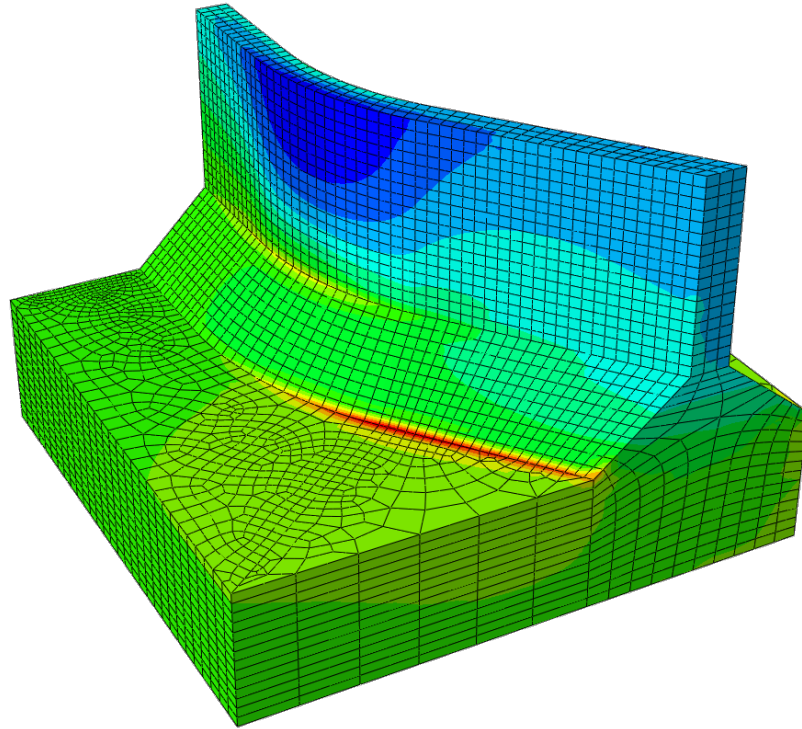




CHALMERS
UNIVERSITY OF TECHNOLOGY



Fatigue Performance of Welded Steel Girders with Corrugated Webs

Master's thesis in the Master's Programme Structural Engineering and Building Technology

ERIK SAVE
KARL ÅKERMO

DEPARTMENT OF ARCHITECTURE AND CIVIL ENGINEERING

CHALMERS UNIVERSITY OF TECHNOLOGY
Gothenburg, Sweden 2020
www.chalmers.se

MASTER'S THESIS ACEX30

Fatigue Performance of Welded Steel Girders with Corrugated Webs

ERIK SAVE
KARL ÅKERMO



CHALMERS
UNIVERSITY OF TECHNOLOGY

Department of Architecture and Civil Engineering
Division of Structural Engineering
Lightweight Structures
CHALMERS UNIVERSITY OF TECHNOLOGY
Gothenburg, Sweden 2020

Fatigue Performance of Welded Steel Girders with Corrugated Webs
ERIK SAVE
KARL ÅKERMO

© ERIK SAVE, KARL ÅKERMO 2020.

Supervisor: PhD. FARSHID ZAMIRI, AFRY ÅF Pöyry AB
Examiner: Prof. MOHAMMAD AL-EMRANI, Department of Architecture and
Civil Engineering

Master's Thesis ACEX30
Department of Architecture and Civil Engineering
Division of Structural Engineering
Chalmers University of Technology
SE-412 96 Gothenburg
Telephone +46 31 772 1000

Cover: Contour plot of maximum principal stress over the expected region of crack initiation.

Typeset in L^AT_EX
Printed by Chalmers Reproservice
Gothenburg, Sweden 2020

Fatigue Performance of Welded Steel Girders with Corrugated Webs

ERIK SAVE

KARL ÅKERMO

Department of Architecture and Civil Engineering

Division of Structural Engineering and Building Physics

Lightweight Structures

Chalmers University of Technology

Abstract

Steel girders with corrugated webs have been widely studied regarding their static capacity. They are known to have high out-of-plane stiffness as well as shear buckling capacity. This permits the use of deeper web plates without the need for additional stiffeners. However, an important aspect that has not been studied to a large extent is the fatigue capacity of these structures. A number of fatigue tests have previously been performed to determine their fatigue resistance. Those tests have shown the complexity of the fatigue performance due to the complex geometry and shear transfer mechanism. One aspect that is argued to influence the stress state is the transverse bending of the flanges due to shear flow in the web. This effect and its influence on the structural hot spot stress at fatigue critical points has not been examined until today and is therefore further investigated in this thesis. This thesis initially presents a state of the art literature review of previous work on fatigue performance of corrugated web girders followed by the procedure, results and discussion of the finite element analyses performed. Evaluation of previously performed experimental tests shows that the fatigue performance of corrugated web girders is slightly better than what is currently suggested in the design standard EN 1993-1-9. Based on the finite element analysis, it is found that the transverse bending of the flanges has an effect on the structural hot spot stress at the fatigue critical points and should be considered in fatigue design. A proposal is presented for considering the structural hot spot stress as a superposition of two parts corresponding to primary and transverse bending of the flanges. Also, suggestions on how to efficiently and accurately model a corrugated web girder using finite element method are given.

Keywords: Corrugated Web, Welded Steel Girder, Fatigue, Finite Element Modelling, Structural Hot Spot Stress, Transverse Bending

Utmattningskapacitet hos Svetsade Stålbalkar med Korrugerade Livplåtar

ERIK SAVE

KARL ÅKERMO

Institutionen för Arkitektur och Samhällsbyggnadsteknik

Konstruktionsteknik och Byggnadsteknologi

Lättviktskonstruktioner

Chalmers Tekniska Högskola

Sammanfattning

Den statiska kapaciteten hos stålbalkar med korrugerade liv har studerats i stor utsträckning i tidigare studier. Den här typen av balk tillhandahåller hög styvhet i tvärriktningen och hög skjuv- och skjuvbucklingskapacitet, vilket i sin tur tillåter djupare livplåtar utan behov av extra avstyvningsplåtar. Utmattningskapaciteten hos dessa typer av balkar har å andra sidan inte studerats i samma utsträckning, vilket ofta är en dimensionerande faktor i svetsade konstruktioner. Ett antal utmattningstester har dock utförts i litteraturen där författarna är eniga om att detta är ett komplext problem som involverar en mängd parametrar. En parameter som påverkar spänningsförhållandet i den dragna flänsen är den transversella böjningen av flänsen som uppstår på grund av skjuvflödet i livet. Effekten av denna spänning på spänningskoncentrationer i den dragna flänsen har hittills inte studerats och detta är därför undersökt i denna rapport. Initialt presenterar denna rapport en "state of the art" litteraturstudie över utmattningskapaciteten hos balkar med korrugerade livplåtar. Följande presenteras metod, resultat och diskussion kring finita element metoden analys som utförts. En analys av tidigare utförda utmattningstester visar att utmattningskapaciteten hos stålbalkar med korrugerade livplåtar är högre än vad som tidigare föreslagits i litteraturen. Utifrån finita element analyser visar denna rapport att den transversella böjningen av flänsen har en effekt på spänningskoncentrationerna vid de kritiska punkterna i den dragna flänsen. En ekvation för hur spänningskoncentrationerna i dessa punkter kan delas upp i två delar kopplade till primär- och transversell böjspänning är föreslagen. Avslutningsvis är ett strukturerat och noggrant sätt att modellera stålbalkar med korrugerade livplåtar med hjälp av finita element presenterat.

Nyckelord: Korrugerade livplåtar, Svetsade stålbalkar, Utmattning, Finita element metoden analys, Spänningskoncentrationer, Transversell böjning

Acknowledgements

This Master's thesis was initiated by Chalmers University of Technology, Department of Architecture and Civil Engineering and conducted at AFRY ÅF Pöyry AB's department of Bridge and Infrastructure in Gothenburg. The project is part of the national research project SUNLIGHT concerning development of maintenance-free steel bridges and has been carried out from January 2020 to June 2020. The computations were performed on resources at Chalmers Centre for Computational Science and Engineering (C3SE) provided by the Swedish National Infrastructure for Computing (SNIC).

This thesis have been carried out with supervisor PhD. Farshid Zamiri at AFRY ÅF Pöyry AB and examiner Prof. Mohammad al-Emrani, Department of Architecture and Civil Engineering.

Farshid, the continuous help from you with wide knowledge spanning over many engineering areas have been invaluable for this project. It has truly been a privilege having you as our supervisor.

Mohammad, you have been an excellent examiner throughout this project. Your ability to rapidly acquaint yourself into complex issues (regardless of day and time) have been very precious.

To both of you, we would like to send our greatest gratitude for your guidance, commitment and enthusiasm from beginning to end of the project.

Gothenburg, June 2020
Erik Save and Karl Åkermo

Contents

List of Figures	XIII
List of Tables	XV
Nomenclature	XVII
1 Introduction	1
1.1 Aim and scope	1
1.2 Objectives	2
1.3 Limitations	2
1.4 Approach	2
2 Literature review	3
2.1 Fatigue in Stainless steel	3
2.2 Geometry of corrugated web girders	4
2.3 Fatigue in corrugated web girders	5
2.4 Analytical studies	7
2.5 Numerical studies	10
2.5.1 K. Anami and R. Sause. (2005)	10
2.5.2 A. Ibrahim, W. W. El-Dakhakhni and M. Elgaaly (2006)	11
2.5.3 B. Kövesdi, B. Jáger and L. Dunai (2012)	12
2.5.4 Z.Y. Wang, Q.Y. Wang and Y.Q. Zhang (2013)	12
2.5.5 S.Y. Wang, Q.Y. Wang and R.J. Jiang (2015)	13
2.5.6 J. Xu, H. Sun, S. Cai, W. Sun and B. Zhang (2019)	14
2.6 Experimental studies	15
2.6.1 Test procedure	15
2.6.2 Previous experiments	16
2.6.2.1 J. D. Harrison (1965)	16
2.6.2.2 M. Korashy and J. Varga (1979)	16
2.6.2.3 R. Rodriguez (2000)	16
2.6.2.4 S.A. Ibrahim (2001)	17
2.6.2.5 H. H. Abbas (2003)	17
2.6.2.6 N. Kotaki, A. Ichikawa, E. Sasaki, C. Miki and T. Hosaka (2003)	18
2.6.2.7 J. Machacek and M. Tuma (2006)	18
2.6.2.8 Z. Y. Wang, Q. Y. Wang and Y. Q. Zhang (2013)	18
2.6.2.9 B. Kövesdi and L. Dunai (2014)	18

2.6.2.10	Z.Y. Wang, Q. Y. Wang and R. J. Jiang (2015)	19
2.6.2.11	J. Xu, H. Sun, S. Chai, W. Sun and B. Zhang (2019)	19
2.6.3	Summary of experimental studies	20
2.6.4	Analysis of experimental studies	24
2.6.4.1	Statistical analysis	26
2.7	Discussion of literature review	32
2.8	Conclusion of literature review	33
3	Methods	35
3.1	Analysis procedure	35
3.2	Structural hot spot stress methods	38
3.2.1	Surface Stress Extrapolation	40
3.2.2	Through Thickness at Weld Toe Integration	41
3.2.3	1mm stress method	42
3.2.4	Hot spot stress in biaxial stress state	43
3.3	Modelling of CWG	44
3.3.1	Global model	45
3.3.2	Intermediate model	47
3.3.3	S-point model	48
3.4	Verification of Model	50
4	Results	53
4.1	Evaluation of SHSS methods	53
4.2	Stress state in bottom flange	56
4.2.1	Comparison between average longitudinal stress and bending stress from beam theory	62
4.2.2	Stress state at S-points	66
5	Discussion	75
5.1	Analytical methods	75
5.2	FE-modelling	76
5.3	Experimental tests	77
6	Conclusions	79
6.1	Concluding remarks	79
6.2	Suggestions for further studies	80
	References	81
A	Python script used to model corrugated web girders	I

List of Figures

2.1	Trapezoidal (a) and sinusoidal (b) corrugation.	4
2.2	S-N curves and fatigue classes for upper and lower bounds of CWGs.	5
2.3	S-point in corrugated web steel girders.	6
2.4	Crack propagation for CWG.	7
2.5	Transverse bending of the flanges due to eccentric shear flow.	9
2.6	Corrugation types for calculation of C-ratios.	10
2.7	Studied detail by (Anami and Sause, 2005).	11
2.8	Corrugated small-scale weld detail.	13
2.9	Fatigue life estimation as a function of t_f and θ	14
2.10	Conceptual three- and four-point bending of beams.	15
2.11	Summary of previous fatigue tests on trapezoidal CWG.	25
2.12	Procedure of Statistical Evaluation.	27
2.13	Summary of previous fatigue tests on trapezoidal CWG, excluding outliers.	29
2.14	Data points grouped by flange thickness category.	30
2.15	Stress gradient effect on thin and thick plates.	30
2.16	Data points grouped by flange thickness category, excluding points from Abbas.	31
2.17	Fatigue classes by flange thickness category.	32
3.1	FE Experiment setup.	37
3.2	Constant moment applied to girders.	37
3.3	Tensile forces applied to the flange detail of one wavelength.	38
3.4	Notch stress at a weld toe (Hobbacher, 2016).	39
3.5	Hot spot types according to IIW standard. (Hobbacher, 2016).	39
3.6	Linear surface stress extrapolation.	41
3.7	Through thickness at weld toe integration.	42
3.8	The 1mm stress at a weld toe.	43
3.9	Hot spot stress at weld toe for biaxial stress state (Hobbacher, 2016).	44
3.10	Simply supported girder, symmetry condition.	45
3.11	Rigid beam constraints at the I-section at the supports.	46
3.12	Global model's mesh.	46
3.13	Overlay plot, shell-to-solid modeling. Global model composed of shell elements drives the intermediate model made up of solid elements.	47
3.14	Intermediate model's mesh.	48
3.15	Overlay plot, solid-to-solid submodeling.	49

3.16	S-point model's mesh.	49
3.17	Strain gauge and convergence path locations for convergence study of FE mesh.	50
4.1	Maximum principal stress contour at S-point in constant moment zone, girder from the experiments by Ibrahim (2001).	53
4.2	Stress contour through web thickness, girder from experiments of Ibrahim (2001).	54
4.3	Maximum principal stress contour at S-point when web is neglected, girder from the experiments by Ibrahim (2001).	55
4.4	Comparison between structural hot spot stress methods.	56
4.5	Definition of "North" and "south" edges along the bottom flange.	57
4.6	Transverse deflection of bottom flanges for all test girders.	57
4.7	Longitudinal stresses (S11) along north and south edge of bottom flange for girders 1 and 2.	58
4.8	Longitudinal stresses (S11) along north and south edge of bottom flange for girders 3 and 4.	59
4.9	Average and delta stresses for girders 1 and 2.	60
4.10	Average and delta stresses for girders 3 and 4.	61
4.11	Longitudinal stress sections girders 2 and 3.	62
4.12	Superposition of primary and transverse bending stresses.	63
4.13	Longitudinal stress profiles across the flange width in various sections for girder 2.	63
4.14	Longitudinal stress profiles across the flange width in various sections for girder 3.	64
4.15	Studied S-points along the girders.	66
4.16	Variation of longitudinal stress from primary bending at S-points along the girders.	67
4.17	Variation of transverse bending stresses at S-points along the girders.	68
4.18	Variation of structural hot spot stress at S-points along the girders.	68
4.19	SHSS normalized by primary bending stress at S-points.	69
4.20	Relation between transverse bending stress normalized by primary bending stress and SHSS normalized by primary bending stress at S-points.	70
4.21	Variation of SCF_t at S-points.	72
4.22	Comparison between SHSS obtained from FE-analyses and SHSS calculated with the proposed equation.	73
5.1	Transverse deflection modes for girders from experimental tests mentioned in 2.	77

List of Tables

2.1	C-factors by Abbas et al. (2007).	9
2.2	Difference of FE-models to experimental tests.	12
2.3	Geometrical and testing parameters of all previous studies.	21
2.4	Geometrical parameters of trapezoidally corrugated girders.	23
2.5	Factors tested for statistical significance.	28
3.1	Common geometry parameters for test girders.	36
3.2	Variable parameters for test girders.	36
3.3	Mesh convergence for global model.	51
3.4	Comparison between FE models and experimental data from Ibrahim (2001).	52
4.1	Comparison between primary bending stress from beam theory and approximated primary bending stress.	65
4.2	Stress concentration factor for primary bending stress from pure bending and uniform tension models.	71
4.3	SCF_p and SCF_t for the 4 studied girders.	72

Nomenclature

Abbreviations

C3SE	Chalmers Centre for Computational Science and Engineering
CAFL	Constant amplitude fatigue limit
CT	Corrugation type
CWG	Corrugated web girders
DI	Discrete corrugations
FE	Finite element
IIW	International Institute of Welding
LVDT	Linear variable differential transformer
MPC	Multi-point constraint
OFAT	One-factor-at-a-time method
SCF	Stress concentration factor
SHSS	Structural hot spot stress
SI	Sinusoidal corrugations
SNIC	Swedish National Infrastructure for Computing
SSE	Surface stress extrapolation
TR	Trapezoidal corrugations
TTWT	Through thickness at weld toe integration
UIT	Ultrasonic Impact Treatment, weld treatment method

Glossary

1mm stress method	Structural hot spot stress evaluation method
ABAQUS	Commercial finite element software
ANSYS	Commercial finite element software
Eurocode	Collection of standards specifying how structural design should be conducted within the European Union
FAT	Fatigue design strength of a welded detail acc. to Eurocode and International Institute of Welding

fe-safe	Commercial finite element software
Nominal stress method	Commonly used fatigue strength evaluation method found in Eurocode and International Institute of Welding
Null-hypothesis	Initial hypothesis when conducting a statistical evaluation
Run-out	Fatigue test that does not reach failure criterion during testing
S-N curve	Curve used for fatigue strength evaluation of structural details
S-point	Critical point of fatigue initiation in corrugated web girders

Greek letters

$\Delta\sigma_{nom}$	Nominal stress range used when evaluating fatigue life according to nominal stress method
σ_b	Bending stress
σ_m	Membrane stress
σ_p	Primary bending stress
σ_t	Transverse bending stress subjected to the flange
σ_{nl}	Non-linear peak stress
σ_{nom}	Nominal primary bending stress
σ_{SHSS}	Structural hot spot stress
θ	Corrugation angle

Roman lower case letters

a_w	Weld throat thickness
$b_{f,bot}$	width of bottom flange
$b_{f,top}$	Width of top flange
h_w	Web height
l_{eff}	Effective length of the girder
$l_{inc,hor}$	Projected length of inclined fold
l_{inc}	Length of inclined fold
l_{par}	Length of parallel fold
l_wl	Corrugation wavelength
t_f	Flange thickness
t_w	Web thickness

$t_{f,bot}$ Thickness of bottom flange

$t_{f,top}$ Thickness of top flange

Roman upper case letter

H_c Corrugation depth

R Bend radius between an inclined fold and a parallel fold

$R_{circular}$ Bend radius of a sinusoidal corrugation

SCF_p Stress concentration factor for primary bending stresses

SCF_t Stress concentration factor for transverse bending stresses

S11 Longitudinal stress

1

Introduction

The Swedish road administration along with several private actors are currently trying to promote the use of stainless steel in bridge design. The main reason for this promotion is the superior resistance to environmental corrosion in stainless steel compared to carbon steel, leading to substantial cost reductions in inspections, repainting and replacements during the service life of the bridges. However, stainless steel has a higher initial cost (Karlsson, 2018) than carbon steel which gives an incentive to find highly material-efficient structures.

Girders with corrugated web plates are a desirable solution to this aim. This type of girder has been used in bridge design in many countries in Europe and Asia due to its superior out of plane stiffness and shear capacity compared to conventional stiffened plate girders. This design permits an increase in web height without the need for adding stiffeners to the web which increases the structural capacity-to-weight ratio, leading to more effective material utilization. Up to date, there is a large amount of test data and studies on the static capacity and behaviour available on corrugated web girders. However, the fatigue performance of these structures has been studied to a smaller extent which is troublesome since the fatigue capacity of steel bridge girders is often the limiting design aspect. It is therefore of high interest to investigate the fatigue performance of these types of girders. The initial intent of this thesis was to investigate the fatigue performance of corrugated web girders made in stainless steel. However, as will be evident in Section 2.1, the fatigue performance of welded stainless steel structures is regarded as equal to the fatigue performance of carbon steel in the design codes (Hobbacher, 2016; EN:1993, 2005). Furthermore, there are no fatigue tests or information available in the literature on the use of stainless steel in corrugate web girders. Therefore, this thesis will focus on corrugated web girders made in carbon steel.

1.1 Aim and scope

The complex geometry and stress state in corrugated web girders compared to conventional stiffened plate girders creates uncertainty in fatigue assessment of these types of structures. The aim of this thesis is therefore to examine the fatigue behaviour and resistance of these corrugated web girders and to investigate if there is a unified way of determining the fatigue performance. As this major aim gives rise to several questions, the main issue has been divided into the following questions:

- Which corrugation geometry parameters affect the fatigue performance and what rate?
- How does the force- and stress field in the flanges affect the location of the critical crack along the girder?
- How can the global response and the complex stress state be modelled efficiently?

1.2 Objectives

The objective of this thesis is to provide insight for bridge designers in regards to fatigue performance of corrugated web girders. This knowledge can further be used to optimize the design of these structures.

1.3 Limitations

In this thesis, the fatigue performance of corrugated steel girders is sought. It is known from experimental studies that the fatigue critical point for bending cases is located in the flange connected to the weld toe, therefore this thesis will be restricted to considering this issue.

As mentioned, fatigue tests have solely been performed on corrugated web girders with carbon steel but the fatigue resistance for stainless steel and carbon steel is considered equal in the design recommendations from the International Institute of Welding. Therefore the fatigue resistance of these girders made of carbon steel is investigated.

Finally, only trapezoidal corrugated web girders will be analysed in this thesis. However, it is yet important to understand the fatigue performance of all types of corrugations and loading conditions. Therefore, the literature review is presenting all previous work performed on corrugated girders in regard to fatigue.

1.4 Approach

The thesis has been divided into three parts. Firstly, in chapter 2, a state of the art literature review where what is known today about fatigue in corrugated web girders is conducted. The literature review includes analytical, numerical and experimental findings along with comments and statistical evaluation from previous work. Additionally, a collective fatigue resistance class for the tested specimens is suggested. Secondly, in Chapters 3 and 4, the analysis part including procedure and results of finite element modeling is presented. Thirdly, in Chapters 5 and 6, discussion, conclusions and suggestions for further studies are presented for the analysis part. The connection to previous studies is also discussed in these chapters. In the appendix, the script used for the analysis part is given.

2

Literature review

In the last decades, many researchers have carried out fatigue tests and analyses on corrugated web girders to establish the fatigue performance of plate girders with corrugated webs. Experimental, numerical and analytical studies with varying beam geometries, loading conditions and weld methods have been performed. In the following chapter, an investigation of these studies is conducted to establish what can be concluded on the fatigue performance of corrugated web girders (CWG) and what parameters or behaviours that possibly need further research.

2.1 Fatigue in Stainless steel

In order to determine the fatigue performance of welded stainless steel details compared to carbon steel details several fatigue tests have been performed in the past. According to Baddoo (2017) numerous authors have tested various types of welded details. Earlier test show that the fatigue performance for austenitic and duplex stainless steel show similar or slightly higher fatigue performance than carbon steel, while more recent studies show slightly lower fatigue performance for stainless steels, throwing some doubt on the earlier anticipated superior performance. However, the design recommendations presented in Eurocode (EN:1993, 2005) and International Institute of Welding (IIW) (Hobbacher, 2016) suggest using the same S-N curves for stainless steel as for carbon steel. furthermore, there are not yet any design curves for stainless steel available in the codes. In the case of corrugated web girder details made in stainless steel, there are no tests or information to be found in the literature.

Since there are no tests or information to be found on the use of stainless steel in corrugated web girders, the investigation of fatigue performance of CWGs are performed on girders with regular carbon steel. It can then be argued that since stainless steel is treated as carbon steel in regard to fatigue in the codes, the findings in this thesis are also applicable to corrugated web girders in austenitic and duplex stainless steel.

2.2 Geometry of corrugated web girders

Some parameters that are affecting the structural response of the beam are shared with plate girders with flat web profiles namely:

- l_{eff} , effective length of the girder.
- h_w , web height.
- t_w , web thickness.
- a_w , weld throat thickness.
- $t_{f,top}$, $b_{f,top}$, thickness and width for top flange.
- $t_{f,bot}$, $b_{f,bot}$, thickness and width for bottom flange.

For the corrugated web profiles, additional geometrical parameters appear to describe the design. Two main corrugation types (CT) can be recognized in the literature, namely sinusoidal (SI) and trapezoidal corrugations (TR), see Figure 2.1. A sinusoidal shaped corrugation has smooth transitions and can be described by the corrugation depth H_C , bend radius R and length of a full wavelength l_{wl} . For the trapezoidal corrugated web, additional parameters are required to describe the geometry namely:

- θ , corrugation angle
- l_{par} , parallel fold length
- l_{inc} , inclined fold length, or:
- $l_{inc,hor}$, the projected length of the inclined fold along the longitudinal axis.

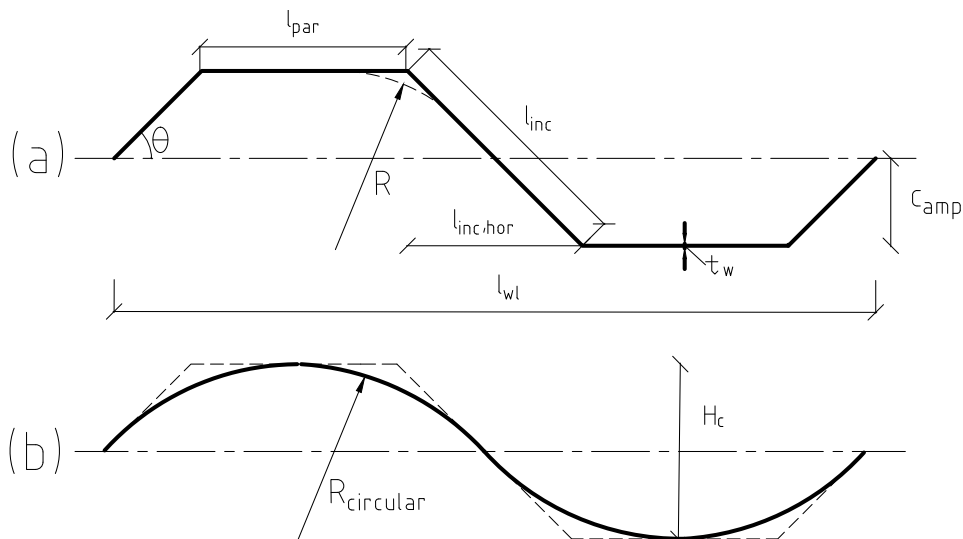


Figure 2.1: Trapezoidal (a) and sinusoidal (b) corrugation.

2.3 Fatigue in corrugated web girders

The literature presents both agreement and disagreement on parameters that influence the fatigue performance of corrugated web girders. To be able to design a fatigue-resistant CWG, knowledge about the following aspects are required:

- Where the fatigue critical points occur.
- Which geometrical parameters affect the severity of the stress concentrations.
- What loading conditions are governing.

It is concluded in previous studies that the fatigue class of corrugated webs fit somewhere between Category B, B' and C in AASHTO Specifications (AASHTO, 2013; Sause et al., 2003) which correlates to fatigue design categories (FAT) of 125 or 112 and 80 in Eurocode 3 (EN:1993, 2005). The upper and lower bounds correspond to constructional details of a plate with longitudinal weld and a welded transverse attachment, see Figure 2.2.

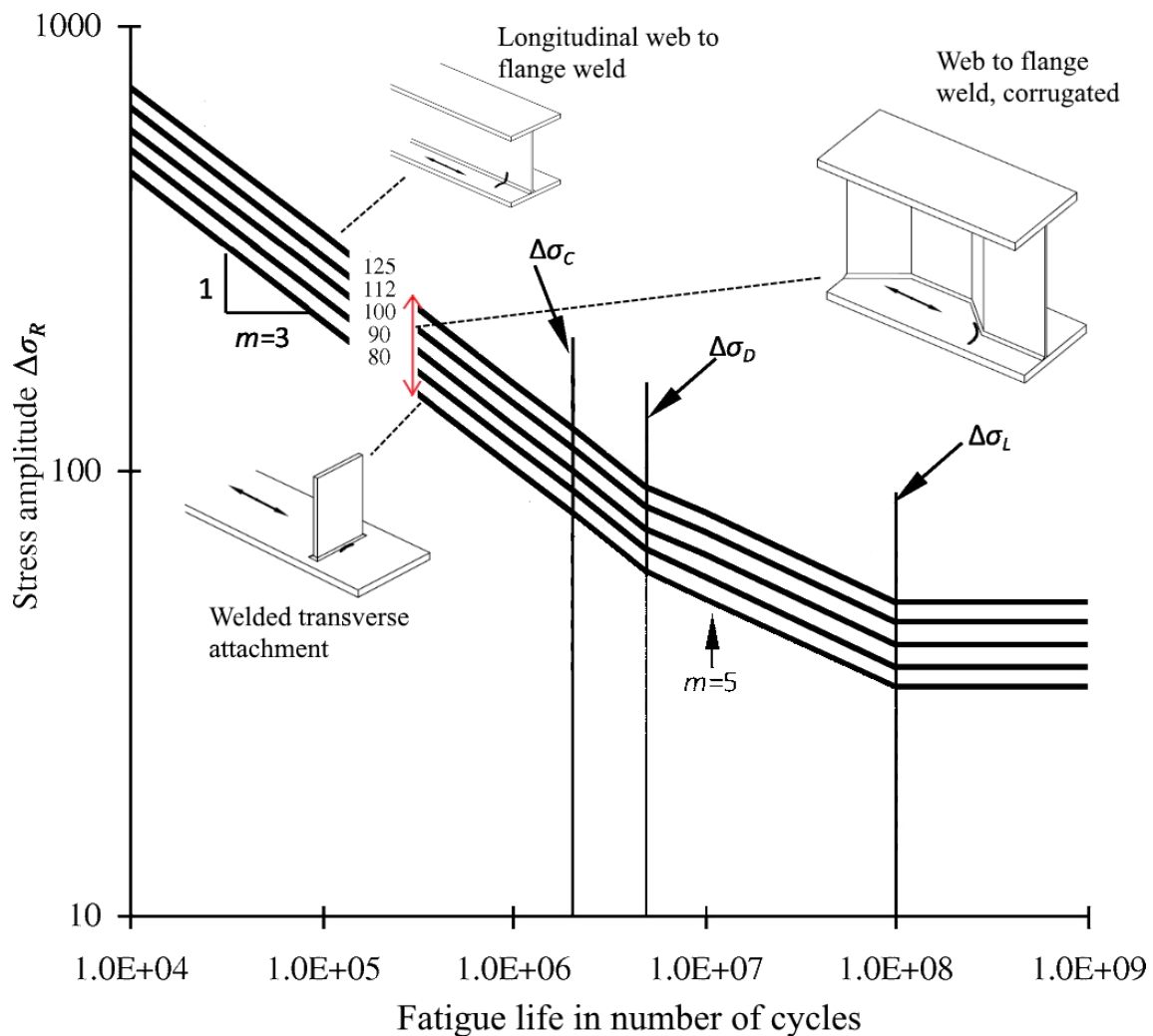


Figure 2.2: S-N curves and fatigue classes for upper and lower bounds of CWGs.

There is a common understanding in the literature that the most critical point with regard to fatigue in corrugated web steel girders with trapezoidal corrugations is the "S-point" presented in Figure 2.3. The S-point is located at the beginning of the bend region in the intersection between a longitudinal fold and an inclined fold. It is also stated from previous authors (Ibrahim, 2001; Abbas, 2003) that the two main parameters affecting the severity of the stress concentration at this point are the corrugation angle θ and the radius of the bend region R , both presented in Figure 2.3. Generally, smaller corrugation angles and larger bend radius result in lower stress concentrations.

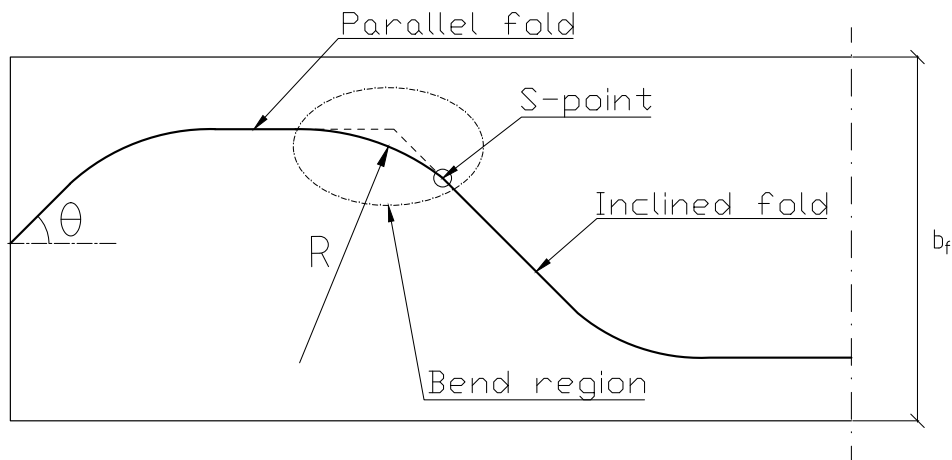


Figure 2.3: S-point in corrugated web steel girders.

Figure 2.4 presents the most common fatigue failure in a CWG. At S-point, the crack initiates at the weld toe and propagates a few millimeters along the weld toe. The crack then changes direction and propagates further through the tensile flange, perpendicular to the principal stress until failure.

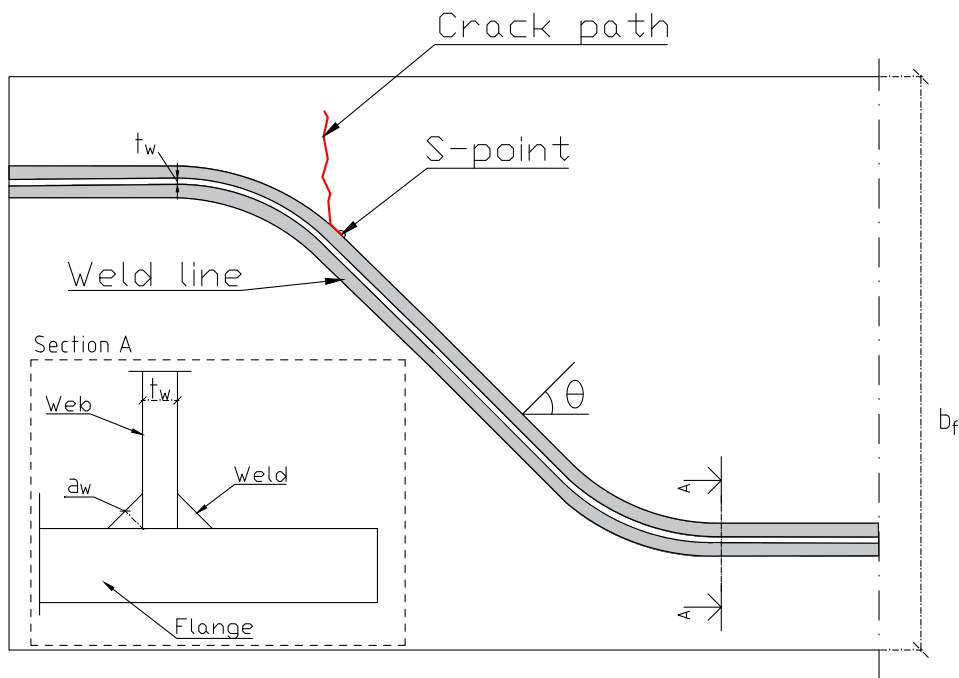


Figure 2.4: Crack propagation for CWG.

2.4 Analytical studies

Corrugated web girders are complex structures that often require numerical analysis to explain the structural response accurately. However, a few authors have demonstrated explanations of how different loading situations and geometries influence the capacity of the beam. The two corrugation profiles, trapezoidal and sinusoidal waved girders perform differently depending on the loading type. Trapezoidal corrugations perform superior to sinusoidal corrugations under static loading. This can be originated from the "accordion effect" which is more pronounced in sinusoidal corrugations. The accordion effect signifies that the corrugated web barely contributes to the bending capacity of the beam, thus when calculating the second moment of inertia analytically, only the contribution from the flanges is considered. Subsequently, only the contribution from the web is considered when calculating the shear and shear buckling capacity. Since sinusoidal corrugations have no parts of the web that are parallel to the longitudinal axis of the girder, the contribution to flexure from the web is less than that of trapezoidal corrugations, which have sections of the web that are parallel to the longitudinal axis and thus contributing more to the bending capacity (Kövesdi et al., 2012). On the other hand, sinusoidal corrugations perform better under fatigue loading conditions since the geometrical stress concentrations are smaller compared to trapezoidal corrugations. It is suggested from previous studies that the static load-bearing capacity decreases with approximately 10% between sinusoidal and trapezoidal corrugations (Ibrahim, 2001).

The literature seems to agree that the most severe loading conditions with regard to fatigue damage on corrugated web girders are those that give rise to combined shear and bending action. This is due to that the shear flow in the eccentric web-to-flange connection gives rise to an additional transverse in-plane bending moment in the flanges. This secondary bending effect results in longitudinal stresses in the flanges in addition to those induced by primary bending. The magnitude of these stresses depends on the following factors(Kövesdi et al., 2012; Abbas, 2003):

- The geometry and the number of corrugations.
- If the load is applied on a longitudinal or inclined fold.
- The support conditions.

An illustration of the flange transverse bending can be seen in Figure 2.5. An in-depth study of this phenomenon along with methods to calculate these secondary bending effects are given by Abbas et al. (2006) and Abbas et al. (2007), respectively. One of these methods is called the "fictitious load method", where a transverse load that gives rise to transverse bending and lateral shear in the flanges is considered. Abbas analytical study resulted in a general formula (eq.2.1), describing the additional bending moment for a sinusoidal shaped girder at a certain position along the beam:

$$M_t^{sin} = \frac{p_y \cdot L_0^2 \cdot H_C}{2 \cdot h_w} \cdot \left\{ \frac{1}{\Pi^2} \cdot \left[\left(1 - 2 \cdot \frac{z}{L_0}\right) \cdot \Pi \cdot c_\zeta + 2 \cdot s_\zeta + \left(\Pi \cdot c_\Pi - 2 \cdot s_\Pi + \Pi\right) \cdot \frac{z}{L_0} - \Pi \right] \right\} \quad (2.1)$$

where:

Π	$2 \cdot \pi \cdot n$	p_y	Uniformly distributed in-plane load
c_ζ	$\cos(2 \cdot \pi \cdot n \cdot \frac{z}{L_0})$	L_0	Girder span
c_Π	$\cos(2 \cdot \pi \cdot n)$	n	Number of corrugation waves
s_ζ	$\sin(2 \cdot \pi \cdot n)$	z	Position of the analyzed cross-section along
s_Π	$\sin(2 \cdot \pi \cdot n)$		the girder

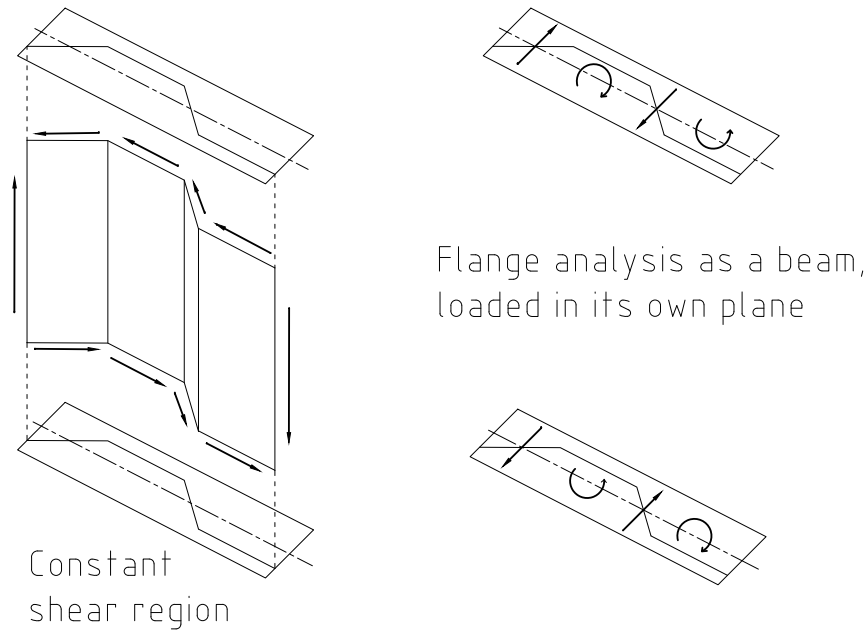


Figure 2.5: Transverse bending of the flanges due to eccentric shear flow.

Since the first analytical formula from Abbas (2003) applied exclusively to sinusoidal shaped girders, correction factors for calculating the transverse bending moment for trapezoidal corrugations were later developed by the same researchers Abbas et al. (2007). It was shown that the correction factors could be originated to the difference in area under one half wavelength between the corrugation types. The authors also showed that the additional transverse bending moment could be calculated for any corrugation type and geometry by first calculating the transverse bending moment for a sinusoidal corrugation with the same corrugation depth and wavelength and then multiplying with the corresponding C-factor. The C-factor for different types of corrugations are presented in Table 2.1 and the transformation equation is presented as Equation 2.2 below:

$$M_t = C_i \cdot M_t^{sin} \quad (2.2)$$

The corresponding C-factors for different corrugations are presented in Table 2.1.

Table 2.1: C-factors by Abbas et al. (2007).

Corrugation	Area of half wave length $[\int_0^{L_{wl}/2} edz]$	C-ratio
Sinusoidal	$\frac{H_c \cdot L_{wl}}{2 \cdot \pi}$	1
Trapezoidal	$\frac{H_c}{2} [l_{par} + l_{inc,hor}/2]$	$\pi \left[\frac{b + l_{inc,hor}/2}{l_{wl}} \right]$
Triangular	$\frac{H_c \cdot l_{wl}}{8}$	$\pi/4$
Rectangular	$\frac{H_c \cdot L_{wl}}{4}$	$\pi/2$

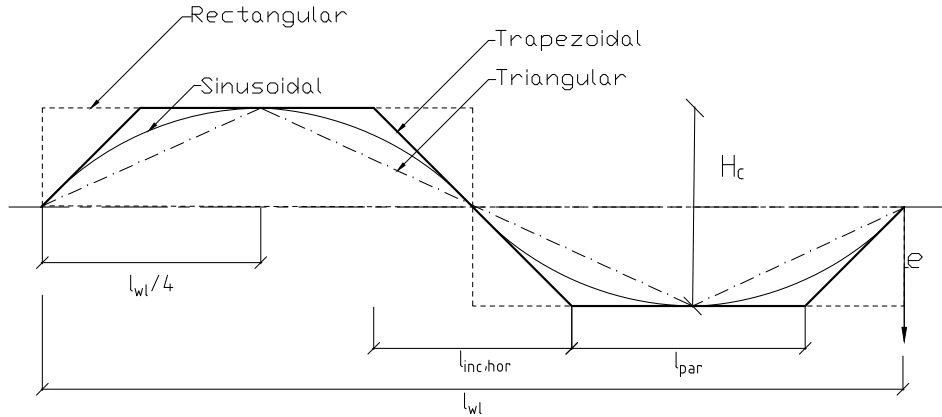


Figure 2.6: Corrugation types for calculation of C -ratios.

Furthermore, similar in-plane bending also occurs in constant bending zones where no shear is present (Kövesdi et al., 2012). This is once again originated from the accordion effect. Since the parallel sections of the web contribute more to the second moment of inertia than the inclined sections of the web, the flanges in the parallel sections will experience lower normal stress than the flanges in the inclined sections. The non-uniform stress distribution will then give rise to a transverse in-plane bending of the flanges. This behaviour has however not yet been explained analytically and therefore, numerical analyses are recommended when examining this phenomenon. This transverse bending contribution is commonly referred to as the secondary transverse bending but is normally neglected due to its marginal magnitude.

2.5 Numerical studies

Numerical analyses have been performed alongside analytical and experimental tests to further investigate how the various parameters influence the structural behaviour of the corrugated girders. The numerical analyses are initially modelled as a digital twin, i.e. with the same geometry and material parameters as the associating experimental test girders. After the model has been compared to conform with the structural behaviour of the experimental test, a chosen individual parameter of interest is subsequently adjusted to study its influence, commonly described as one-factor-at-a-time analysis (OFAT). The finite element software used include ABAQUS, ANSYS and fe-safe. Following sections briefly describe the numerical analyses from previous authors and their main findings.

2.5.1 K. Anami and R. Sause. (2005)

In 2005, Anami et. al modelled a flange detail with a single trapezoidal corrugation wavelength attachment and applied uniform nominal stress to the flange part, see Figure 2.7. This model provided the opportunity to study the behaviour of these kinds of details without the influence of secondary nominal stresses induced in the

flange by shear flow in the web, as discussed in Section 2.4. The corrugation angle θ and the bend radius R were adjusted in the model to investigate their effects on the level of stress concentration at the S-point. The hypothesis of the study was that this type of detail should fall between the fatigue strength category of a T-form joint and a longitudinal gusset plate joint. A noteworthy finding in this study is that by increasing the transverse distance, H_1 between point S and the parallel fold, by increasing the bend radius, the influence of the parallel fold can be eliminated and thus the detail could be regarded as a T-form joint with an inclined attachment (Anami and Sause, 2005). However, it is important to note that the authors intentionally excluded the complex stress conditions usually found in this kind of detail by applying normal stress directly to the flange. This provides the opportunity to study the single corrugation detail itself, but it also renders the application of the results to a girder with more complex stress conditions questionable, for which the authors give background to for further research.

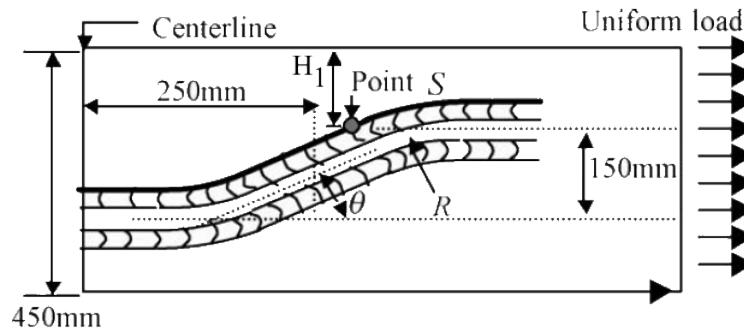


Figure 2.7: Studied detail by (Anami and Sause, 2005).

2.5.2 A. Ibrahim, W. W. El-Dakhakhni and M. Elgaaly (2006)

A full girder model, a three waved and a single waved corrugated model were set up in this study. The aim was to study whether a full corrugated girder model is needed for structural analysis or if a more simple model is sufficient to explain a similar response. The stress distributions from the models were compared to previous test results described in Section 2.6.2.4. The results showed that the stresses differed between 0.7 - 8.5%, 0.5 - 8.7%, and 3 - 10.8% for the full-girder, three-corrugation and the single-corrugation model compared to the tested girder, respectively, see Table 2.2. The authors concluded that a single-corrugation finite element model can be used with sufficient accuracy (Ibrahim et al., 2006).

Furthermore, OFAT analyses were executed studying how the stress concentration was influenced by the bend radius R . As described in Section 2.2, sinusoidal corrugation performs better in regard to fatigue than trapezoidal corrugation. Therefore, a case of maximum radius, $R_{circular}$, of which the inclined fold and parallel fold would tangent in their mid-lengths, was initially calculated for the trapezoidal corrugation. This maximum radius was then compared to an increasing actual bend radius for

Table 2.2: Difference of FE-models to experimental tests.

Model	Minimum stress difference	Maximum stress difference
Full girder model	0.7%	8.5%
Three wavelength model	0.5%	8.7%
Single wavelength model	3%	10.8%

the trapezoidal corrugation. By subsequently increasing the bend radius, the stress concentration factor (SCF) was gradually reduced at the S-point. The authors concluded that the fatigue life of the trapezoidal corrugated detail could increase to that of a sinusoidal corrugated detail if the bend radius was larger and equal to one fourth of the bend radius in case of sinusoidal corrugation.

2.5.3 B. Kövesdi, B. Jáger and L. Dunai (2012)

In this study, numerical analyses were conducted to examine the behavior of corrugated girders under different loading conditions. Before adjusting the loading situation, the FE model was first verified by modeling the girder with the same conditions as the experimental specimens. After the structural response of the FE model conformed with the experimental results, the loading conditions were changed. The study examined the influence of applying a three-point bending load on an inclined or a parallel fold. Furthermore, various cases were examined based on the number of half-corrugation waves between the support and the loading point. The results showed that the most unfavorable loading situation regarding the additional transverse bending moment was when supports and loading were located in the middle of an inclined fold with a whole number of corrugation lengths between the supports and loading point. From these findings, Kövesdi et al. (2012) concluded that the previous analytical formula, explained in Section 2.4 does not capture the additional stresses for this most unfavorable scenario. The authors then suggested an enhanced and simplified expression for describing the average and maximum local transverse bending for trapezoidal corrugations:

$$M_{t,avg} = \frac{V \cdot H_c}{4 \cdot h_w} \cdot (2 \cdot l_{par} + l_{inc,hor}) \quad (2.3)$$

$$M_{t,max} = \frac{V \cdot H_c}{2 \cdot h_w} \cdot (2 \cdot l_{par} + l_{inc,hor}) \quad (2.4)$$

where V is the shear force in the section.

2.5.4 Z.Y. Wang, Q.Y. Wang and Y.Q. Zhang (2013)

In 2013, Wang et al. (2013a) conducted both experimental and numerical analyses to study small-size welded details. The details consisted of half a corrugation wavelength with web welded to a flange, see Figure 2.8. The fatigue behaviour was examined for details with corrugation angles of 30° and 45° during cyclic tensile loading subjected to the flange. The results showed that both for the experimental

and numerical analysis, the details with 45° corrugation angles achieved a higher stress concentration factor, thus shorter fatigue lives of roughly 50%. Furthermore, the location of the S-point approached closer to the parallel fold as the angle was increased. The authors also concluded that effective notch stress analysis is useful when determining critical stress concentrations as they conform well with the experimental data.

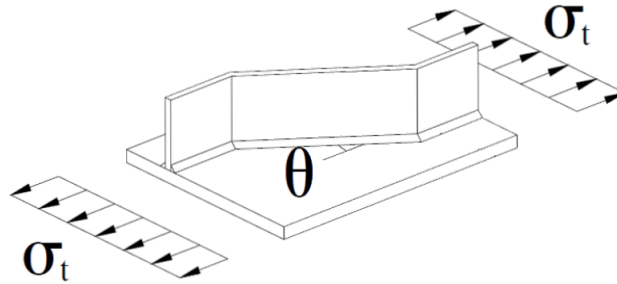


Figure 2.8: Corrugated small-scale weld detail.

2.5.5 S.Y. Wang, Q.Y. Wang and R.J. Jiang (2015)

Wang et al. (2015) examined the interaction of flange thickness t_f and corrugation angle θ using effective notch stress approach. The flange thickness was increased from 5 mm to 10 mm for a girder with a constant 45° corrugation angle. The doubling of the flange thickness showed an increase in fatigue life of 133% due to the reduced stresses in the flange when subjecting the model to the same load. However, the increase in flange thickness will substantially increase the structural weight of the girder, approximately by 50%. The same procedure was subsequently performed for a girder with a corrugation angle of 30° . It could be seen that a reduction in corrugation angle corresponds to a fatigue life increase of 35% which corresponds approximately to an increase of flange thickness of 2 mm. The authors recommendation from a material's weight point of view was to reduce the corrugation angle rather than increase flange thickness for better fatigue resistance. Results by Wang et al. (2015) are presented in Figure 2.9.

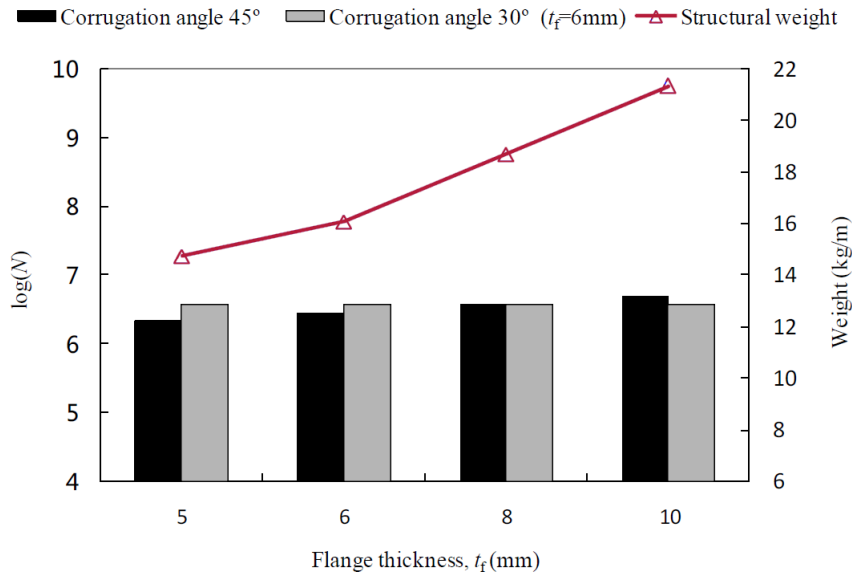


Figure 2.9: Fatigue life estimation as a function of t_f and θ .

2.5.6 J. Xu, H. Sun, S. Cai, W. Sun and B. Zhang (2019)

Several OFAT parametric analyses were made in this study. The parameters that the authors examined were:

- θ , corrugation angle.
- R, bend radius.
- a_w , weld throat thickness.
- α , inclination angle between flange and horizontal axis.

The influences of these parameters were compared by the varying stress concentration, described by the maximum principal stress measured at a distance of 2 mm from the weld toe at the critical S-point. Initially, the corrugation angle was examined. By increasing the angle from 30° to 60° , the authors concluded that the stress concentration was increased by approximately 30%. The bend radius was in the same way examined by a varying range between 50 and 200 mm. The results showed that the concentration factor was reduced by 30.9% for the total range but approximately half of the reduction was located between $R=50\text{mm}$ and $R=100\text{mm}$. This suggests that a minimum value of R equals 100 mm for this girder would be suitable Xu et al. (2019). The authors also confirmed this suggestion with design code recommendations from The Chinese National Standard which states a recommendation for R equal to a minimum of 97 mm or 15 times the web thickness. The inclined angle of the oblique flange, α was supposed to represent a box girder case. This angle was modelled between 10° and 30° in relation to the horizontal axis. The results showed that the stress concentration is lowered marginally with 1.7% with a decrease from 30° to 10° . Finally, the weld size was examined within a range of 6 to 10 mm. The largest 10 mm weld raised the stress concentration by 3.8% compared to a size of 6 mm. This parametric study mostly follows the conclusions from previous authors except for the study of the weld size. Previous authors e.g Kövesdi and

Dunai (2014), have concluded by experimental tests that the weld size is a major factor affecting the fatigue life. This difference could be explained by challenges in numerical modeling of representational welds.

2.6 Experimental studies

Numerous laboratory tests have been executed to acquire an understanding of how a corrugated web girder made of carbon steel is affected by different kinds of loading and their interactions. However, not as many fatigue tests have been performed due to two main reasons. First, experiments within this topic are normally expensive due to that large scale specimens are required to achieve a realistic behaviour of the girders and secondly, due to the time-consuming nature of high cycle fatigue testing. Therefore, every experiment that has been previously executed is valuable to include to understand fatigue resistance of these type of girders. Since the girders vary in many aspects e.g. geometry, type of loading and welding procedure, it is important to carefully review every test to understand which tests are relevant and comparable to each other. This section covers how the tests have generally been performed and which conclusions that can be drawn from them.

2.6.1 Test procedure

The tests have been performed similarly by three-point or four-point bending, see Figure 2.10. Strain gauges are generally placed along the beam, especially throughout the flanges. Prior to fatigue testing, the specimens are loaded statically to obtain the static response of the girder. The specimens are subsequently subjected to cyclic loading at different stress ranges until either failure occurs or that the testing time has ended, defined as "run-out". During the test, the girders are visually examined for cracks and the strains are measured by the strain gauges. The deflection in mid-span is often measured using linear variable differential transformers (LVDTs).

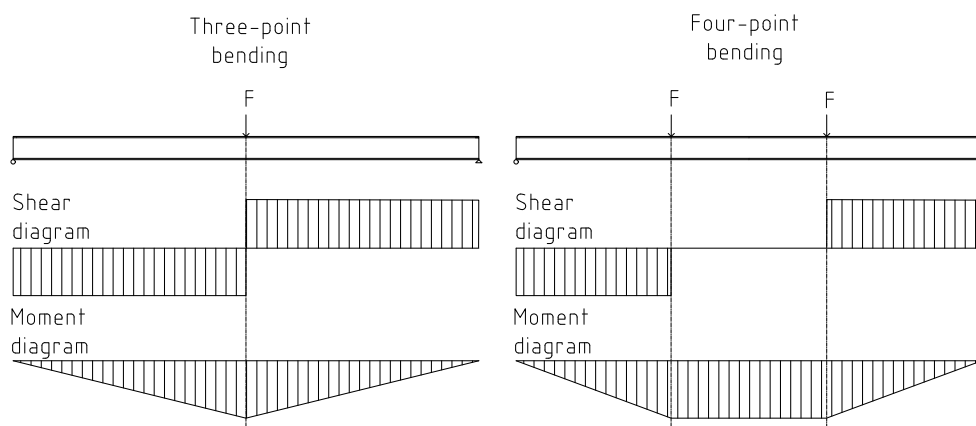


Figure 2.10: Conceptual three- and four-point bending of beams.

2.6.2 Previous experiments

Different techniques and focus for e.g loading and welding have been effectuated by previous authors. It is therefore essential to examine how the tests have been performed to be able to determine comparable results. The main differences in geometry and load situation of the various tests are presented in Table 2.3. The stresses ($\Delta\sigma_{nom}$) are defined as the maximum nominal stress ranges at the top of the bottom flange at fracture location. This section will follow the same structure as previous Section 2.5 by briefly describing the experimental studies from the literature along with their findings.

2.6.2.1 J. D. Harrison (1965)

The first fatigue experiments for corrugated web girders were performed by Harrison (1965). Two sinusoidal girders were tested in four-point bending at measured average stress ranges in the flange of 185 MPa and 156 MPa. The two girders failed at 1.1 and 2.35 million cycles, respectively. The first girder failed prematurely from a notch in the flame cut edge of the tension flange. For the second girder, Harrison (1965) reported several cracks initiating from the web-to-flange fillet weld. Both girders failed outside the pure bending zone where combined shear and moment occurs, explained in Section 2.4.

2.6.2.2 M. Korashy and J. Varga (1979)

Korashy and Varga (1979) tested 18 stiffened steel girders with different geometries in four-point bending. Eleven girders were stiffened by discrete (DI) sinusoidal corrugation while the other seven were conventional I-girders with vertical stiffeners. The calculated nominal stresses for the partial corrugated specimens varied between 132-216 MPa with associating fatigue lives between 1 and 2.7 million cycles. The study focused on how corrugation affected the fatigue life compared to conventionally stiffened girders. The results from Korashy and Varga (1979) reported that the sinusoidal shaped girders showed approximately 25% increased fatigue life compared to the conventional I-girders due to the reduced stress concentration, described in Section 2.3.

2.6.2.3 R. Rodriguez (2000)

Rodriguez (2000) investigated how bearing stiffeners affect the fatigue life of CWGs. The experiments were performed by testing six girders with varying stiffener types under cyclic loading. Rodriguez (2000) concluded that the vertical stiffeners should not be attached to the tension flange and cut short to avoid the stress region in the flange and lower web. Furthermore, the best location of the vertical stiffener was determined to be in the center of the inclined fold. This is due to the reduction of the eccentricity of the applied load with respect to the web. Even though these are valuable results, only the sixth specimen from this study is comparable to the other studies since they share the same stiffener situation. It should be noted

that the failure modes for Rodriguez (2000) specimens differ from the rest of the experimental tests mentioned in this report, some of them even develop cracks in the compressed flange. The only specimen that shows the same failure mode as the rest of the experimental test and which also share the same stiffener situation is, as mentioned, specimen number six. This should be kept in mind if data points gathered from (Rodriguez, 2000) would deviate from trends seen for test data gathered for the other experiments mentioned in this section.

2.6.2.4 S.A. Ibrahim (2001)

The first experiments of plate girders with trapezoidal corrugation was completed by Ibrahim (2001). The six specimens with the same geometry were subjected to four-point bending with different stress ranges. The nominal stress ranges spanned from 64.7 MPa to 161.8 MPa which resulted in fatigue lives between 17.61 and 1.24 million cycles, respectively. All the girders failed within the constant moment zone unlike the previous experiments but still at the critical S-point, described in Section 2.2. The first of the six girders failed prematurely due to a start-stop of the weld at the inclined fold line between the longitudinal and inclined folds where high stresses arise. As the first specimen did not result in the expected fatigue life, the sixth specimen was performed as a repetition of the first girder but with the weld start-stop adjusted to be located at the middle of the inclined fold instead. This change resulted in a fatigue life increase from 2.61 to 9.34 million cycles.

2.6.2.5 H. H. Abbas (2003)

Prior the experimental testing, Abbas (2003) determined the theoretical critical fatigue points by analytical methods, which is special for this study. Abbas (2003) concluded that the stresses in the tensile flange in the shear region were higher than the stresses within the constant moment zone due to flange transverse bending, described in Section 2.4. The points where the maximum stresses were expected to be located were therefore post-weld treated using ultrasonic impact treatment (UIT) to improve their fatigue strength. Abbas (2003) then completed fatigue testing of eight girders with trapezoidal web corrugation. The girders had repetitive geometry and were subjected to four-point bending. Three girders were first tested at a higher stress range of 138 MPa which resulted in fatigue lives between 1.3 and 1.45 million cycles. A lower stress range of 103 was then subjected to another set of three girders which resulted in two run-outs and one premature failure. The two run-outs were terminated after 7.3 million cycles. For the test failing prematurely, a defect was noted in the web-to-flange fillet weld which interrupted the test at 2.56 million cycles. The last two test girders were re-fabricated from one beam of each prior test set. These girders used robotic welding instead of semi-automatic welding to evaluate the effect of welding procedure on fatigue resistance. The results showed that robotic welding increased the fatigue life by approximately 42%. Stress ranges of 110 MPa and 138 MPa gave fatigue lives of 3.5 and 1.99 million cycles, respectively.

2.6.2.6 N. Kotaki, A. Ichikawa, E. Sasaki, C. Miki and T. Hosaka (2003)

In this particular study, two tests were performed on a large scale system level which means that the girders were tested in sets of two. This resulted in two specimens more similar to a complete bridge. The two sets of beams were tested in four-point bending and the nominal stress ranges at the top of the bottom flange were calculated to 150 MPa for both specimens. The fractures occurred in the constant moment zone close to the support after 1.38 and 1.60 million cycles (Kotaki et al., 2003).

2.6.2.7 J. Machacek and M. Tuma (2006)

In 2006, Machacek and Tuma (2006) tested ten beams with sinusoidal corrugations and stiffeners welded to the upper and lower flange under cyclic shear load. The specimens were loaded under three-point bending with shear stress ranges that varied between 30 MPa to 60 MPa which resulted in fatigue lives between 0.77 and 2.72 million cycles. Machacek and Tuma (2006) set the run-out limit for the experiments at 3 million cycles. Four of the specimens reached run-out, two specimens failed due to a crack in the upper flange to web weld, three specimens failed due to a crack in the stiffener to web weld and only one of the tested beams failed in the bottom flange to web weld. Due to the different stiffener and load configuration of these tests compared to other authors mentioned in Section 2.6, the results from this study are not comparable with other studies. Nevertheless, the authors provide valuable recommendations for fatigue design of girders with sinusoidal corrugated webs under shear and transverse loading.

2.6.2.8 Z. Y. Wang, Q. Y. Wang and Y. Q. Zhang (2013)

Two trapezoidal corrugated girders were tested under three-point bending by Wang et al. (2013b). The girders were designed with the same geometry but with different corrugation angles of 30.6° and 45° . The nominal stress ranges were calculated to 147.2 and 118.9 MPa which resulted in fatigue lives of 1.05 and 3.27 million cycles, respectively. However, the first girder with a corrugation angle of 30.6° failed earlier than predicted from a notch in the flame cut edge of the flange plate. In this study, Wang et al. (2013b) tested two additional girders including scallops (weld access holes) in the web. These scallops resulted in high stress concentrations at the cut-outs and a substantially lower fatigue life and are therefore not comparable to the other girders discussed in this thesis.

2.6.2.9 B. Kövesdi and L. Dunai (2014)

Kövesdi and Dunai (2014) tested a total of six girders with trapezoidal corrugation. The overall geometry of the specimens was kept constant while the loading situation, stress ranges and the weld sizes varied. Two specimens were tested under four-point bending and four specimens under three-point bending. The stress ranges varied between 100.6 MPa and 148.81 MPa and the fatigue lives resulted between 1.31 million

and 3.27 million cycles. The two specimens tested under four point bending and one of the specimens tested under three point bending did not fail and reached run-out after 4 million cycles. Noteworthy from the three remaining tests, all loaded with approximately the same stress range, is that when the weld size increased from 3mm to 6mm the fatigue life decreased with almost 40%. This indicates that the weld size of the flange to web connection plays an important role in the fatigue life of these girders. Furthermore, Kövesdi et. al conducted a statistical analysis of the results obtained from their tests together with results obtained from previous authors to determine a characteristic fatigue strength for trapezoidal corrugated web girders. The results suggested that trapezoidal corrugated web girders with corrugation angle $\theta < 39^\circ$ can be considered to be in fatigue detail category 90 according to EN 1993-1-9, although further investigation was suggested to study how the corrugation geometry affects the fatigue detail category.

2.6.2.10 Z.Y. Wang, Q. Y. Wang and R. J. Jiang (2015)

This study is a repetition of the experiment performed by Wang et al. (2013b), described in Section 2.6.2.8. Two girders with the same geometries and stress ranges but with corrugation angles of 30° and 45° were subjected to three-point bending. The specimens with corrugation angles of 30° and 45° failed after 3.31 and 3.24 million cycles, respectively (Wang et al., 2015). Since the location of the final fracture was not reported, additional contact with Z.Y. Wang regarding these girders was sought. Clarification from Wang provided additional information that the girders failed in regions close to the support (approximately 440-500 mm from the support) which was not expected due to a substantially lower stress range in that section (Personal contact, Wang (2020)).

2.6.2.11 J. Xu, H. Sun, S. Chai, W. Sun and B. Zhang (2019)

The largest beam tested under cyclic loading was studied by Xu et al. (2019). The 12 meter long girder with trapezoidal web profile and oblique flanges was tested under four-point bending. A nominal stress range at fracture location of 62.95 MPa resulted in a fatigue life of 5.74 million cycles. The girder failed outside the constant moment zone.

2.6.3 Summary of experimental studies

The review of the experimental results suggests that they are partly confirming and partly contradicting the theoretical predictions in terms of cracking locations along the beams and/or the fatigue life of the details. To increase the comparability of results, the specimens have been condensed to a smaller number of girders. The girders have been sorted by geometry, stiffener configuration and according to recommendations from the guide for statistical analysis for fatigue results (Schneider and Maddox, 2003) and the background document of Eurocode EN 1993-1-9 (Sedlacek et al., 2003).

The tests that have reached run-out or failed prematurely add to the uncertainty in the corresponding fatigue life. This uncertainty can both lead to a significantly lower or higher prediction of the fatigue class and are therefore excluded from further processing. This is supported by recommendations from Schneider and Maddox (2003). It is worth noticing that many experiments have failed prematurely due to weld defects even though inspections were performed prior to testing. This proves the importance of quality welding.

For the geometry of the girders, previous authors have concluded that corrugation type, existence of some structural details (e.g scallops), and loading type change the stress concentration and cracking modes. Therefore the sinusoidal and discrete corrugations, girders with scallops and deviant stiffener configurations are excluded, along with girders tested in shear. Hence, the final girders that are determined to be comparable for post-processing all share trapezoidal corrugations, have not failed prematurely or reached run-out, and have similar loading, cracking, and stiffener situation. The factors that still differ are the individual trapezoidal geometries, stresses, fracture zone, three or four-point bending and in a few cases, the welding procedure.

Two unexpected findings were noticed, namely the fracture zones for the four and three-point bending. Theoretically, due to the additional transverse bending moment, fracture is predicted in the zones where high moment and high shear occur but the experiments show that this is not certain. Approximately half of the girders from the four-point bending cases fail in the constant bending zone which suggests that the transverse bending induced by shear flow is not that significant in these cases. Similarly, for specimens subjected to three-point bending, fracture location is predicted close to where maximum shear and bending stresses occur, thus in the middle of the span. Often, this is a correct predication but a few experiments result in cracking at a distance away from the load position. The properties of all tested specimens and properties of the specimens used for further evaluations can be seen in Table 2.3 and 2.4, respectively.

Table 2.3: Geometrical and testing parameters of all previous studies.

Ref.	LT^1	L_{eff} [mm]	t_w [mm]	h_w [mm]	$t_{f,top}$ [mm]	$b_{f,top}$ [mm]	$t_{f,bot}$ [mm]	$b_{f,bot}$ [mm]	CT^2	θ [°]	R [mm]	H_C^3 [mm]	L_{par} [mm]	L_{inc} [mm]	a_w [mm]	L_{wl} [mm]	$\Delta\sigma_{nom}$ [MPa]	Nf [·10 ⁶]
Harrison	4	3962	6.35	609.6	15.9	293.2	15.9	203.2	SI	-	-	152.4	-	-	6.35	610	185	1.10
Harrison	4	3772	6.35	609.6	15.9	293.2	15.9	203.2	SI	-	-	152.4	-	-	6.35	419	156	2.35
Korashy	4	2740	4	240	10	140	10	110	DI	-	-	78.40	-	-	4	257	216.4	0.47
Korashy	4	2740	4	240	10	140	10	110	DI	-	-	78.40	-	-	4	257	198.10	0.80
Korashy	4	2740	4	240	10	140	10	110	DI	-	-	78.40	-	-	4	257	136.90	2.67
Korashy	4	2740	4	240	10	140	10	110	DI	-	-	78.40	-	-	4	257	132.10	1.80
Korashy	4	2740	4	240	10	140	10	110	DI	-	-	78.40	-	-	4	257	155.80	1.42
Korashy	4	2740	4	240	10	140	10	110	DI	-	-	78.40	-	-	4	257	176.60	1.16
Korashy	4	2740	4	240	10	140	10	110	DI	-	-	78.40	-	-	4	257	208.10	0.59
Korashy	4	2740	4	240	10	140	10	110	DI	-	-	78.40	-	-	4	257	156.30	3.36
Korashy	4	1700	4	230	10	110	10	110	DI	-	-	78.40	-	-	4	257	184.40	1.34
Korashy	4	1700	4	230	10	110	10	110	DI	-	-	78.40	-	-	4	257	171.30	1.02
Korashy	4	1700	4	230	10	110	10	110	DI	-	-	78.40	-	-	4	257	163.20	1.74
Rodriguez	4	3750	2	400	10	120	10	120	TR	40	-	106	129.54	165	-	500	108	0.40
Rodriguez	4	3750	2	400	10	120	10	120	TR	40	-	106	129.54	165	-	500	88.6	1.35
Rodriguez	3	2500	2	400	10	120	10	120	TR	40	-	106	129.54	165	-	500	80.66	4.72
Rodriguez	4	3750	2	400	10	120	10	120	TR	40	-	106	129.54	165	-	500	99.6	0.65
Rodriguez	4	3500	2	400	10	120	10	120	TR	40	-	106	129.54	165	-	500	96.18	1.70
Rodriguez	4	3500	2	400	10	120	10	120	TR	40	-	106	129.54	165	-	500	101	3.28
Ibrahim	4	5859	3	500	12.5	150	12.5	150	TR	36.9	27	75	117	125	5	434	97.14	2.61
Ibrahim	4	5859	3	500	12.5	150	12.5	150	TR	36.9	27	75	117	125	5	434	64.71	17.61
Ibrahim	4	5859	3	500	12.5	150	12.5	150	TR	36.9	27	75	117	125	5	434	142.39	1.60
Ibrahim	4	5859	3	500	12.5	150	12.5	150	TR	36.9	27	75	117	125	5	434	137.21	1.81
Ibrahim	4	5859	3	500	12.5	150	12.5	150	TR	36.9	27	75	117	125	5	434	161.80	1.24
Ibrahim	4	5859	3	500	12.5	150	12.5	150	TR	36.9	27	75	117	125	5	434	97.14	9.34
Abbas	4	7000	6	1200	20	225	20	225	TR	36.9	120	150	300	170	8	1000	138	1.42
Abbas	4	7000	6	1200	20	225	20	225	TR	36.9	120	150	300	170	8	1000	138	1.45
Abbas	4	7000	6	1200	20	225	20	225	TR	36.9	120	150	300	170	8	1000	138	1.30
Abbas	4	7000	6	1200	20	225	20	225	TR	36.9	120	150	300	170	8	1000	103	7.32
Abbas	4	7000	6	1200	20	225	20	225	TR	36.9	120	150	300	170	8	1000	103	2.56
Abbas	4	7000	6	1200	20	225	20	225	TR	36.9	120	150	300	170	8	1000	103	7.65

2. Literature review

Abbas	4	7000	6	1150	20	225	20	225	TR	36.9	120	150	300	170	8	1000	138	1.98
Abbas	4	7000	6	1150	20	225	20	225	TR	36.9	120	150	300	170	8	1000	110	3.50
Kotaki	4	6000	4.5	600	19	300	12	300	TR	30	75	150	300	150	5	500	150	1.38
Kotaki	4	6000	4.5	600	19	300	12	300	TR	30	75	150	300	150	5	500	150	1.60
Machacek	3	1700	2	500	10	200	10	200	SI	-	-	40	-	-	-	310	20.42	2.11
Machacek	3	1700	2	500	10	200	10	200	SI	-	-	40	-	-	-	310	20.42	1.42
Machacek	3	1700	2	500	10	200	10	200	SI	-	-	40	-	-	-	310	20.42	0.77
Machacek	3	1700	2	500	10	200	10	200	SI	-	-	40	-	-	-	310	20.40	3.07
Machacek	3	1700	2	500	10	200	10	200	SI	-	-	40	-	-	-	310	12.25	3.03
Machacek	3	1700	2	500	10	200	10	200	SI	-	-	40	-	-	-	310	16.34	3.07
Machacek	3	1700	2	500	10	200	10	200	SI	-	-	40	-	-	-	310	18.38	3.02
Machacek	3	1700	2	500	10	200	10	200	SI	-	-	40	-	-	-	310	24.51	0.98
Machacek	3	1700	2	500	10	200	10	200	SI	-	-	40	-	-	-	310	24.51	1.47
Machacek	3	1700	2	500	10	200	10	200	SI	-	-	40	-	-	-	310	24.51	2.72
Wang(2013)	3	1600	4	248	6	88	6	88	TR	30.6	-	64	82	82	3	320	147.2	1.05
Wang(2013)	3	1600	4	248	6	88	6	88	TR	45	-	64	82	82	3	320	118.9	3.20
Kövesdi	4	6750	6	500	20	225	20	225	TR	39	60	139	210	212	6	750	100.6	4.49
Kövesdi	4	6750	6	500	20	225	20	225	TR	39	60	139	210	212	6	750	110.63	4.16
Kövesdi	3	6750	6	500	20	225	20	225	TR	39	60	139	210	212	6	750	146.7	1.31
Kövesdi	3	6750	6	500	20	225	20	225	TR	39	60	139	210	212	6	750	140.27	1.33
Kövesdi	3	6750	6	500	20	225	20	225	TR	39	60	139	210	212	3	750	148.81	3.27
Kövesdi	3	6750	6	500	20	225	20	225	TR	39	60	139	210	212	3	750	127.54	15
Wang(2015)	3	1600	4	248	6	88	6	88	TR	30	-	64	82	82	3	320	147.9	3.31
Wang(2015)	3	1600	4	248	6	88	6	88	TR	45	-	64	82	82	3	320	117.5	3.24
Xu	4	11500	6.4	1650	25	424	25	297	TR	45	100	160	340	226	7	1000	62.95	5.74

Notes: ¹Loading type: 4 = Four-point bending, 3 = Three-point bending. ²Corrugation type: TR = Trapezoidal corrugations, SI = Sinusoidal corrugations, DI = Discrete corrugations. ³Height of corrugations (corrugation depth)

Table 2.4: Geometrical parameters of trapezoidally corrugated girders.

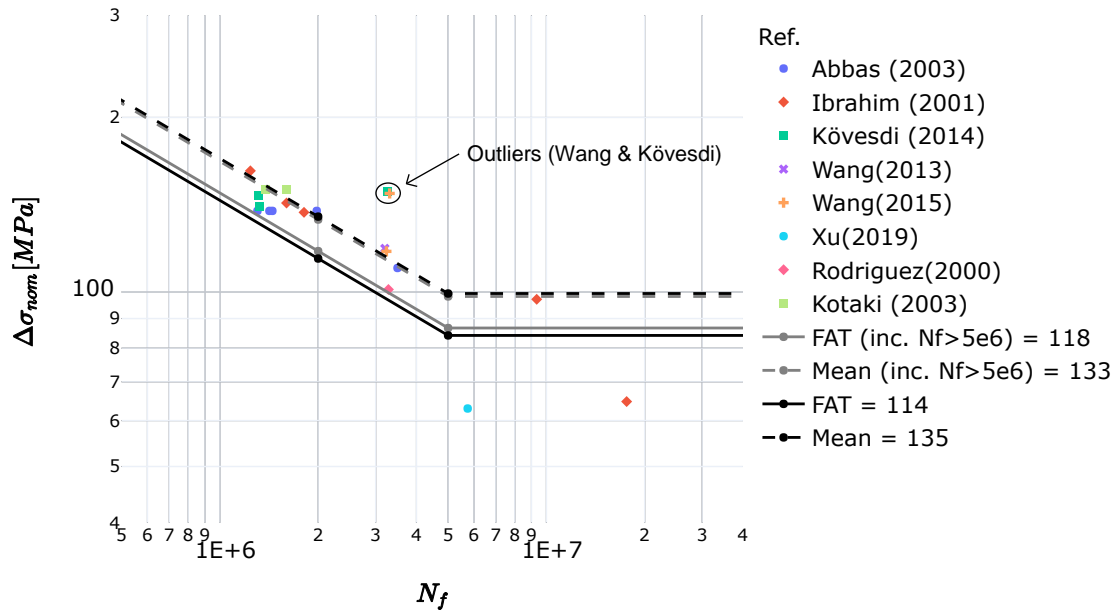
Ref.	LT^1	L_{eff} [mm]	t_w [mm]	h_w [mm]	$t_{f,top}$ [mm]	$b_{f,top}$ [mm]	$t_{f,bot}$ [mm]	$b_{f,bot}$ [mm]	CT^2	θ [°]	R [mm]	H_C^3 [mm]	L_{par} [mm]	L_{inc} [mm]	a_w [mm]	L_{wl} [mm]	$\Delta\sigma_{nom}$ [MPa]	N_f [$\cdot 10^6$]
Rodriguez	4	3500	2	400	10	120	10	120	TR	40	-	106	129.54	165	-	500	101	3.28
Ibrahim	4	5859	3	500	12.5	150	12.5	150	TR	36.9	27	75	117	125	5	434	64.71	17.61
Ibrahim	4	5859	3	500	12.5	150	12.5	150	TR	36.9	27	75	117	125	5	434	142.39	1.60
Ibrahim	4	5859	3	500	12.5	150	12.5	150	TR	36.9	27	75	117	125	5	434	137.21	1.81
Ibrahim	4	5859	3	500	12.5	150	12.5	150	TR	36.9	27	75	117	125	5	434	161.80	1.24
Ibrahim	4	5859	3	500	12.5	150	12.5	150	TR	36.9	27	75	117	125	5	434	97.14	9.34
Abbas	4	7000	6	1200	20	225	20	225	TR	36.9	120	150	300	170	8	1000	138	1.42
Abbas	4	7000	6	1200	20	225	20	225	TR	36.9	120	150	300	170	8	1000	138	1.45
Abbas	4	7000	6	1200	20	225	20	225	TR	36.9	120	150	300	170	8	1000	138	1.30
Abbas	4	7000	6	1150	20	225	20	225	TR	36.9	120	150	300	170	8	1000	138	1.98
Abbas	4	7000	6	1150	20	225	20	225	TR	36.9	120	150	300	170	8	1000	110	3.50
Kotaki	4	6000	4.5	600	19	300	12	300	TR	30	75	150	300	150	5	500	150	1.38
Kotaki	4	6000	4.5	600	19	300	12	300	TR	30	75	150	300	150	5	500	150	1.60
Wang(2013)	3	1600	4	248	6	88	6	88	TR	45	-	64	82	82	3	320	118.9	3.20
Kövesdi	3	6750	6	500	20	225	20	225	TR	39	60	139	210	212	6	750	146.7	1.31
Kövesdi	3	6750	6	500	20	225	20	225	TR	39	60	139	210	212	6	750	140.27	1.33
Kövesdi	3	6750	6	500	20	225	20	225	TR	39	60	139	210	212	3	750	148.81	3.27
Wang(2015)	3	1600	4	248	6	88	6	88	TR	30	-	64	82	82	3	320	147.9	3.31
Wang(2015)	3	1600	4	248	6	88	6	88	TR	45	-	64	82	82	3	320	117.5	3.24
Xu	4	11500	6.4	1650	25	424	25	297	TR	45	100	160	340	226	7	1000	62.95	5.74

Notes: ¹Loading type: 4 = Four-point bending, 3 = Three-point bending. ²Corrugation type: TR = Trapezoidal corrugations, SI = Sinusoidal corrugations, DI = Discrete corrugations. ³Height of corrugations (corrugation depth)

2.6.4 Analysis of experimental studies

From the comparable data gathered in the previous chapter, two S-N curves for trapezoidal corrugated web girders have been established as shown in Figure 2.11. Since the number of data points is limited, the best-fit regression lines are estimated with a fixed slope of 1:3 as recommended by the guide on statistical analysis of fatigue data for welded details (Schneider and Maddox, 2003). The solid black and gray S-N curves represent a fatigue class (95% confidence limit) where data points over 5 million cycles have been excluded and where data points over 5 million cycles have been included, respectively. The exclusion of data points over 5 million cycles is based on recommendations from the background document of EN 1993-1-9 (Sedlacek et al., 2003) and Schneider and Maddox (2003). These recommendations are provided to accurately estimate the best-fit regression line with regard to the constant amplitude fatigue limit (CAFL). However, since every valid data point is valuable and the number of valid data points is restricted, an S-N curve is also calculated, including data points over 5 million cycles to investigate their effect on the fatigue class. The inclusion of the three points located above 5 million cycles is motivated by the fact that the fatigue response in reality often shows fatigue damage even for stress ranges below the predefined CAFL. As can be seen in Figure 2.11, the difference between the two characteristic S-N curves are not that significant and the suggestion is therefore to follow the recommendations from EN 1993-1-9 and the guide from Schneider et. al, which in this case gives a more conservative fatigue class for the observed detail.

Two points with a low stress range can be noted from Rodriguez (2000) and Xu et al. (2019). These points are located above 5 million cycles and should be excluded from S-N curve calculations by recommendations from Eurocode (EN:1993, 2005) and the guide on statistical analysis of fatigue data by Schneider and Maddox (2003). Nonetheless, the deviance of these data points compared to the rest of the data points is interesting. These two specimens were tested at a relatively low stress range which in general explains their ability to sustain a large number of load cycles even though they are found below the CAFL. The first explanation to this is that fatigue still can occur below the CAFL and therefore not fully representative of the reality. An explanation for the less number of cycles for the data point produced by Xu et al. (2019) compared to Rodriguez (2000) could be that this specimen is substantially larger than the rest of the specimens seen in Figure 2.11, and as stated by Fisher et al. (1974), larger specimens in general shows lower fatigue lives than smaller specimens. Another explanation could be that the oblique flanges on this specimen decrease the fatigue performance, although Xu et al. suggest that the inclined angle of the oblique flanges should have a relatively small impact on the fatigue performance of the girder, see Section 2.5.6. A third explanation could be that this specimen has relatively large welds and high corrugation angle compared to the other specimens, which should decrease the fatigue performance of the specimen.



Notes: Solid black line corresponds to fatigue class (95% confidence limit) excluding points over 5 million cycles, solid grey line corresponds to fatigue class (95% confidence limit) including points over 5 million cycles, dashed grey and black lines corresponds to mean fatigue classes.

Figure 2.11: Summary of previous fatigue tests on trapezoidal CWG.

To post-process the data gathered in Figure 2.11 and to evaluate the findings presented in Sections 2.4 and 2.5, comparisons were performed between tests and parameters for individual specimens. Two distinct outliers can be recognized in Figure 2.11, namely two points from Wang (2015) and Kövesdi (2014). The most probable explanation to this, found in the previous sections is that the weld thicknesses of these two specimens are substantially lower than for most of the remaining specimens (3mm compared to 5-8mm for most of the remaining specimens). The effect of weld size on fatigue performance on corrugated web beams was reported by Kövesdi and Dunai (2014) where it could be seen that by increasing the weld size from 3mm to 6mm, the fatigue life decreased substantially due to larger internal defects, increased residual stresses and larger stress concentrations at weld toe (Fisher et al., 1970, 1974). There are however differences in other critical parameters between these points which should have an effect on the fatigue performance. For example, the outlying point from Kövesdi has a larger corrugation angle than the deviant point from Wang, which should decrease the fatigue performance in comparison to the aforementioned point. The ratio between additional transverse bending and global bending moment of the bottom flange is concurrently larger for the point from Wang. This suggests a counteractive behaviour between parameters, resulting in the two points with different geometries still showing similar fatigue performance. The remaining specimens from Wang (2013) and Wang (2015) also have weld thickness equal to 3mm but still performs considerably worse than the outlier by Wang, this can again be originated to their substantially higher corrugation angle.

The specimens of Ibrahim follow the regression line relatively accurate since the girders have the same geometry with no well-distinguished parameter and are tested in different stress levels. A grouped scatter can be seen between 1.4 and 1.6 million cycles. These girders are from Kotaki, Kövesdi and Abbas and are tested in similar stress ranges. The girders result in similar fatigue lives probably since the geometries from these authors are similar with only a few exceptions. Abbas data point shows marginally worse performance probably due to the higher weld thickness of 8 mm. Kövesdi and Kotaki however, have similar weld sizes (5-6 mm) but a large difference in corrugation angle. The specimens from Kotaki have a low corrugation angle of 30° compared to Kövesdi's 39° which lead to a small increase in the fatigue resistance.

Abbas experiment also produced two deviant points which demonstrate a slightly higher fatigue performance than the rest of the specimens in the same test, this can be explained by that these two specimens were both robotic welded while the remaining three specimens were semi-automatic welded which would result in poorer weld quality and thus poorer fatigue performance.

2.6.4.1 Statistical analysis

To statistically prove the observations in the above section regarding the significance of single geometry parameters on fatigue performance, statistical analyses are performed. The aim of the statistical evaluation is to determine if the data in Figure 2.11 belong to different populations based on geometry parameters, which would yield different fatigue classes. Statistical evaluations are useful when larger data sets with numerous parameters are involved since it can be challenging to assert an overlying trend. In the best practice guide for statistical evaluation by Schneider and Maddox (2003), several statistical tests are provided to evaluate statistical differences between data sets. Particularly tests that evaluate the statistical equivalence between two sets of S-N curves have been used in this analysis. These tests include whether the slopes or the intercepts of two S-N curves are consistent. As previously mentioned, a fixed slope of 1:3 is chosen for the calculation of the S-N curves in this thesis and a test whether the slopes of two S-N curves are consistent is therefore unnecessary. Only the statistical equivalence between the intercepts of two S-N curves was therefore tested. Equation 2.5 from the recommendations by Schneider and Maddox (2003) was used to evaluate the intercepts and is presented below. If the condition of Equation 2.5 is true, the null hypothesis is accepted meaning that the two data sets belong to the same population and no statistical difference between the intercept of the two regression lines can be observed, see Figure 2.12. Thus, if the null-hypothesis holds true, no statistical difference in fatigue performance can be observed. The data points included in the statistical evaluation are those that are located below 5 million cycles in Figure 2.11.

$$|\overline{\log A_1} - \overline{\log A_2}| \leq t \sqrt{\left(\frac{1}{n_1} + \frac{1}{n_2} + \frac{\overline{\log S_1}^2}{\sum_{i=1}^{n_1} (\log S_{1,i} - \overline{\log S_1})^2} + \frac{\overline{\log S_2}^2}{\sum_{j=1}^{n_2} (\log S_{2,j} - \overline{\log S_2})^2} \right) \sigma_e^2} \quad (2.5)$$

Where:

$\overline{\log A_i}$	Estimated intercept of regression line
t	Appropriate percentage point of t-distribution
n_i	Number of data points
$\overline{\log S_i}$	Mean value of stress ranges
$\sigma_e^2 = \frac{f_1 \hat{\sigma}_1^2 + f_2 \hat{\sigma}_2^2}{f_1 + f_2}$	Estimate of common variance of samples
$f_i = (n_i - 2)$	Degrees of freedom
$\hat{\sigma}_i^2 = \frac{\sum (\log N_i - \log \hat{N}_i)^2}{f_i}$	Variance of data set

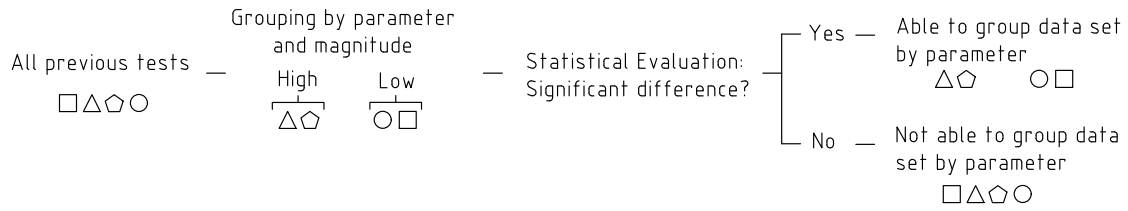


Figure 2.12: Procedure of Statistical Evaluation.

Previous knowledge from sections 2.4, 2.5 and Eurocode suggests a number of parameters that should have a significant effect on the fatigue performance and the data were therefore sorted and evaluated based on these. The factors studied were the corrugation angle θ , bend radius R , weld thickness a_w , flange thickness t_f , l/t_f -ratio, $R/R_{circular}$ -ratio and the " σ_t/σ_{nom} -ratio".

The corrugation angle and bend radius are included since they are stated by numerous authors to be major factors influencing the fatigue resistance. This has been proven by authors analytically and numerically as well for experiments studying small size weldments. The flange thickness, weld size and l/t_f -ratio are parameters commonly appearing in EN 1993 for determination of correct fatigue class of a structural detail. Therefore, they are also included to see their influence on fatigue performance. As explained in Section 2.5.2, Ibrahim (2001) concluded by numerical studies that by increasing the bend radius to one fourth the length of an equivalent sinusoidal shaped girder, the stress concentration could be significantly reduced and therefore the $R/R_{circular}$ -ratio is investigated. The σ_t/σ_{nom} -ratio is a hypothesis that a trend could be seen if a certain CWG geometry would result in a high transverse bending stress compared to the longitudinal stress in the flange. If the

hypothesis would hold true, many factors would be indirectly included in this ratio since $\theta, L_{par}, L_{inc}, H_C$ and h_w are needed to calculate σ_t . The additional transverse bending stresses were calculated for the girders according to the simplified fictitious load model, according to equation 2.3 by Kövesdi et al. (2012)

The above-mentioned factors are expected to influence the fatigue performance of the specimens and the data are therefore initially sorted into batches with high and low values. If a significant difference is found, the data will be further divided. Table 2.5 shows the parameters studied in the statistical analysis and the ranges for the high and low categories.

Table 2.5: Factors tested for statistical significance.

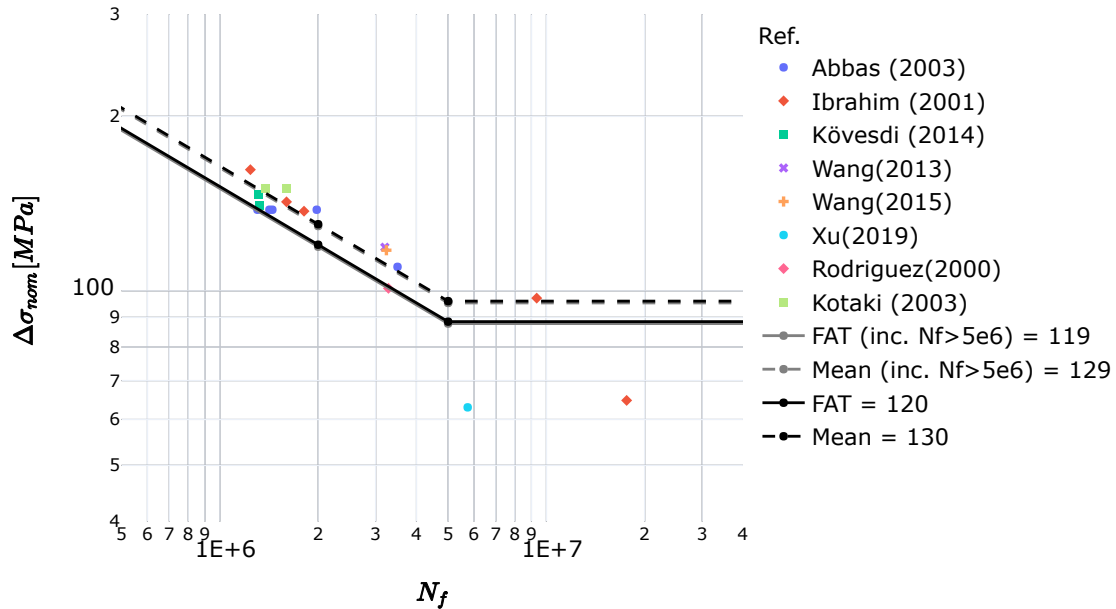
Parameter	Low cat.	High cat.
Corrugation angle, θ	$\theta < 37^\circ$	$\theta \geq 37^\circ$
Bend radius, R	$R \leq 60\text{mm}$	$R > 60\text{mm}$
Flange thickness, t_f	$t_f < 15\text{mm}$	$t_f \geq 15\text{mm}$
l/t_f	$l/t_f < 85$	$l/t_f \geq 85$
$R/R_{circular}$	$R/R_{circular} < 0.25$	$R/R_{circular} \geq 0.25$
σ_t/σ_{nom}	$\sigma_t/\sigma_{nom} < 0.17$	$\sigma_t/\sigma_{nom} \geq 0.17$
Weld thickness, a_w	$a_w < 5\text{mm}$	$a_w \geq 5\text{mm}$

The statistical evaluation did not indicate a significant difference between any of the data batches, which does not conform with previous knowledge. This could however be originated to a number of reasons and/or a combination of them. One reason could be the general scatter often seen in fatigue test data as a result of several factors, such as high variability of residual stresses and internal weld defects. Another reason is the low number of specimens. This is problematic for statistical analysis since every individual point has a high impact on the result. Finally, there is a possibility that the complex combined action of several parameters trumps the influence of one single parameter.

As the statistical evaluation was unsuccessful in grouping the data, further analyses are performed for the whole data set. Since highly deviant data points influence statistical results substantially in small data sets, those points are normally excluded. This is also recommended by Schneider and Maddox (2003) and therefore, the outlying data points from Kövesdi and Wang are ignored in order to further investigate the cluster closer to the mean regression line.

As expected, when calculating the regression lines for the reduced data set, the mean lines are lowered when these high values are excluded. However, the characteristic curves result in higher fatigue classes. This is explained by significantly reduced scatter and standard deviation which results in a tighter safety margin, see Figure 2.13. A second statistical evaluation is performed for the reduced data set using the same parameters shown in Table 2.5, including weld size. Still, no significant difference can be determined for the data. As stated previously, it probably owes to

the large number of parameters affecting the fatigue resistance which could therefore balance each other out when they are not considerably different.



Notes: Solid black line corresponds to fatigue class (95% confidence limit) excluding points over 5 million cycles, solid grey line corresponds to fatigue class (95% confidence limit) including points over 5 million cycles, dashed black and grey line corresponds to mean fatigue classes.

Figure 2.13: Summary of previous fatigue tests on trapezoidal CWG, excluding outliers.

Alternatively, visual examination of the reduced data set is carried out by plotting the values with regard to different parameters. When plotting against flange thickness, it can be seen that the points are roughly grouped into two clusters, with the exception of two values from Abbas' experiments, see Figure 2.14. From the group where the girders have high flange thickness, the points from Abbas show higher fatigue resistance compared to the other points from the same author. These points appear to have no extraordinary geometry. The only difference was that they belonged to girders that were produced by robotic welding instead of a semi-automatic procedure. This finding shows the importance of weld quality and could therefore be questioned whether the results from Abbas are comparable to the other CWGs.

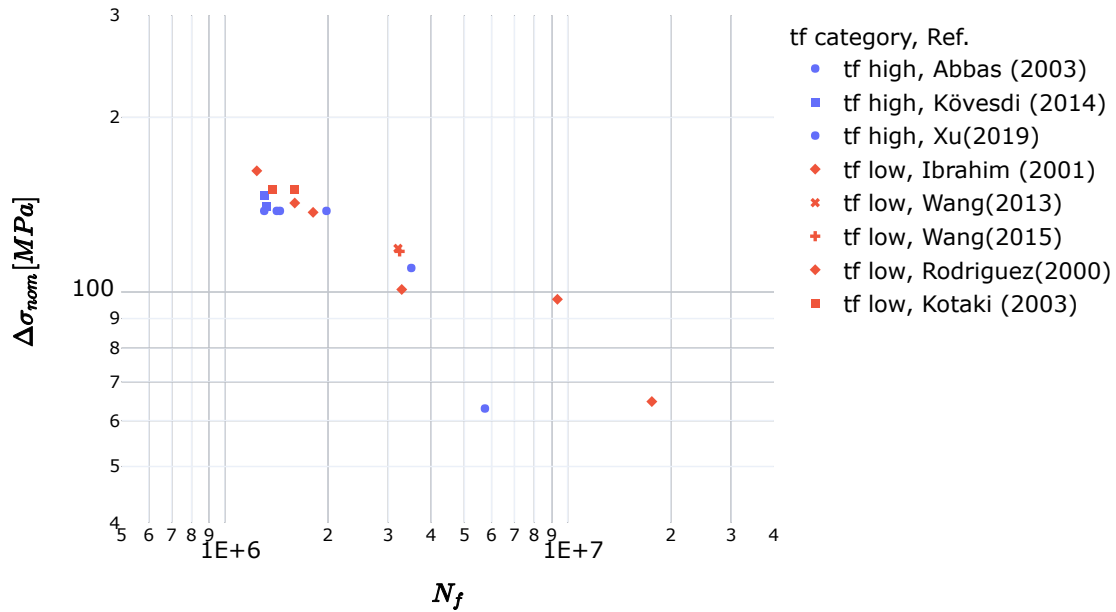


Figure 2.14: Data points grouped by flange thickness category.

After excluding these points, it can be seen that the scatter is more distinctively divided into two groups with low and high flange thickness, see Figure 2.16. The grouping is supported by previous knowledge that flanges with low thickness experience a high stress gradient effect, meaning that stresses are rapidly decreasing from the surface to the middle of the thickness. The gradient effect results in that an appearing crack quickly grows outside a high stress zone, which could stop the crack propagation, see Figure 2.15. This finding suggests that similar to many other welded details in Eurocode, corrugated web girders could be grouped in different fatigue classes in regard to their flange thickness. However, more test data is needed to prove this statistically.

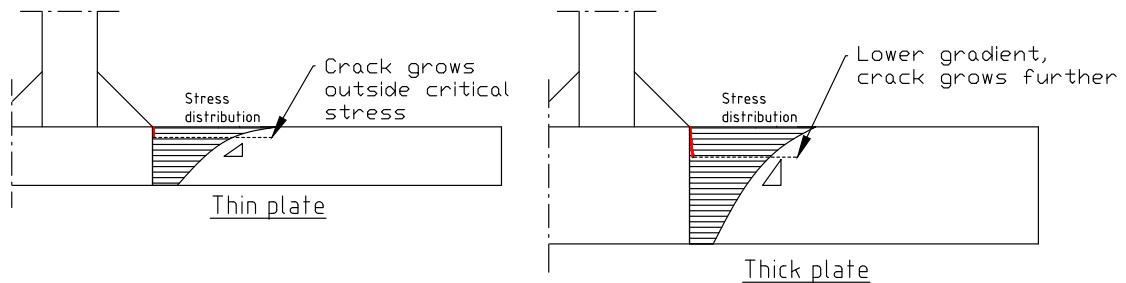


Figure 2.15: Stress gradient effect on thin and thick plates.

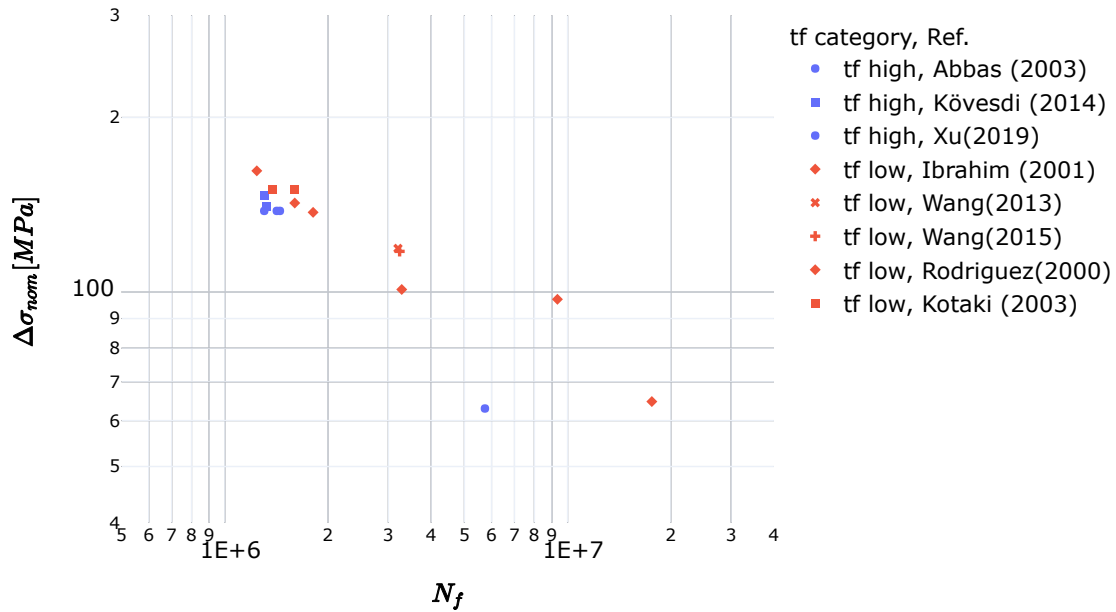
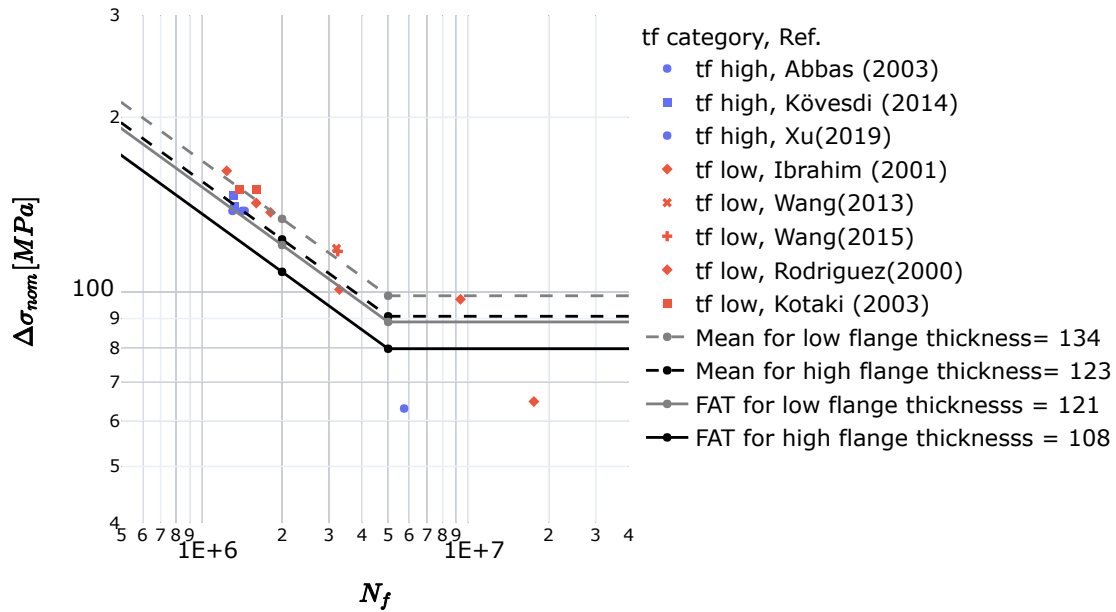


Figure 2.16: Data points grouped by flange thickness category, excluding points from Abbas.

When calculating the regression lines based on this grouping, two different characteristic fatigue classes can be distinguished, namely FAT 108 and FAT 121, see Figure 2.17. It is uncertain that these fatigue categories are precise but it could still provide an indication of the effect of flange thickness on the fatigue performance of CWGs. Furthermore, when selecting all the valid trapezoidal points (excluding the outliers as recommended by Schneider and Maddox (2003)), their characteristic fatigue category falls into a fatigue class 120, see Figure 2.13, which is higher than what previous authors have suggested.



Notes: Solid black and grey lines corresponds to fatigue classes (95% confidence limit) excluding points over 5 million cycles, dashed black and grey line corresponds to mean fatigue classes excluding points over 5 million cycles.

Figure 2.17: Fatigue classes by flange thickness category.

2.7 Discussion of literature review

The conclusions from numerical and analytical studies conform generally well with each other, agreeing on many stress raising parameters. As mentioned earlier, the experimental results also conform relatively well with numerical and analytical studies within the same test, but they do not agree when comparing tests from different authors. This is an interesting finding that both validate numerical and analytical results, and acknowledges the complexity of interaction between parameters and the importance of consistent conditions when performing fatigue testing.

Since the nominal stress method is a conventional method used to establish the fatigue performance of welded specimens, the stress range where the final fracture crack is expected is also calculated for every specimen. These stresses are then compared to the actual nominal stresses at the final crack location and the results show large differences. Using the theoretical nominal stresses lead to a substantially higher scatter due to the fact that the cracking often appears at locations where lower primary bending stresses are present. Therefore, the applicability of using nominal stresses based on only primary bending when designing CWGs, which is the current recommendation in Eurocode (EN:1993, 2005), would lead to a conservative prediction of the fatigue life.

Both Abbas (2003) and Kövesdi et al. (2012) recommend numerical analyses, especially for girders with multiple number of wavelengths due to the complexity in analytical methods to best predict the structural response for a corrugated structure. However, many numerical analyses are still not able to capture where the final fracture occur which should be considered when designing CWGs.

2.8 Conclusion of literature review

With the literature review presented in this chapter, it becomes evident that the nominal stress method based on primary bending stresses leaves more to be desired when it comes to predicting where along the girder the crack will initiate. It is stated several times in the previous sections that the transverse bending of the flanges can have a significant influence on the longitudinal stress component in the flanges. However, the effect of the transverse bending of the flanges on the geometric stress at the S-point has not been studied in the literature. Further investigation on this could give significant insight into where along the girder the crack can be expected to initiate. By studying the relation between the longitudinal nominal stress, the additional longitudinal stress from transverse bending and the geometric stress, an understanding for the stress state at critical points along the girder can be achieved which serves a great purpose when designing bridges with corrugated web girders.

Furthermore, the literature does not provide a thorough and distinct way of how to efficiently study the structural hot spot stress (SHSS) at the S-points along the girder in finite element modelling. Insight in this will provide valuable information for future researchers studying behaviour of CWGs. The following chapters of this thesis are therefore providing a suggestion of a structured way of modelling CWGs along with a comparison of different SHSS assessment methods available in the literature, intending to find the most efficient model in terms of computational cost.

3

Methods

As mentioned in Section 2.8, an investigation on the relation between nominal stress coming from primary bending, transverse bending stress, and geometric stress, also known as structural hot spot stress, at S-points along the girder will be performed. In order to do this, several girders with varying geometries are modelled using the commercial finite element software ABAQUS. In the following chapter the modelling methods, type of elements, and stress evaluation methods used are presented and discussed.

3.1 Analysis procedure

Previous authors have concluded that transverse bending of the flanges due to eccentric shear flow in the web affects the stress state in the flanges and consequently the fatigue performance. Although, the effect on the stress concentration at the fatigue critical points due to transverse bending has not been investigated. It is important to study this effect prior to performing further studies on single parameters and their interactions in order to determine where along the girder a crack is expected.

As previously mentioned, the maximum transverse bending moment (for the worst load and support condition with respect to transverse bending) can be described by equation 2.4, first defined by Kövesdi et al. in 2012 (Kövesdi et al., 2012). This equation is a function of the eccentric shear flow in the web and a few geometric parameters. The equation is repeatedly presented below.

$$M_{t,max} = \frac{V \cdot H_c}{2 \cdot h_w} \cdot (2 \cdot L_{par} + L_{inc,hor}) \quad (2.4)$$

With equation 2.4 as background, four girder geometries that will result in a spectrum of transverse bending moment values applied to the flanges are chosen in order to study their influence on the structural hot spot stresses at the S-points along the girder. In addition to this, the parameter space chosen for the girder geometries is chosen based on CWG geometries for bridges presented in Karlsson (2018). This is done to attain cases closer to real bridge girders. The majority of the geometric parameters are kept constant between studied girders in order to isolate the effect on transverse bending to one parameter connected to the magnitude of shear flow (h_w) and one parameter connected to the corrugation geometry (L_{par}). The common geometry parameters for the models are presented in Table 3.1.

Table 3.1: Common geometry parameters for test girders.

Parameter	Dimension
Web thickness, t_w [mm]	9
Flange width, b_f [mm]	300
Flange thickness, t_f [mm]	30
Corrugation depth, H_c [mm]	200
Projected fold length, $L_{inc,hor}$ [mm]	265.4
Corrugation angle, θ [°]	37
Bend radius, R [mm]	60
Weld thickness, a_w [mm]	9

The varying parameters for this analysis are the height of the web and the length of the parallel fold. The web height is chosen to study the magnitude of shear flow on the fatigue critical point while the parallel fold length is chosen to study the effect of change in corrugation geometry. These parameters are suggested to be the most influential parameters with regard to local transverse bending moment according to the formerly mentioned Equation 2.4. The matrix for the varying parameters is presented in Table 3.2. This results in two long girders with different heights (girders 2 and 4), and two shorter girders with different heights (girders 1 and 3).

Table 3.2: Variable parameters for test girders.

	CWG 1	CWG 2	CWG 3	CWG 4
Web height, h_w [mm]	1500	1500	3000	3000
Parallel fold length, L_{par} [mm]	200	400	200	400

The four CWGs are modelled with the same number of corrugation wavelengths, subjected to four-point bending. The total number of wavelengths is set to 15 and the point loads are located at a distance of one-third of the full effective length from the supports, similar to previous experiments. Hence, the models are divided into three equal sections consisting of five full wavelengths where the middle section is theoretically experiencing a constant bending moment and the other sections being under combined shear and moment action, see Figure 3.1. This allows for a study of two regions along the girder where 1) the longitudinal stress state in the flanges is governed only by primary bending moment and 2) where the longitudinal stress state in the flanges is governed by both primary bending moment and shear flow in the web. In order to study the influence of transverse bending of the flanges on SHSS at the S-points, a comparison between the stress concentration factor (SCF) in the combined moment and shear region and the constant moment region is made. In this case, the stress concentration factor is equal to the ratio between the hot spot stress and the longitudinal stress coming from primary bending in the same section, $SCF = \sigma_{SHSS}/\sigma_p$. A magnitude of 300kN was applied to both point loads for every girder.

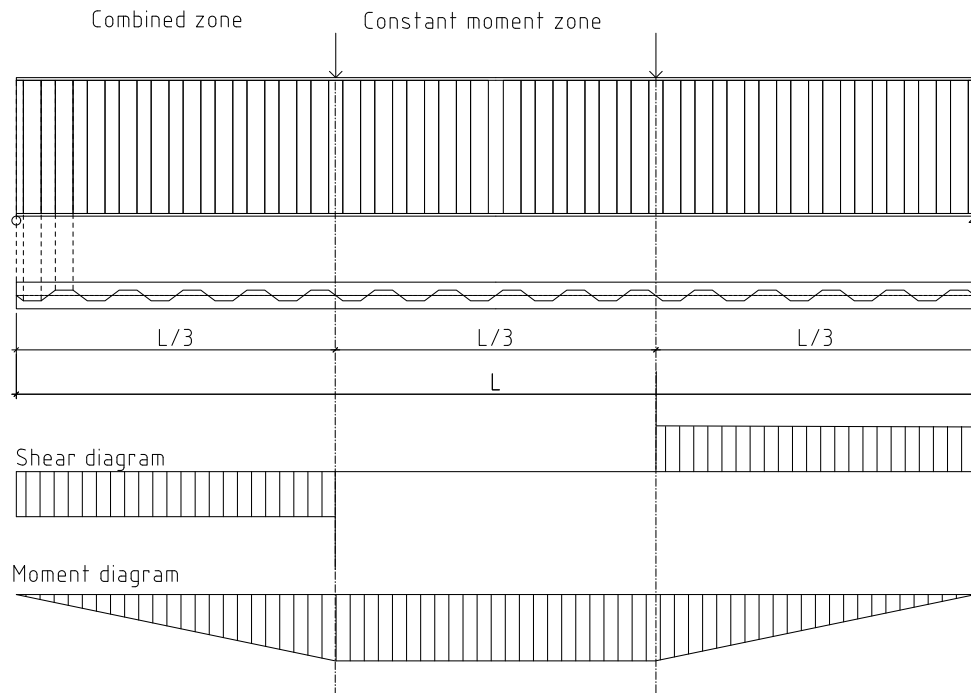


Figure 3.1: FE Experiment setup.

As can be seen in Figure 3.1, the sectional forces are analytically explained with "sharp transitions" under the point loads since the load distribution through the depth of the girders is neglected. In reality and subsequently in FE-modelling, local stresses at the point of application of concentrated loads are distributed through the depth of the girders, resulting in a more smooth transition of shear force under point loads.

Therefore, to assure a stress concentration factor that is excluding any effect of shear force, a girder subjected to pure moment is modelled as shown in Figure 3.2.

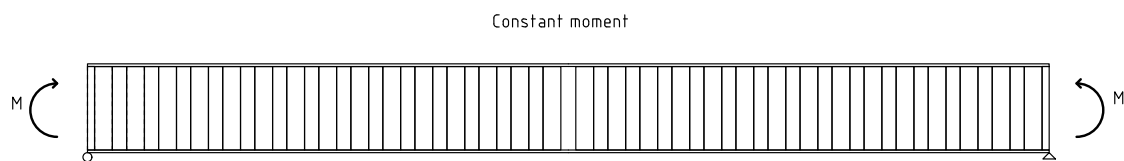


Figure 3.2: Constant moment applied to girders.

Furthermore, one corrugation wavelength welded to a flange plate subjected to uniform tension is modelled, see Figure 3.3. This is done to investigate if a simplified tension model could represent a whole CWG under pure bending. As suggested by Wang et al. (2013a).

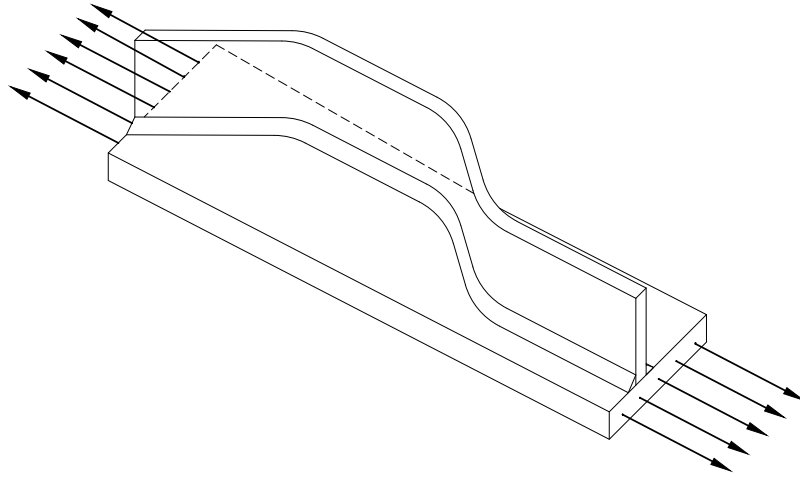


Figure 3.3: Tensile forces applied to the flange detail of one wavelength.

3.2 Structural hot spot stress methods

In this section, a brief introduction to the concept of geometric or hot spot stress and how it can be calculated according to the design codes (Hobbacher, 2016; EN:1993, 2005) is presented. The methods are further used and compared for the girders mentioned in Section 3.1.

In the vicinity of a weld toe, the stress distribution through the thickness of the plate becomes highly non-linear, see Figure 3.4. This non-linear stress distribution, also referred to as notch-stress, owes to the overall change in geometry, the change in stiffness, and to the local geometry of the weld toe itself. According to the International Institute of Welding (IIW) standard, the structural or geometric stress, also known as structural hot spot stress, is the stress that includes all stress raising effects of a structural detail excluding the effect of local profile of the weld (Hobbacher, 2016). In other words, the non-linear peak stress caused by the weld toe geometry is to be excluded from the notch-stress in order to achieve the hot spot stress. This is typically done by linearly extrapolating stresses that are located at a distance away from the weld toe. The exclusion of the non-linear peak stress is sought due to three reasons. Firstly, it provides a consistent way of determining the hot spot stress since a single-valued solution can be achieved. Secondly, it is reasonable since the local weld geometry is usually not known in the design of a welded detail. Thirdly, the peak stress is captured on the resistance side since the SN-curves are obtained from fatigue testing. Additionally, the exclusion of the peak stress provides a way to avoid the infinite stress concentration forming at weld toes in finite element analyses due to sharp transitions between weld toe and plate.

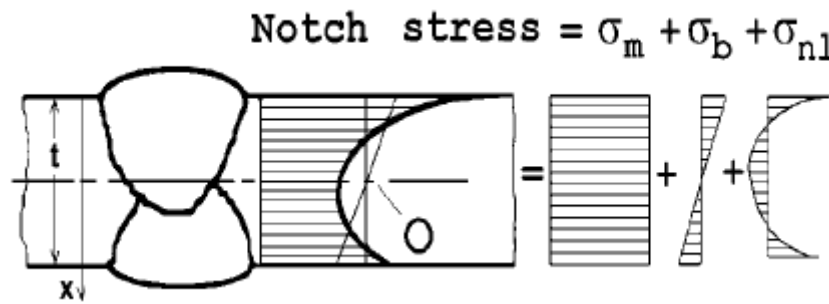


Figure 3.4: Notch stress at a weld toe (Hobbacher, 2016).

Besides the definition mentioned above, IIW also defines two types of hot spot stresses in its standard (Hobbacher, 2016) as shown in Figure 3.5. *Type a* hot spots are associated with weld toes on a plate surface, while *type b* hot spots are associated with weld toes on a plate edge. The reason for dividing these hot spots into two categories is the difference in stress distribution through the thickness of the cracked plate. In *type a* hot spots, the distribution varies greatly through the thickness while for *type b* hot spots, it is more uniform. For linearization of stress profiles in *type a* hot spots, the thickness of the cracked plate is therefore considered as a parameter while in *type b* hot spots, the thickness of the plate is not considered (Al-Emrani and Aygül, 2013).

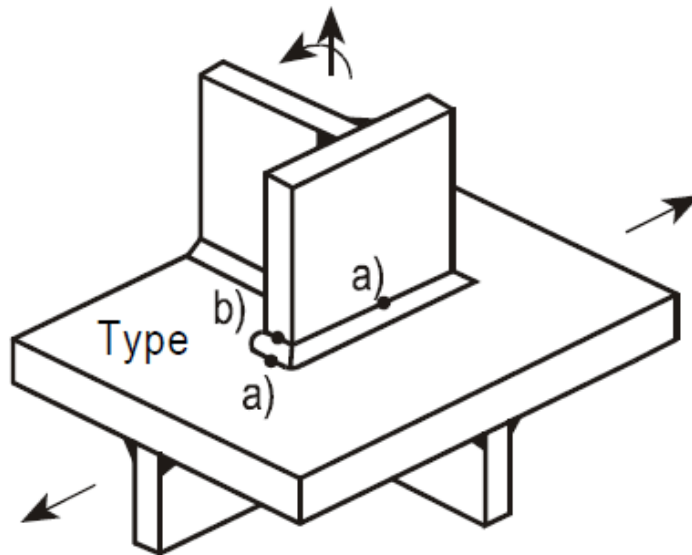


Figure 3.5: Hot spot types according to IIW standard. (Hobbacher, 2016).

The main advantage of the SHSS method is that the macro stress raising factors are captured on the load side which reduces the amount of S-N curves needed on the resistance side for evaluation of fatigue design. In IIW standard and Eurocode, there are two SHSS classes representing load-carrying and non-load-carrying fillet welds that correspond to FAT 90 and FAT 100, respectively (Hobbacher, 2016; EN:1993, 2005).

In IIW standard there are several methods mentioned for evaluating hot spot stresses for complex welded structures. Two standard procedures of calculating the structural hot spot stress at the weld toe are referred to as the "surface stress extrapolation method" (SSE) and the "through-thickness at weld toe integration method" (TTWT). Both of these methods are relatively cumbersome to use in finite element analyses since they demand a certain amount of post-processing of stresses in order to calculate the SHSS. This creates an incentive to compare these methods to other IIW-approved methods that are more easily implemented in finite element analyses like the 1mm stress method proposed by Xiao and Yamada (2004), since this would considerably reduce the post-processing effort of the analyses. The following subsection presents an introduction to these three structural hot spot stress evaluation methods and how they are implemented in the S-point model.

3.2.1 Surface Stress Extrapolation

As mentioned in Section 3.2, the surface stress extrapolation (SSE) is the standard or conventional method used in IIW (Hobbacher, 2016). SSE is based on linear or quadratic extrapolation of surface stresses at reference points at prescribed distances away from the non-linear peak stress. An illustration of the extrapolation line can be seen in Figure 3.6. The major advantage of the SSE method is that it can both be implemented in finite element analyses and also be verified in physical experiments by reading strain gauge measurements on the surface close to the weld toe. In finite element analyses, the method demands a number of criteria regarding the mesh size and shape for different types of hot spots. The S-point in corrugated web girders characterizes as *type a* hot spot according to IIW standard. The recommended evaluation method is therefore linear extrapolation using two reference points at $0.4t$ and t away from the weld toe, on a path perpendicular to the weld toe. This perpendicular path can be challenging to define when post-processing results using this method for complex geometries. Furthermore, when the correct path is found, the stresses at the correct reference points need additional post-processing. The hot spot stress is calculated using extrapolation equation 3.1 in IIW standard as presented below:

$$\sigma_{hs,SSE} = 1.67 \cdot \sigma_{0.4t} - 0.67 \cdot \sigma_{1.0t} \quad (3.1)$$

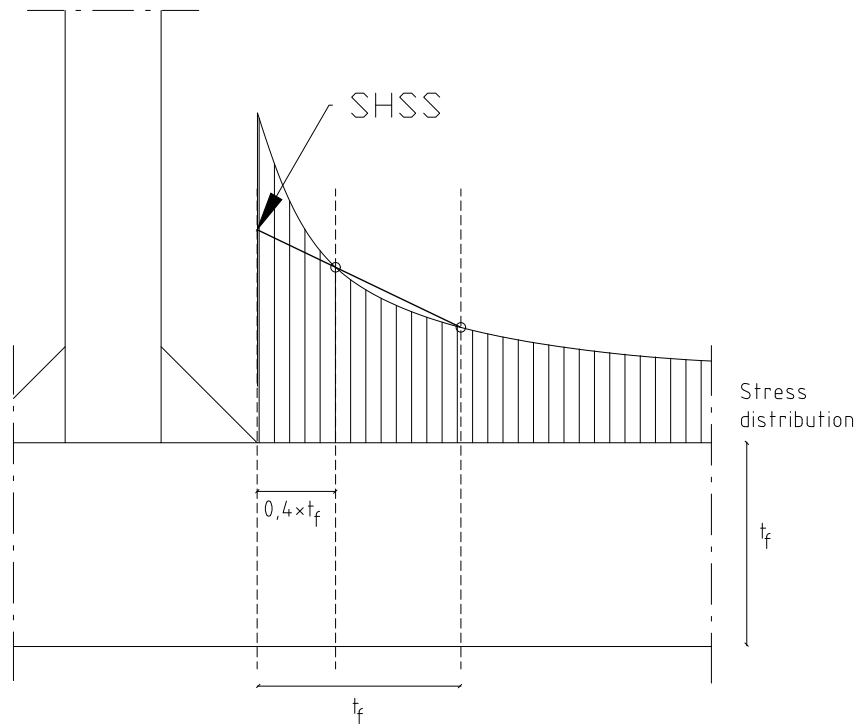


Figure 3.6: Linear surface stress extrapolation.

3.2.2 Through Thickness at Weld Toe Integration

This method is based on separating the stress profile through the thickness of the stressed plate at the weld toe into three components. The three components are the membrane stress σ_m , the bending stress σ_b and the non-linear peak stress σ_{nl} . The structural hot spot stress is then calculated by superposing σ_m and σ_b . The equations for calculating σ_m , σ_b and σ_{nl} according to IIW standard are presented below, where $\sigma(x)$ is the relevant direct stress through the thickness of the stressed plate. In finite element analyses, $\sigma(x)$ can be defined as a list of nodal stresses at the nodes through the thickness of the plate. This method is regarded to acquire accurate SHSS but with the disadvantage of requiring a higher amount of post-processing.

$$\sigma_m = \frac{1}{t} \cdot \int_{x=0}^{x=t} \sigma(x) dx \quad (3.2)$$

$$\sigma_b = \frac{6}{t^2} \cdot \int_{x=0}^{x=t} (\sigma(x) - \sigma_m) \cdot \left(\frac{t}{2} - x\right) dx \quad (3.3)$$

$$\sigma_{nl} = \sigma(x) - \sigma_m - \left(1 - \frac{2x}{t}\right) \cdot \sigma_b \quad (3.4)$$

$$\sigma_{hs,TTWT} = \sigma_m + \sigma_b \quad (3.5)$$

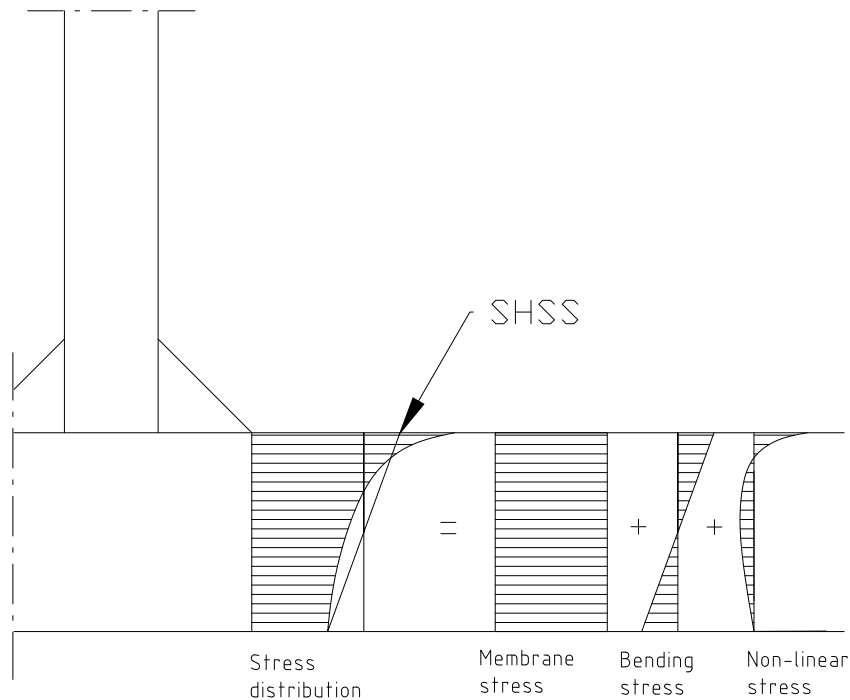


Figure 3.7: Through thickness at weld toe integration.

3.2.3 1mm stress method

In 2004, a structural hot spot stress evaluation method was developed by Zhi-Gang Xiao and Kentaro Yamada and is now accepted as an alternative method to evaluate SHSS in IIW. In this method, the SHSS for a welded detail is equal to the stress calculated 1mm below the surface, at the point where the crack is expected to initiate. This method was first validated against a reference detail, a non-load-carrying cruciform joint, where the 1mm stress was plotted against number of cycles in fatigue tests. This revealed a sufficiently narrow scatter band where the lower band of the data correlated well with fatigue class FAT 100 in IIW (Xiao and Yamada, 2004). The method has since then been validated for several welded details including load carrying welds (Doerk et al., 2003; Rong et al., 2014). Furthermore, Xiao and Yamada suggested that for 3D elements the element length in the thickness direction of the plate should not exceed 1mm, hence the name 1mm stress method (Xiao and Yamada, 2004). The main advantage of the 1mm method is that only one nodal stress is needed to calculate the SHSS which reduces post-processing effort considerably, as well as making way for easier automation of the finite element analysis and post-processing using computer scripts.

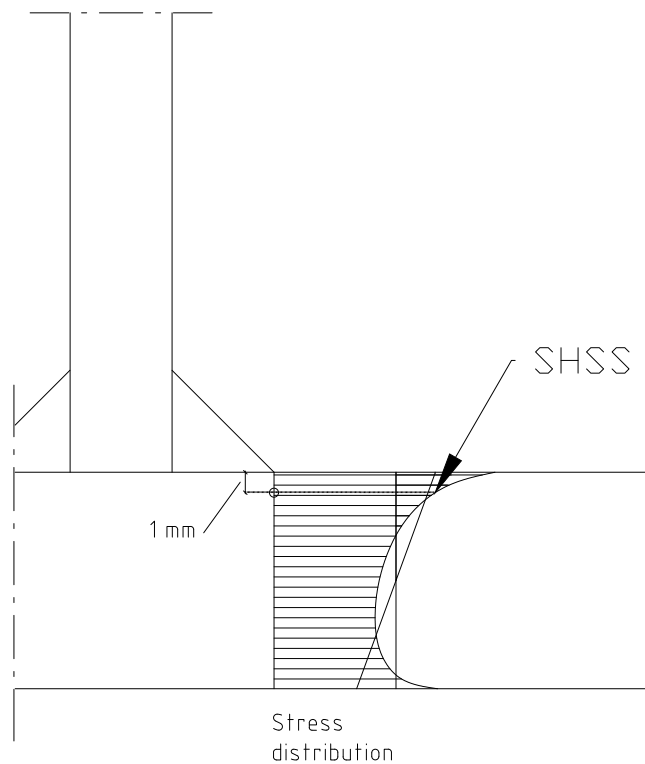


Figure 3.8: The 1mm stress at a weld toe.

3.2.4 Hot spot stress in biaxial stress state

In the case of a biaxial stress state on the surface of the stressed plate, as is the case for the girders mentioned in Section 3.1 IIW recommendations suggest using the maximum principal stress if the principal stress acts within $\pm 60^\circ$ with respect to the normal to the weld toe, and if the direction of the principal stress is not changing during loading (proportional loading) (Hobbacher, 2016). Otherwise, the stress perpendicular to the weld toe should be used to determine the structural hot spot stress, see Figure 3.9. For the girders mentioned in Section 3.1, the angle between the maximum principal stress and the normal on the weld toe is always $< 60^\circ$ and the loading is proportional, which means that the maximum principal stress at the S-point is used to calculate the hot spot stress.

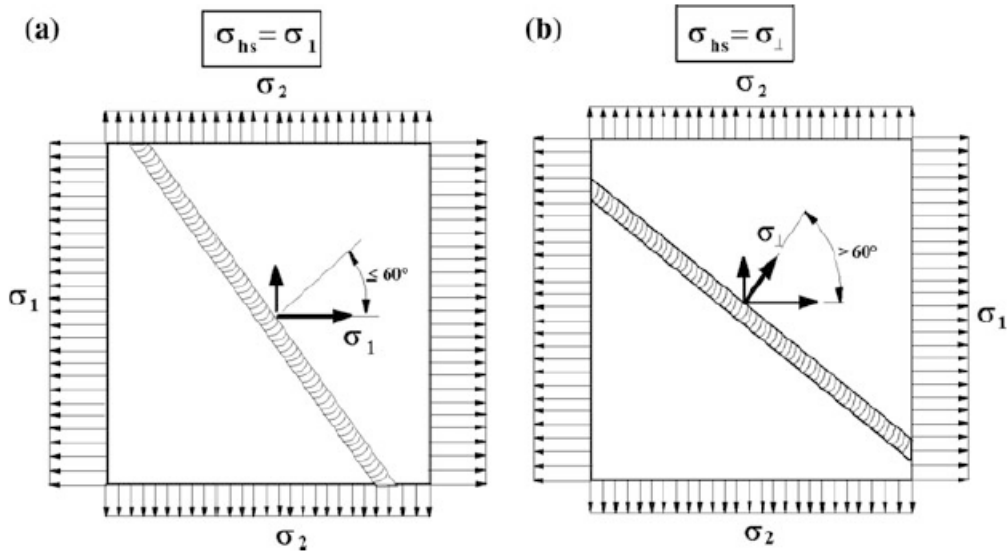


Figure 3.9: Hot spot stress at weld toe for biaxial stress state (Hobbacher, 2016).

3.3 Modelling of CWG

Since the SHSS evaluation methods demand very fine meshes in order to capture accurate results in the vicinity of stress singularities, submodeling techniques provided by ABAQUS are used to reduce the overall model size and computational time while attaining high resolution at areas of interest. Three levels of modelling are used to capture the SHSS at the S-point where the point of crack initiation is expected. The first-level model is the global model representing the full CWG. The second-level model is defined as the intermediate model and represents one corrugation wavelength. The third-level and final model is defined as the S-point model which represents the small region around the intersection of the parallel and inclined fold. Submodeling is commonly performed as "cuts" from a larger model to a smaller model representing a detail of the global model. The smaller model is consequently constructed with more detail and assigned a finer mesh which then replaces the larger model at the specific location. The common boundaries of the larger and the smaller model are referred to as the cut boundaries which are located sufficiently far from the point of interest to not be subjected to boundary distortions. All the models use the same material parameters and are calculated with linear elastic analysis since stresses with regard to fatigue are sought. Despite that linear elastic analysis and that submodeling technique is implemented, a large amount of computational capacity is yet required to acquire the large amount of results from the analyses. Therefore, the computations in this study are performed on resources at Chalmers Centre for Computational Science and Engineering (C3SE), provided by the Swedish National Infrastructure for Computing (SNIC). Furthermore, to quickly and accurately generate models and to post process the results obtained in the analyses in an efficient and structured way, python scripting is utilized. The python script used for creating the global, intermediate and S-point models is presented in Appendix A.

3.3.1 Global model

The global system is modelled as a simply supported girder, either with full length or half length by using symmetry condition at the middle of the girder, see Figure 3.10.

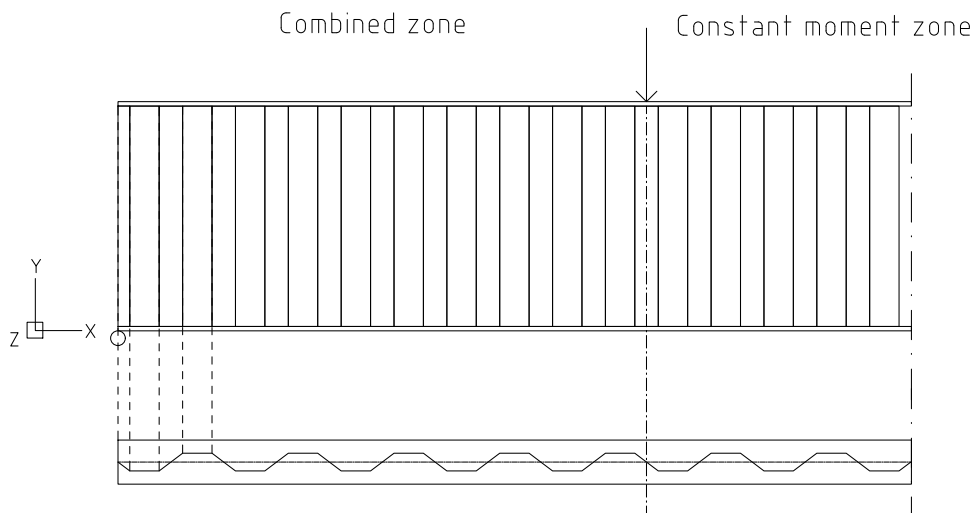


Figure 3.10: Simply supported girder, symmetry condition.

Generally, girders with symmetry condition are chosen for lower computational time. Full-length girders are however chosen in cases where two load applications in four-point bending are narrow and the constant moment zone is of interest. By using full-length girders for these cases, the associating submodels can be placed at a distance from the point loads, thus providing results more similar to the constant moment in that zone.

In addition to the boundary conditions, the ends of the girders are modelled with multi-point constraints (MPC). The I-section of the beam, highlighted in red, is connected to a master node in the middle of the bottom flange using rigid beam constraint, see Figure 3.11. The coupled constraints are assigned beam properties and the master node is in turn assigned to the support conditions. The reason for the additional constraints is to assure that the I-section at each girder end remains plane in the Y-Z plane. This type of modeling additionally conforms with the three and four-point bending experiments where transverse stiffeners usually are welded to the ends.

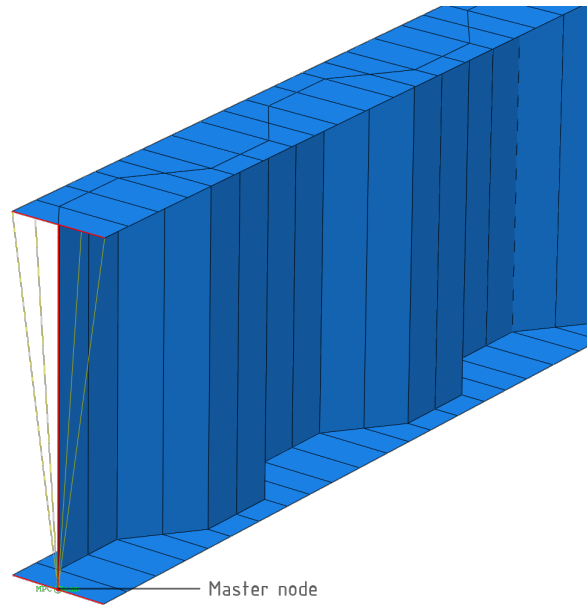


Figure 3.11: Rigid beam constraints at the I-section at the supports.

The geometric parameters that are needed to describe the global model are the length of the beam along with the I-section profile, the corrugation depth, the corrugation angle and the parallel fold length. The elements used in this model are 8-node quadratic, second-order shell elements (S8R). These elements are effective in bending dominated problems and provides reliable results for small strain problems. Furthermore, they are able to capture geometry induced stress concentrations in an accurate way (Smith, 2009). The global model and the mesh used can be seen in Figure 3.12.

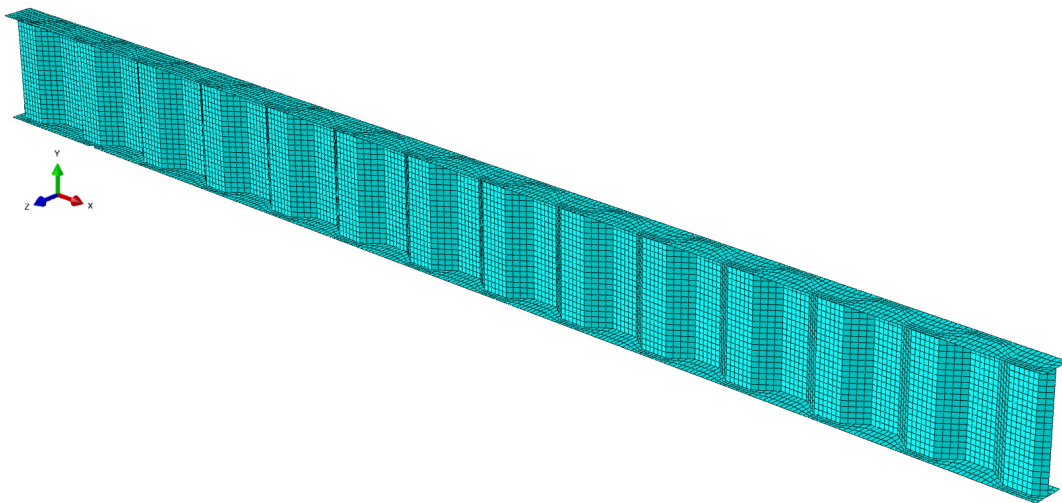


Figure 3.12: Global model's mesh.

3.3.2 Intermediate model

Since the region of stress concentration at the point of interest in the global model possesses a highly coarse mesh, it is not suitable to translate the global structural response directly to the model representing the S-point. In that case, the cut boundaries of the S-point model would be too close to the stress concentration area in the global model, which would yield inaccurate transformation of stresses to the boundaries of the S-point model. Therefore, an intermediate model is introduced to reduce the size and increase the resolution of the stress field in the vicinity of the S-point. To transfer the structural response from the global shell model to the intermediate model, shell-to-solid submodelling is used. In shell-to-solid submodelling, the submodel is made up of solid elements and replaces a region where shell elements are used in the global model. Hence, the degrees of freedom are prescribed to the surfaces of the submodel by using driving nodes meaning that displacements and rotations at the common surfaces are mapped from the global model and numerically approximated to the intermediate model. An illustration of the intermediate model connected to the global model is shown in Figure 3.13.

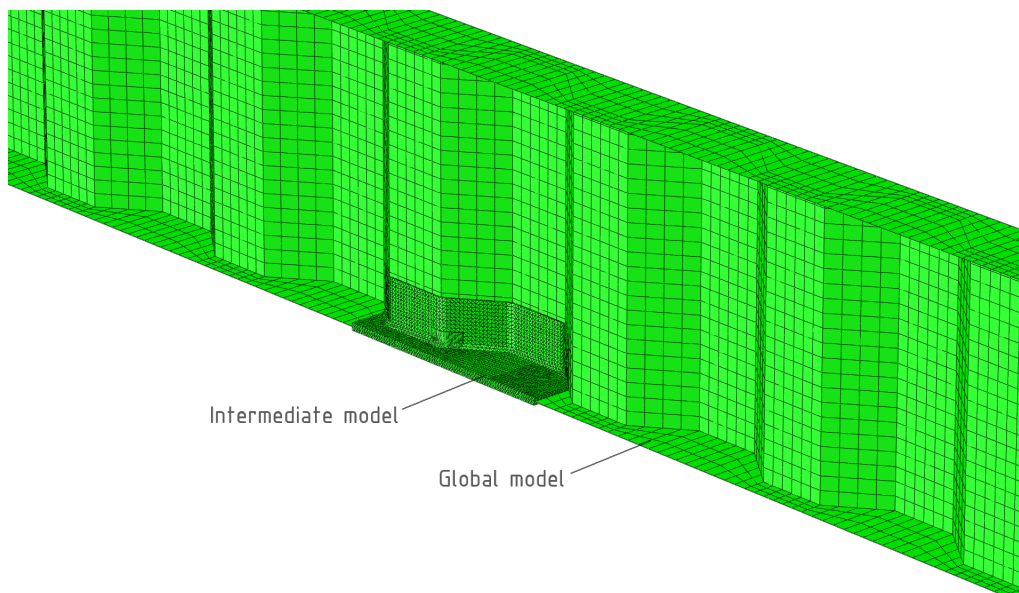


Figure 3.13: Overlay plot, shell-to-solid modeling. Global model composed of shell elements drives the intermediate model made up of solid elements.

The intermediate model is designed as a full corrugation length to have the model boundaries sufficiently far away from the S-point. The reason is again to avoid influence from the model boundaries at the smaller region of interest. The elements used in the intermediate model are ten-node quadratic tetrahedral solid 3D elements (C3D10) with the advantage of accurately performing automatic meshing along with high general-purpose properties (Smith, 2009). Furthermore, the intermediate model level is where the bend radius and weld geometry are first introduced in the finite element analysis. The intermediate model and its mesh is presented in Figure 3.14

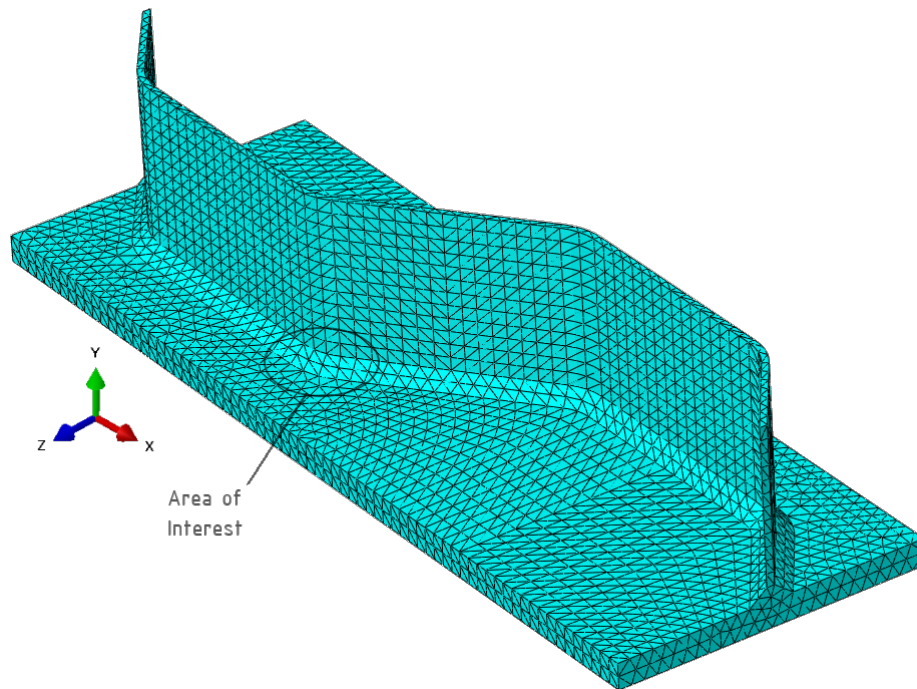


Figure 3.14: Intermediate model's mesh.

3.3.3 S-point model

Even though the intermediate model has a more refined mesh than the global model, it still does not provide desirable resolution in the stress field in the vicinity of the S-point. Therefore, a second submodel representing the S-point is created to achieve this. For the final model, solid-to-solid submodeling is used, meaning that the surface of the submodel is driven by nodes from the intermediate model, see Figure 3.15. Again, it is important to ensure that the cut boundaries for this model also are located at a sufficient distance from the stress concentration area to ensure accurate transfer of displacements, and subsequently stresses, from the cut boundaries. The dimensions of the S-point model varies depending on the flange thickness. These dimensions in x-, y- and z-direction are calculated with origin in the intersection between the longitudinal fold and the parallel fold. In x-direction, the dimensions are set to 2.5 times the flange thickness in both positive and negative direction, but not more than a quarter of a wavelength in total. In z-direction, the dimensions are set to the corrugation amplitude plus the projected length of the weld in positive direction and 2.5 times the flange thickness in the negative direction. In y-direction, the dimensions are set to $1/20$ of the web height in positive direction and the flange thickness in negative direction.

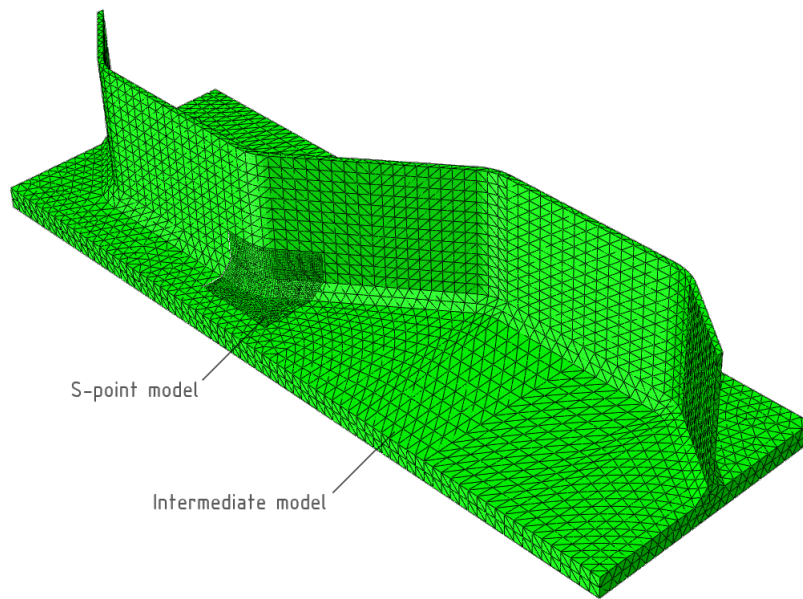


Figure 3.15: Overlay plot, solid-to-solid submodeling.

The mesh for this model is required to be highly structured to be able to use the geometric stress evaluation methods described in Section 3.2. As can be seen in Figure 3.16, the mesh is arranged to be perpendicular to the weld toe with high resolution ($\leq 1\text{mm}$) in the area of interest. By assigning this particular mesh structure, the three previously mentioned stress evaluation methods (SSE, TTWT and 1mm stress) can all be implemented for this model. The elements used are solid twenty-node quadratic hexahedral elements (C3D20R) which are high performing elements for linear elastic calculations (Smith, 2009).

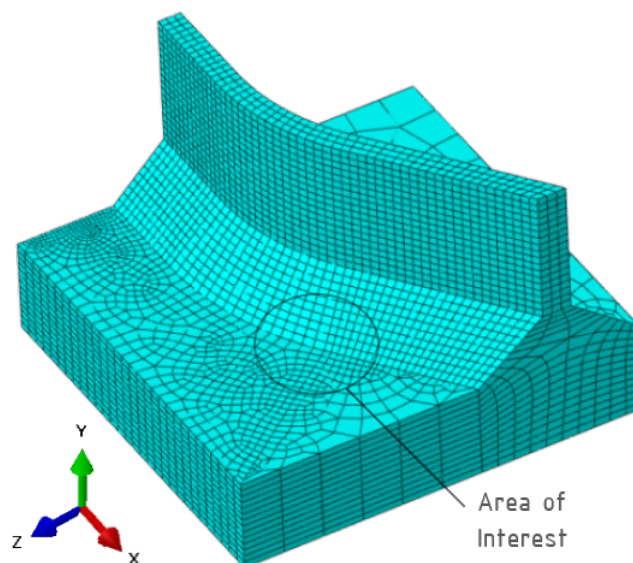


Figure 3.16: S-point model's mesh.

3.4 Verification of Model

For validation of the models, a recreation of a girder from the experiments from Ibrahim (2001) is performed. This beam is chosen since the author thoroughly documents the material parameters, geometric parameters and strain gauge locations and readings. First, it is imperative in finite element modeling to ensure that the mesh size of the model is sufficiently fine to not affect the results. A mesh convergence analysis is therefore performed on each model. For the global model, the average longitudinal stress (S11) across the top side of the bottom flange in mid-span (path MCP1), see Figure 3.17, is recorded while the mesh size is successively refined. When the error in stress between the current and previous iteration becomes less than 2% the mesh size is deemed fine enough to have a negligible effect on the results. For the intermediate model longitudinal stresses (S11) are recorded across the top side of the bottom flange in the middle of a parallel fold (path MCP2), see Figure 3.17, while the mesh is successively refined. The mesh for the intermediate model is deemed fine enough when the error of the stress between the current and previous iteration is less than 1%. For the S-point model, the mesh size is governed by the mesh size restrictions for the 1mm stress method mentioned in Section 3.2.3 and a 1mm mesh size is assumed to give convergent results. A validation of this assumption is presented in Section 4.1. A summary of the mesh convergence analysis can be seen in Table 3.3 where the mesh sizes chosen for the models are highlighted.

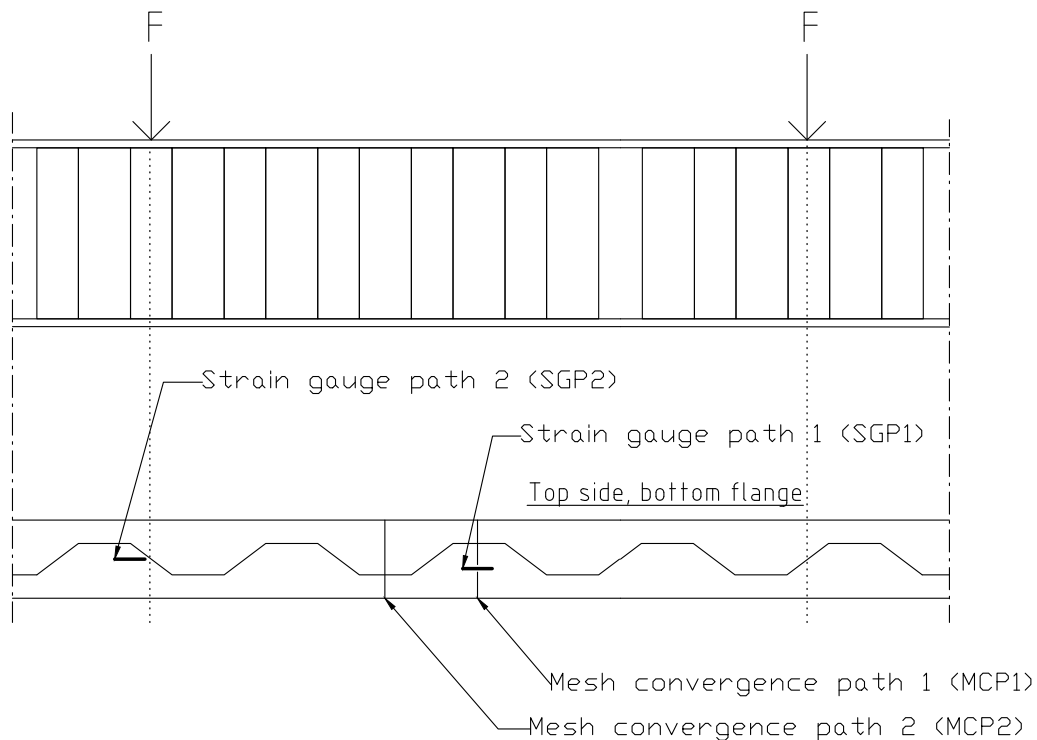


Figure 3.17: Strain gauge and convergence path locations for convergence study of FE mesh.

Table 3.3: Mesh convergence for global model.

(a) Mesh convergence for global model

Global element size	Stress at MCP1	Error [%]
$b_f/3$	171.4	-
$b_f/6$	179.4	4.4
$b_f/12$	179.7	0.3

(b) Mesh convergence for intermediate model

Global element size	Stress at MCP2	Error [%]
$b_f/6$	176.96	-
$b_f/12$	174.01	1.7
$b_f/24$	173.32	0.4

When accurate meshes are achieved, validation of the FE model against the girder for the actual experiment is performed. For the global model, this is done by comparing stresses and deflection in the FE model to stresses and deflection recorded by the strain gauges and the LVDTs in the experiments conducted by Ibrahim (2001), see Figure 3.17 for the location of the strain gauges. The intermediate model is then validated against the global model and the S-point model is validated against the intermediate model by comparing stresses at the same locations in the models. A comparison between stresses obtained in the models and stresses obtained from Ibrahim (2001) can be seen in Table 3.4. It should be noted that it is difficult to record the stresses in the models at the exact location of the strain gauges in the experiments since the coordinates of these are not given. The same situation applies when comparing stresses on paths between the models. As the mesh structure changes between the models it is difficult to ensure that the paths have the exact same coordinates. Obviously, this induces some error in the comparison between the models and the readings from the experiments, nonetheless, the errors presented in Table 3.4 are deemed acceptable as a validation of the models. Furthermore, between the global and intermediate model, a comparison of stresses at a node that is ensured to have the exact same location in both models have been made. The error between these two stresses is very small, see Table 3.4b, which again proves the validity of the models.

Table 3.4: Comparison between FE models and experimental data from Ibrahim (2001).

(a) Comparison between global FE model and experimental data

	Global FE model	Experimental (Ibrahim)	Error [%]
Deflection at mid span [mm]	15.10	14.99	0.73
Stress at SGP1 [MPa]	181.45	171	5.76
Stress at SGP2 [MPa]	174.3	173.8	0.26

(b) Comparison between global FE model and intermediate FE model

	Global FE model	Intermediate FE model	Error [%]
Stress at SGP1 [MPa]	181.45	178.47	1.6
Stress, node on tension flange at mid span[MPa]	156.61	155.98	0.4

(c) Comparison between intermediate FE model and S-point FE model

	Intermediate FE model	S-point FE model	Error [%]
Stress, on path [MPa]	183.81	186.28	1.3

4

Results

This chapter presents the results obtained from the analyses mentioned in Chapter 3. The results are further discussed in Chapter 5.

4.1 Evaluation of SHSS methods

As mentioned in Section 3.2, a comparison between three methods for calculating the structural hot spot stress at a weld toe is performed in order to determine if the more easily implemented 1mm stress method gives reliable results compared to the conventional methods, SSE and TTWT. Figure 4.1 shows the maximum principal stress contours for an S-point model located in the constant bending moment region. A finding worth noticing in this contour plot is that the maximum principal stress appears at the weld toe connected to the web in the middle of the bend radius, and not in the S-point where it is expected.

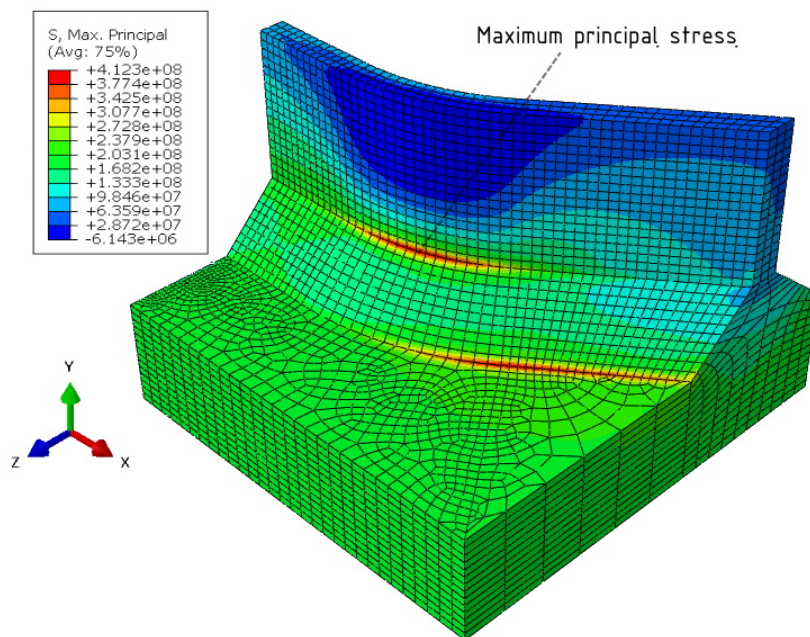


Figure 4.1: Maximum principal stress contour at S-point in constant moment zone, girder from the experiments by Ibrahim (2001).

4. Results

This finding suggests that a crack should initiate in the middle of the bend region at the weld toe connected to the web, which does not conform to previous experimental results. One explanation to why a crack is not observed at this location in the experiments could be that the low thickness of the web plate combined with the bending action subjected to the web induces a very sharp stress gradient through the thickness of the plate, see Figure 4.2. In this case, an initial micro-crack would grow out of the highly stressed region at an early stage which would stop the crack propagation. It could also be a fabrication of the FE model since the stress decreases dramatically over the distance of one element thickness, which makes this a highly localized "stress singularity" and the SHSS evaluation methods might have difficulties capturing this case.

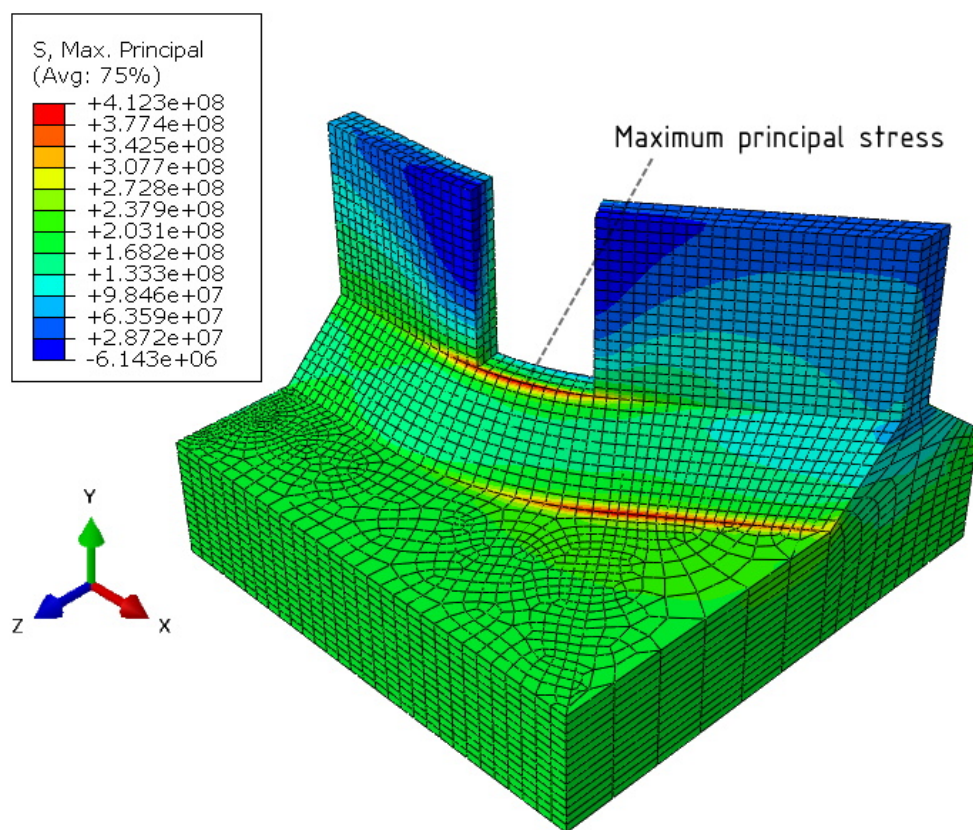


Figure 4.2: Stress contour through web thickness, girder from experiments of Ibrahim (2001).

With this as background along with the fact that cracks have not been observed at this location in the experimental tests, this hot spot is excluded from further investigation. The exclusion of this hot spot can also be motivated with the fact that the main aim of this thesis based on the analyses mentioned in Chapter 3 is to investigate the influence of transverse bending of the *flanges* on the SHSS at the S-points along the girder.

When the weld toe connected to the web is excluded from the contour plot, see Figure 4.3, the maximum principal stress appears at the S-point as expected. The 1mm stress, SSE stress and TTWT stress for girders by Abbas (2003) and Ibrahim

(2001) are plotted in Figure 4.4 for an S-point located in the constant bending moment region. For the girder by Ibrahim (2001), two mesh sizes were analyzed in order to investigate the mesh sensitivity of the SHSS methods.

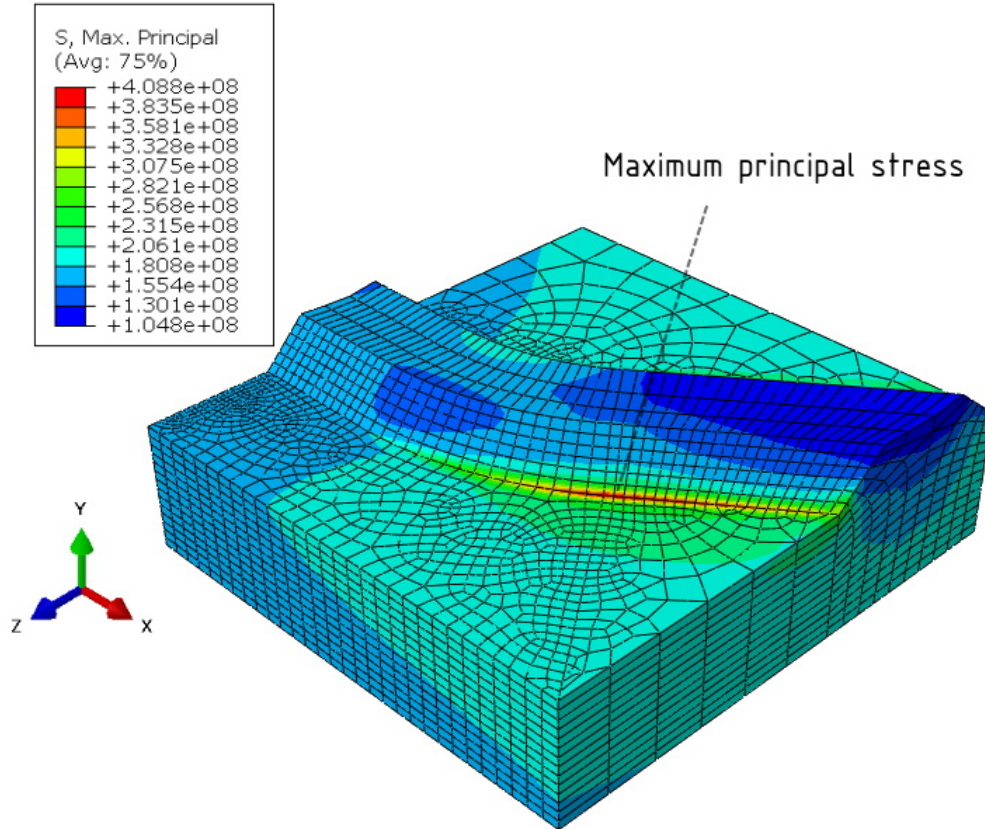


Figure 4.3: Maximum principal stress contour at S-point when web is neglected, girder from the experiments by Ibrahim (2001).

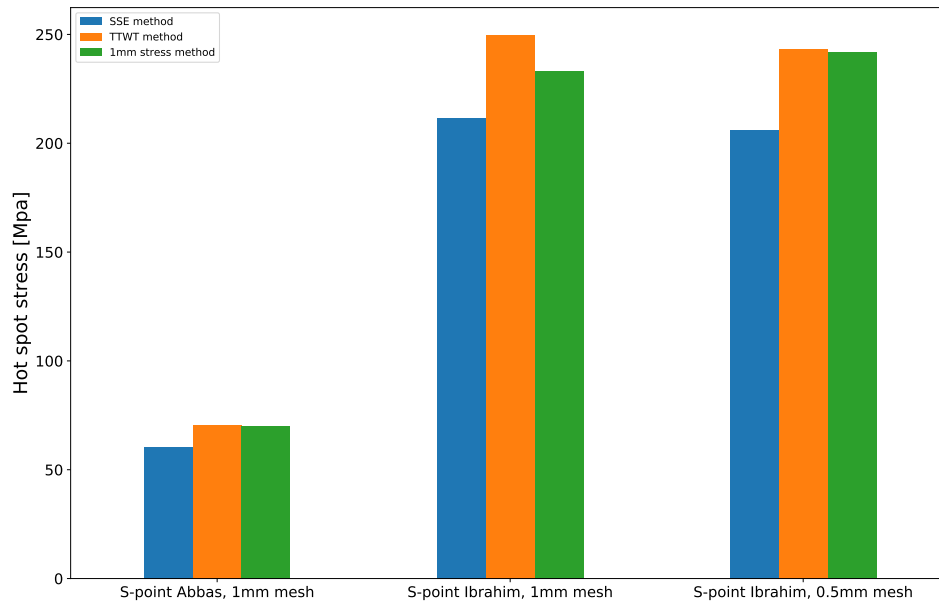


Figure 4.4: Comparison between structural hot spot stress methods.

Between the three methods, the 1mm stress method seems to be the most mesh sensitive. Although it should be noted that the difference for the 1mm stress between 1mm mesh and 0.5mm mesh is $< 4\%$, which can be deemed negligible. For further analysis of the test girders, this finding serves as validation for using 1mm thick elements when applying 1mm stress method to calculate the SHSS. Comparing the three methods, it can be seen that 1mm stress and TTWT correlate the most and result in higher structural hot spot stresses compared to SSE, which in case of fatigue life assessment provides hot spot stresses that are more conservative. With this as background along with the fact that the TTWT method is a conventional method for calculation of SHSS according to IIW (Hobbacher, 2016), the 1mm stress method is deemed to provide results that are reliable enough to use for further analyses of the girders.

4.2 Stress state in bottom flange

In order to validate the assumptions made in Section 3.1 regarding the choice of parameters that govern the magnitude of transverse bending of the flanges, a number of graphs are produced. Figure 4.6 shows the transverse deflection along the south edge (see Figure 4.5) of the bottom flange for all girders.

As predicted in Section 3.1, girder 2 experiences the largest transverse deflection while girder 3 experiences the smallest deflection, which in turn would lead to the largest and smallest transverse bending stresses, respectively. It should be noted that the transverse deflection in this case is both governed by the transverse bending

moment and the slenderness of the web. Meaning that for the deeper girders, girder 3 and 4, the flanges will be able to deflect more since the stiffness of the web in the transverse direction is lower. This higher deflection does not necessarily mean that the transverse bending stress is higher, which will be seen later in Section 4.2.2. What becomes evident from Figure 4.6 is that the transverse bending of the flanges can be described by a global and local bending action where the local action is attributed to the "waviness" of the curves.

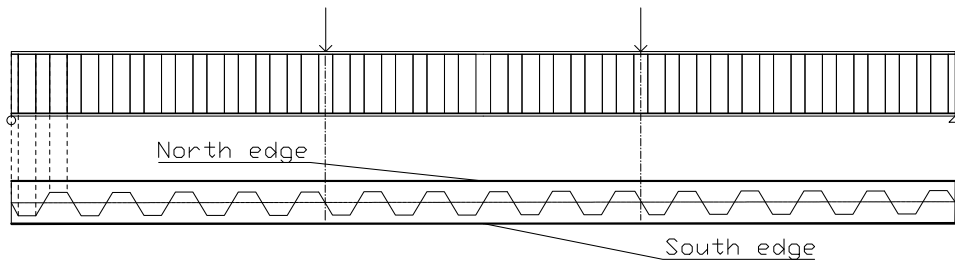


Figure 4.5: Definition of "North" and "south" edges along the bottom flange.

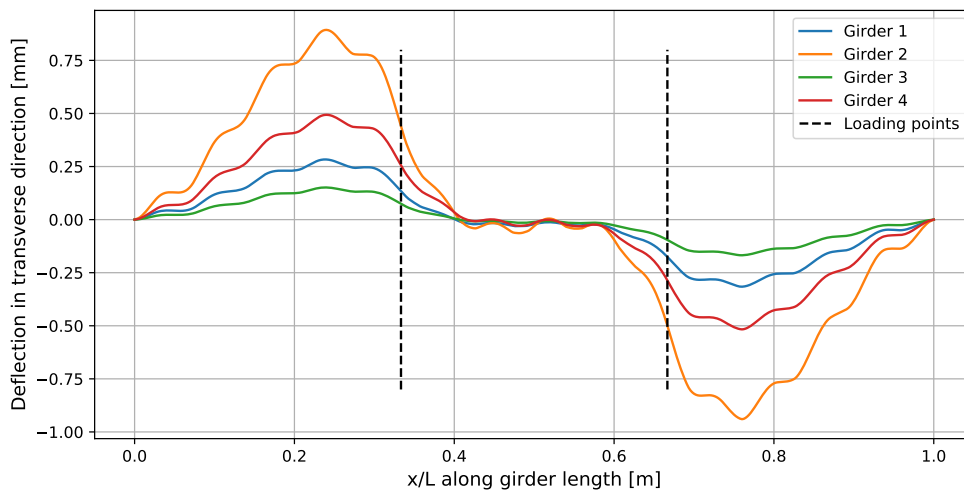
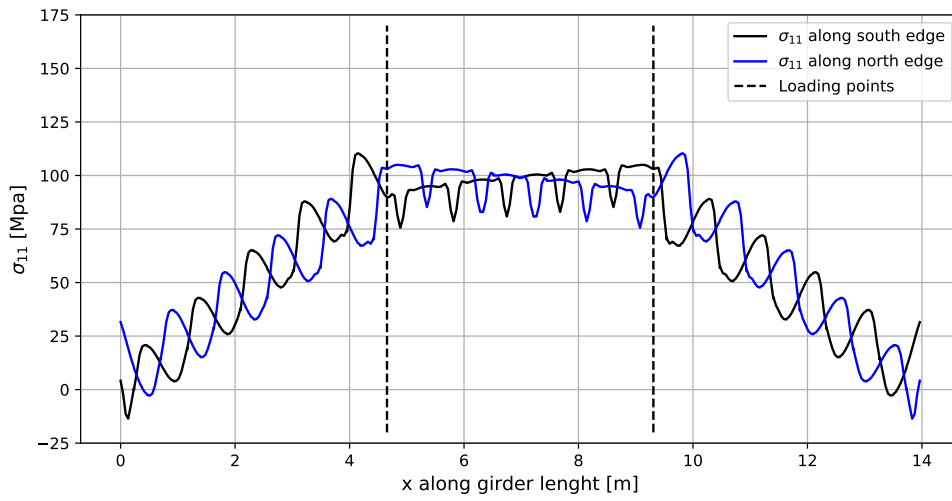


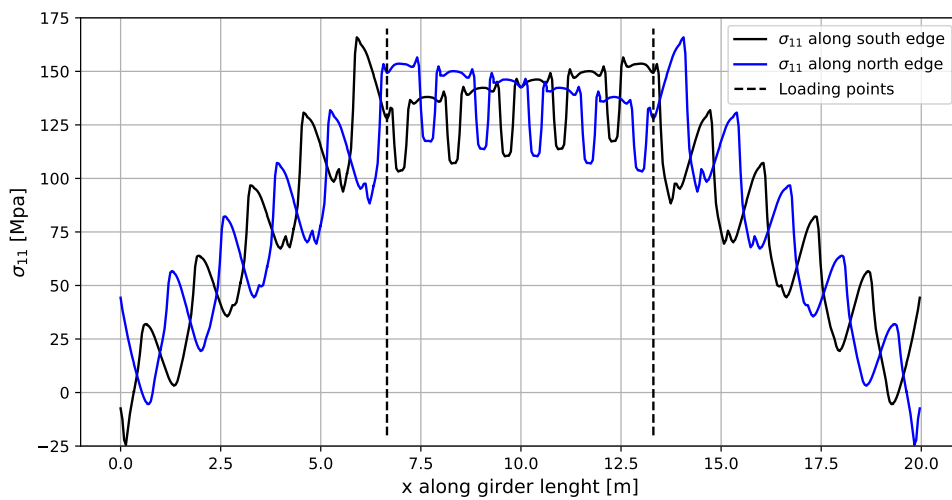
Figure 4.6: Transverse deflection of bottom flanges for all test girders.

Figures 4.7 and 4.8 show the longitudinal stresses (S_{11}) along the north and south edges of the bottom flanges of the girders. The oscillation of the curves is again attributed to the local transverse bending of the flange. The global transverse bending action is less evident in these graphs but is presented later in this section. Worth noting in figures 4.7 and 4.8 is that the maximum stress is constantly located in the combined shear and moment regions, although for girder 3 (Figure 4.8a), the maximum stress in the constant moment region is close to that of the combined region.

4. Results



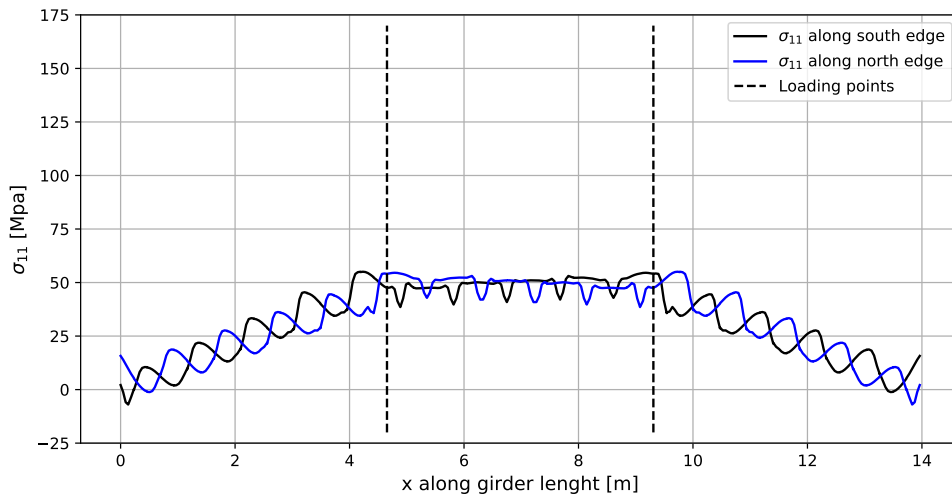
(a) Girder 1



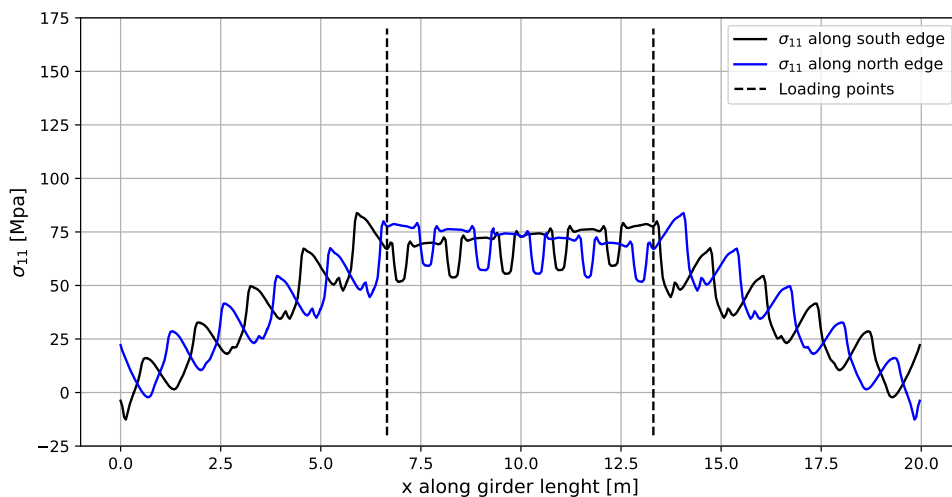
(b) Girder 2

Figure 4.7: Longitudinal stresses (S_{11}) along north and south edge of bottom flange for girders 1 and 2.

By extension this means that a crack should be expected in the combined region for all four test girders, considering that the principal stress at the S-points on the girders has more or less the same direction as the longitudinal stress at these locations. In case of girder 3, this expectation might not hold true since the maximum stress in the constant moment region is very close to that of the combined region. Referring back to the literature study in Chapter 2, this could be an explanation to why some girders in the experiments fail in the constant moment region and others in the combined region, meaning that girders that are subjected to a high amount of transverse bending might be more prone to failure in the combined region.



(a) Girder 3



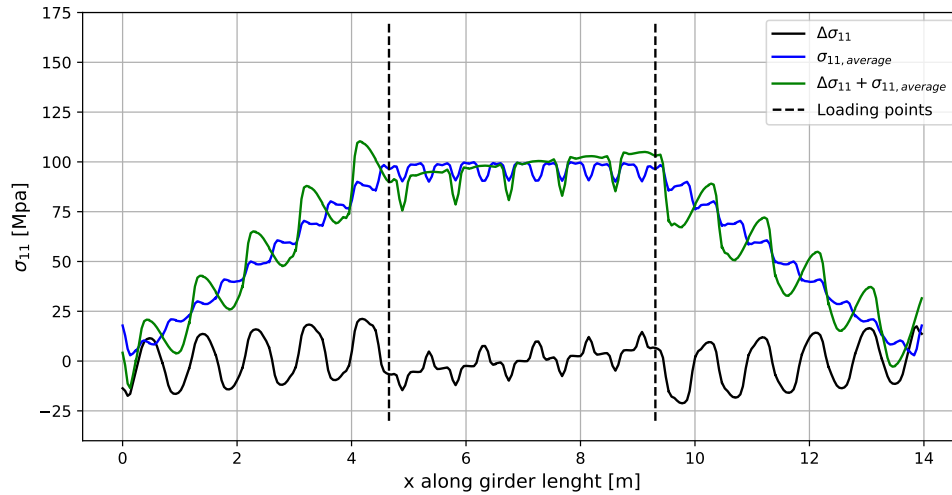
(b) Girder 4

Figure 4.8: Longitudinal stresses (S_{11}) along north and south edge of bottom flange for girders 3 and 4.

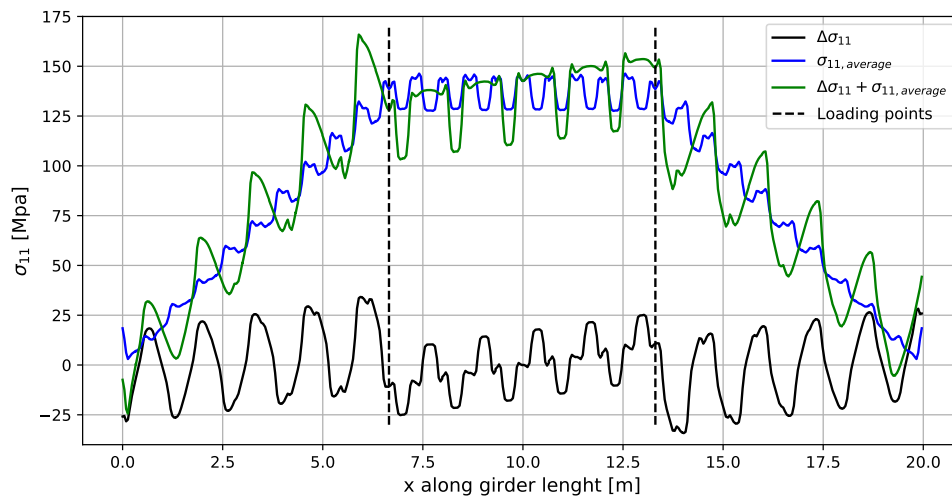
In figures 4.9 and 4.10 three curves can be seen. The blue curves represent the average longitudinal stress between the north and south edges of the bottom flange. This curve is assumed to represent the *primary bending stress* along the girder and the oscillation of the curve owes to the difference between contribution to flexure from the web between a parallel section and an inclined section, as described in 2.4. The black curve represents the difference between average longitudinal stress in the flange and longitudinal stress along the south edge of the girders. This curve is assumed to represent the *transverse bending stresses* along the bottom flange. Referring back to earlier in this section, the linear slopes of these curves is attributed to the global transverse bending action and the oscillation to the local

4. Results

bending action. Validation of the distribution of these curves can be seen when reviewing earlier work on the flexure behaviour of CWGs by Abbas (2003).



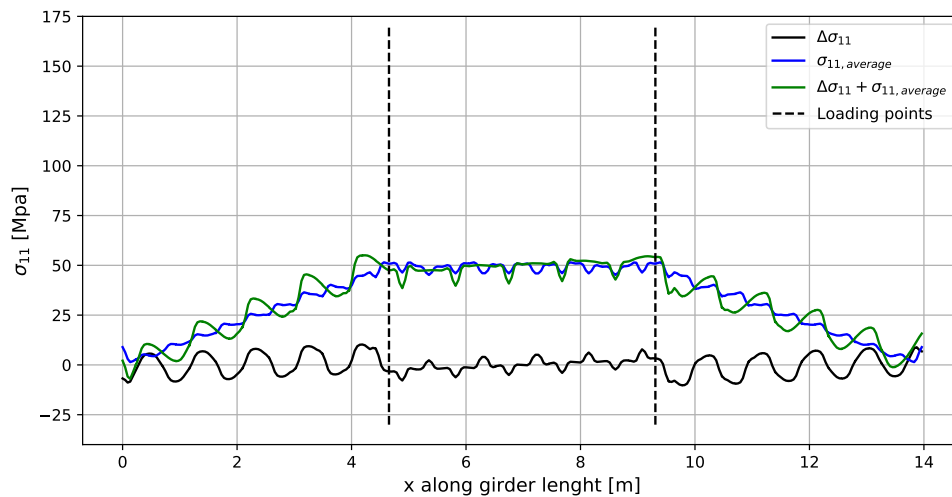
(a) Girder 1



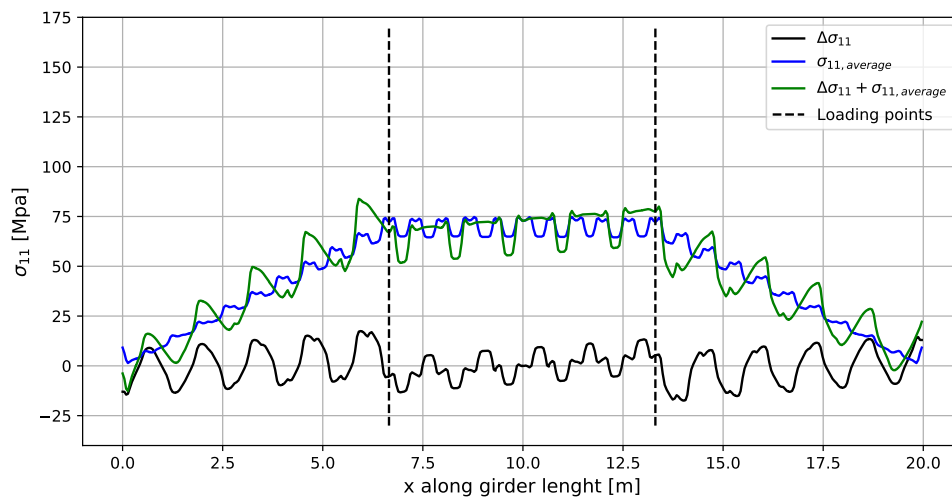
(b) Girder 2

Figure 4.9: Average and delta stresses for girders 1 and 2.

The green curve represents the superposition of the black and blue curves. Note that this curve produces the exact same stress curve seen in figures 4.7 and 4.8, supporting that the longitudinal stress from primary bending and the transverse bending stress indeed can be calculated as the average between the edge stresses and the difference between the edge stresses and the average stresses, respectively.



(a) Girder 3



(b) Girder 4

Figure 4.10: Average and delta stresses for girders 3 and 4.

4.2.1 Comparison between average longitudinal stress and bending stress from beam theory

To further investigate the longitudinal stress distribution in the flanges, the graphs in figures 4.13 and 4.14 are produced. In these figures, the longitudinal stress is plotted across the flange width in five sections for one wavelength(3) in the combined shear and moment region and one wavelength(8) in the constant moment region. This is done for girders 2 and 3 and the location of the sections can be seen in Figure 4.11.

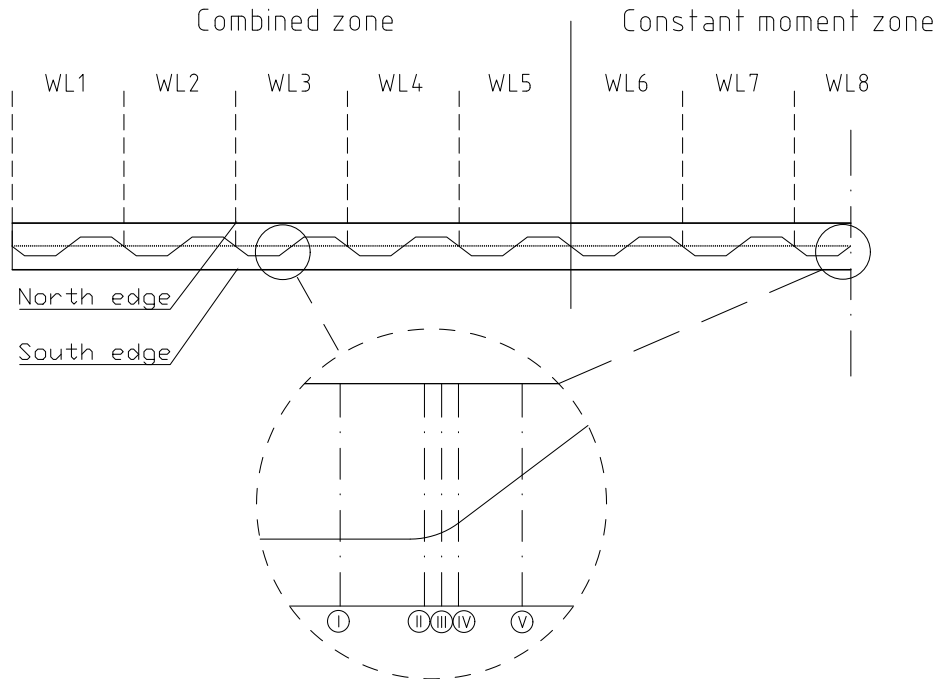


Figure 4.11: Longitudinal stress sections girders 2 and 3.

The graphs show approximately a linear trend between the flange edges, which is also supported by previous work by Kövesdi and Dunai (2014). Local reduction in stresses appears where the web intersects the flange, which is reasonable. Since the total longitudinal stress can be expressed as a superposition of primary and transverse bending stresses (Abbas, 2003), and assuming that the transverse bending stresses follow a "generic" bending stress distribution as illustrated in Figure 4.12, the stress distribution in the sections can be approximated by the dotted lines in figures 4.13 and 4.14.

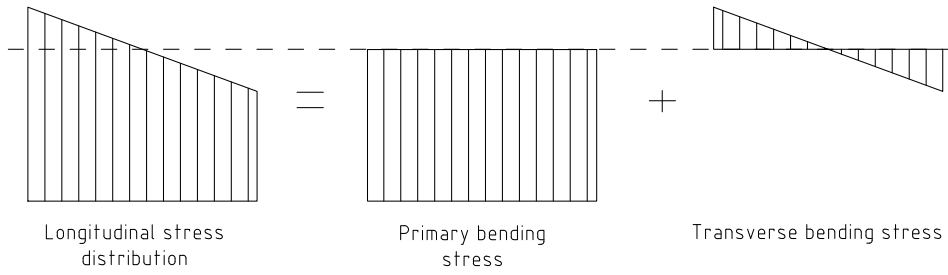
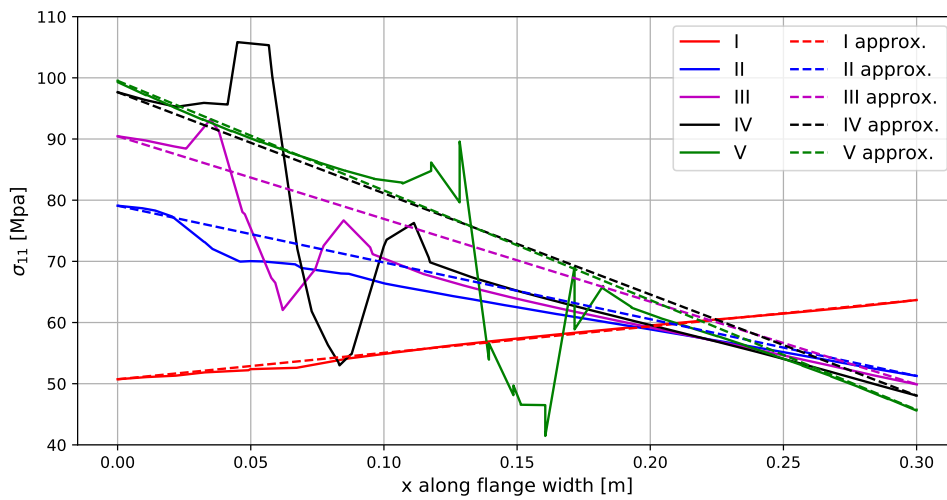
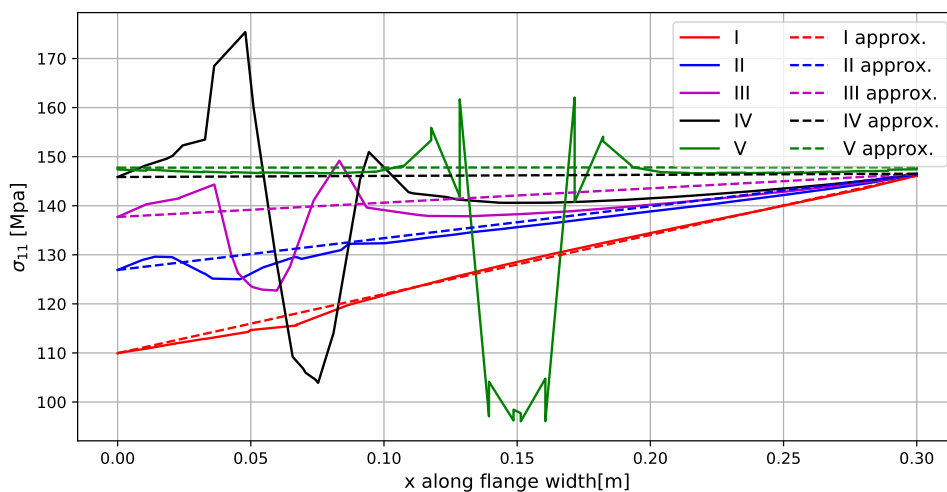


Figure 4.12: Superposition of primary and transverse bending stresses.



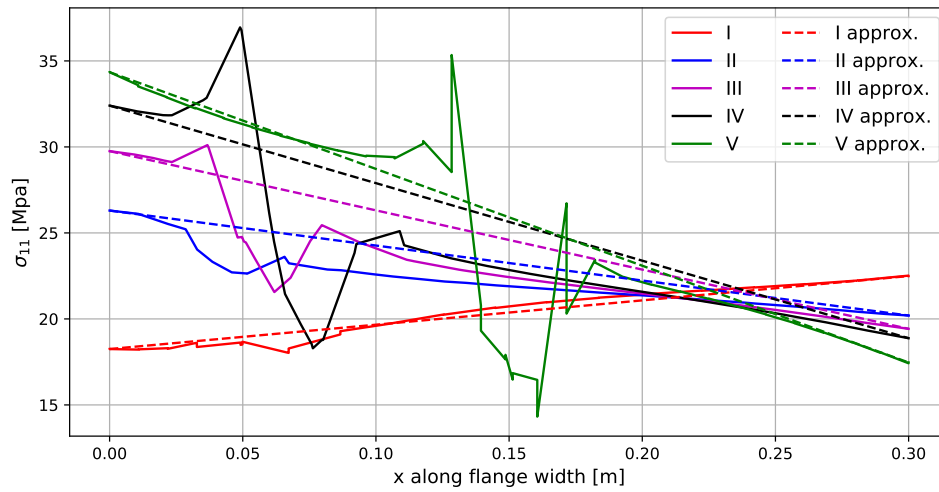
(a) Wavelength 3



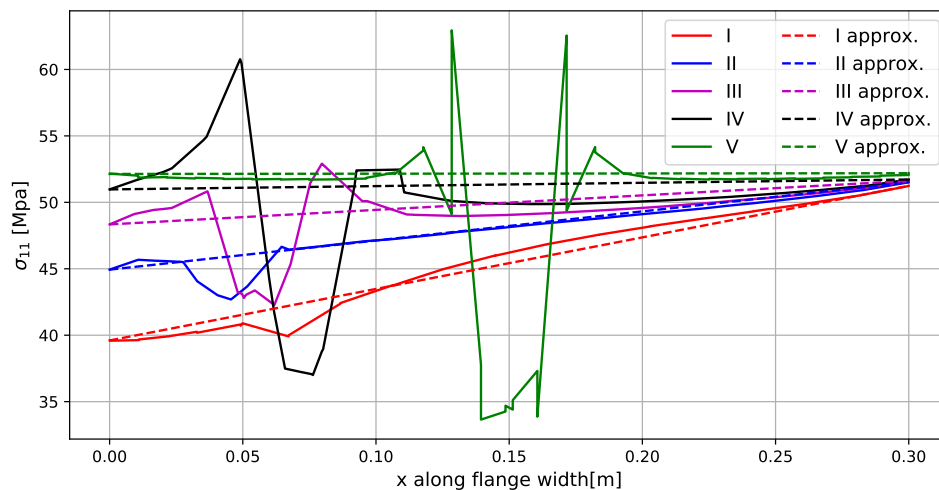
(b) Wavelength 8

Figure 4.13: Longitudinal stress profiles across the flange width in various sections for girder 2.

4. Results



(a) Wavelength 3



(b) Wavelength 8

Figure 4.14: Longitudinal stress profiles across the flange width in various sections for girder 3.

Following the reasoning of the superpositioned stress distribution in previous Figure 4.12, the primary bending stresses in the sections should be equal to the stress at the centerline of the flange on the approximated dotted curves. This assumption is checked by calculating the bending stresses in the sections with simple bending theory, using Navier's formula (see equation 4.1), and comparing them to the values obtained from the approximated curves. Note that when calculating the second moment of inertia for the girders, the "accordion effect" mentioned in Section 2.4 is taken into account, thus neglecting the bending capacity of the webs. The comparison and the errors between the calculations can be seen in Table 4.1, which indicates that this approximation is fairly accurate. Note that the largest error appears in

section I in all cases. This section is located in the middle of a parallel fold and the large error can repeatedly be attributed to the contribution to flexure capacity from the web, which is neglected according to the "accordion effect". Note also the slope difference between wavelength 3 and 8 for section V in all cases. Section V is located in the middle of an inclined fold where the transverse bending moment should be the largest. At wavelength 8 the slope of the line in section V is approximately zero, indicating that the transverse bending stresses are close to zero in this section, which is expected. At wavelength 3 the slope of the line a section V is the largest, which is also expected.

$$\sigma_p = \frac{N}{A} + \frac{M}{I_y}z \quad (4.1)$$

Where:

N	Axial force action on the cross section
A	Area of the cross section
M	Bending moment action on the cross section
I_y	Second moment of inertia for the cross section
z	Distance from center of gravity of the cross section to the point of interest

Section	Beam theory [MPa]	Approximated [MPa]	Error [%]
I	63.95	57.20	11.8
II	68.22	65.18	4.7
III	67.58	70.17	3.7
IV	68.86	72.85	5.5
V	71.05	72.63	2.2

(a) Girder 2, wavelength 3

Section	Beam theory [MPa]	Approximated [MPa]	Error [%]
I	142.11	128.02	11.0
II	142.11	136.63	4.0
III	142.11	142.09	0.01
IV	142.11	146.19	2.8
V	142.11	147.79	3.8

(b) Girder 2, wavelength 8

Section	Beam theory [MPa]	Approximated [MPa]	Error [%]
I	22.81	20.37	12.0
II	23.90	23.25	2.8
III	23.57	24.59	4.1
IV	24.23	25.64	5.5
V	25.35	25.91	2.2

(c) Girder 3, wavelength 3

Section	Beam theory [MPa]	Approximated [MPa]	Error [%]
I	50.69	45.42	11.6
II	50.69	48.22	5.1
III	50.69	49.98	1.4
IV	50.69	51.35	1.3
V	50.69	52.16	2.8

(d) Girder 3, wavelength 8

Table 4.1: Comparison between primary bending stress from beam theory and approximated primary bending stress.

For further analysis, the longitudinal stresses along the bottom flanges of the girders are separated into stresses coming from primary bending and stresses coming from transverse bending. Stresses from primary bending are calculated as the mean value between the north and south edges of the girders and the transverse bending stresses are calculated as the difference between the edge stress on the flange and the primary bending stress.

For further analysis, section III is selected when calculating longitudinal stresses from primary bending. This is motivated by that from a design perspective the corrugation geometry of a CWG is often described without the bend radius, hence the coordinates for that point analytically are easy to determine. Additionally, the difference in primary bending stress between this section and the exact section of the S-point (section IV) is negligible.

4.2.2 Stress state at S-points

The S-points where the influence of transverse bending of the bottom flange is evaluated are presented in Figure 4.15. Since the girders and loading scheme are symmetric, only half of the girders are plotted and analyzed.

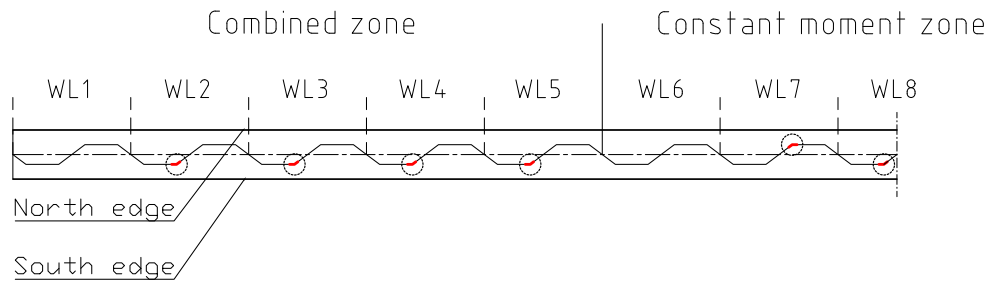


Figure 4.15: Studied S-points along the girders.

Figure 4.16 shows the variation of longitudinal stress coming from primary bending at S-points along the girders. As expected, the distribution follows the moment distribution of a four-point loading scheme presented in Figure 3.1.

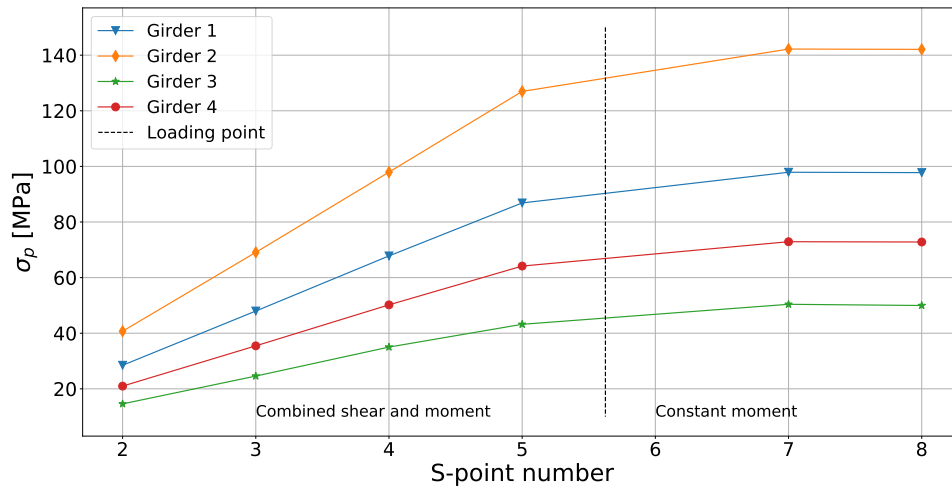


Figure 4.16: Variation of longitudinal stress from primary bending at S-points along the girders.

The variation in transverse bending stresses at the S-points can be seen in Figure 4.17. The transverse bending stresses are calculated both as mentioned in Section 4.2.1 (solid lines) and by equation 2.4 (dotted lines). Repeatedly, it becomes evident that the assumptions made in Section 3.1 regarding which girder experiences the largest and smallest amount of transverse bending seems to hold true. Referring back to Section 4.2 it becomes evident that girder 2 experiences a greater amount of transverse bending than girder 4, even though Figure 4.6 shows larger transverse deflections for girder 4. Furthermore, this graph shows that equation 2.4 overestimates the transverse bending acting on the flange and is not able to capture the variation in transverse bending stress coming from the global transverse deflection seen in Figure 4.6. This will be discussed later on in Chapter 5. The transverse bending stresses used for further analysis are those calculated as mentioned in Section 4.2.1 (solid lines in Figure 4.17).

4. Results

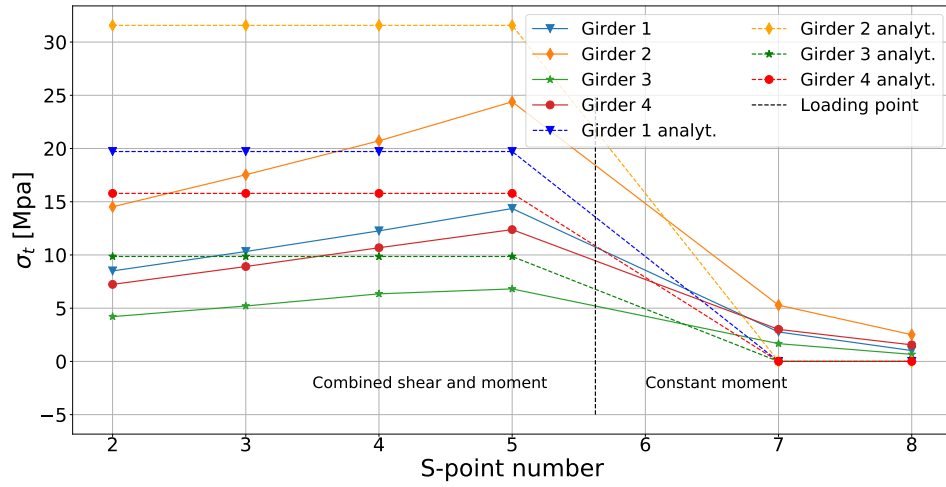


Figure 4.17: Variation of transverse bending stresses at S -points along the girders.

The structural hot spot stress is calculated using the 1mm stress method mentioned in Section 3.2 at the S -points along the girder. Figure 4.18 shows the variation of SHSS at the S -points. As expected, the structural hot spot stress increases as the primary bending stresses increase. Important to note in this graph is that the largest SHSS appears in S -point 5 which is located in the combined shear and moment region, i.e not where the primary bending stress is the largest. An exception can be seen for girder 3 where the largest SHSS appears in S -point 7 located in the constant moment region. This indicates that girders with a low contribution of transverse bending could be more prone to fail in a region where primary bending is the highest.

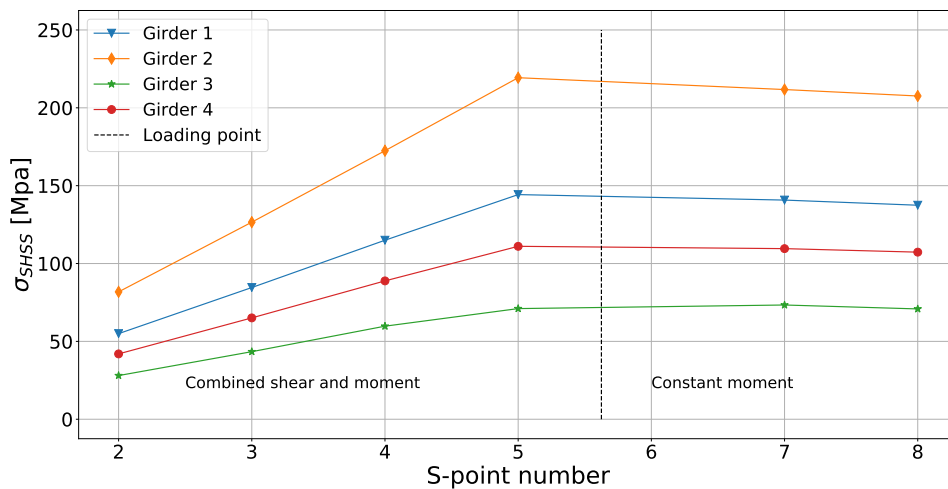


Figure 4.18: Variation of structural hot spot stress at S -points along the girders.

Figure 4.19 shows SHSS normalized by the primary bending stress at S-points along the girders. From this plot, it becomes evident that the SHSS to primary bending stress ratio increases when moving from the constant moment region to the combined shear and moment region. This indicates that the transverse bending stresses introduced in the combined region in fact have an effect on the structural hot spot stress at the S-points. The exponential trend of this curve towards the support is probably due to that the primary bending stresses approach zero towards the support. It is therefore the increase that happens between the 7th and 5th S-point that is of interest in this graph since it is this increase that indicates the difference between the combined shear and moment region and the constant moment region.

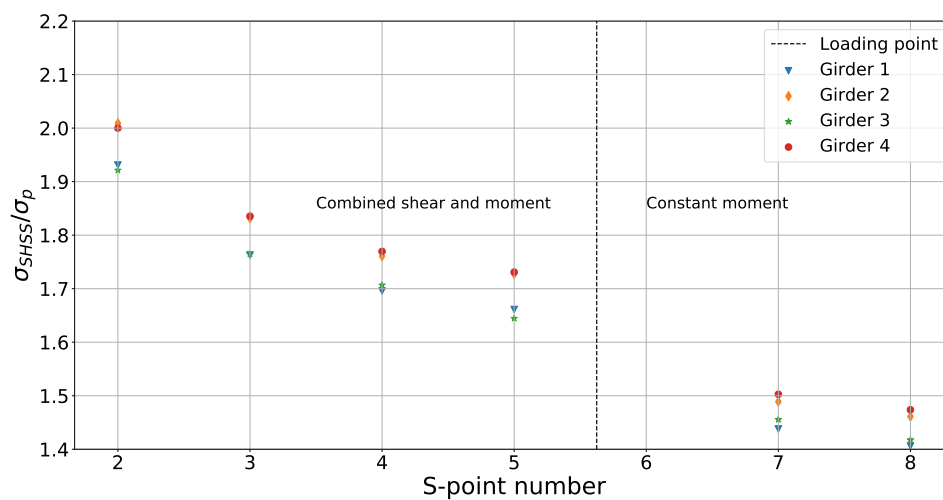


Figure 4.19: SHSS normalized by primary bending stress at S-points.

Figure 4.20 shows transverse bending stress plotted against SHSS, both normalized by primary bending stress at the S-points. Here, a separation between the two groups can be distinguished. The shorter girders with short parallel folds (girders 1 and 3) and the longer girders with long parallel folds (girders 2 and 4) seem to follow each other, respectively.

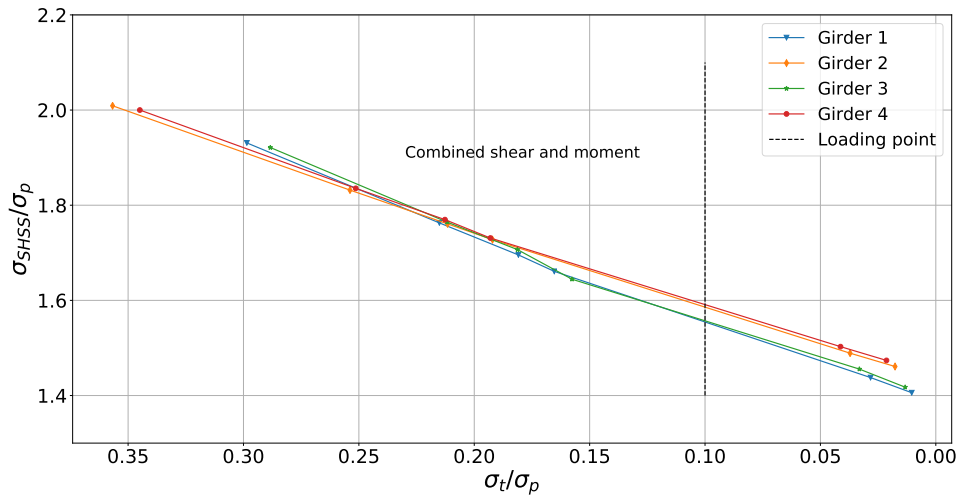


Figure 4.20: Relation between transverse bending stress normalized by primary bending stress and SHSS normalized by primary bending stress at S-points.

Following the logic for superposition of primary and transverse bending stresses, a proposal that the structural hot spot stress at an S-point can be described by a linear combination of those two is presented in Equation 4.2:

$$\sigma_{SHSS} = \sigma_p \cdot SCF_p + \sigma_t \cdot SCF_t \quad (4.2)$$

Where:

- σ_{SHSS} Structural hot spot stress
- σ_p Primary bending stress
- SCF_p Stress concentration factor for primary bending stress
- σ_t Transverse bending stress
- SCF_t Stress concentration factor for transverse bending stress

Rewriting this formula, the equation for a linear relation can be achieved as follows.

$$\frac{\sigma_{SHSS}}{\sigma_p} = SCF_p + \frac{\sigma_t}{\sigma_p} \cdot SCF_t \quad (4.3)$$

Studying equation 4.3 it can be seen that the two fractions correspond to the x- and y-axis in Figure 4.20. In this case, the stress concentration factor for transverse bending stresses corresponds to the slope of the curves and the stress concentration factor for primary bending stresses corresponds to the y-intercept, i.e. where σ_t/σ_p is zero. It can be seen in Figure 4.20 that girders 1 and 3 and girders 2 and 4 belong to approximately the same linear relation, respectively.

With this in mind, one set of SCF_p and SCF_t in Equation 4.2 should be able to predict SHSS for girders 1 and 3 while another set of SCF_p and SCF_t should be able to predict it for girders 2 and 4. Therefore, mean values for SCF_p and SCF_t between girders 1 and 3 and girders 2 and 4, respectively, are sought.

As can be seen in Figure 4.20 the curves do not reach zero for σ_t/σ_p at S-point number 8 in the middle of the constant moment region, meaning that the transverse bending stress does not reach zero at this point which is expected analytically. Therefore, the stress concentration factor for primary bending is calculated from the pure bending and uniform tension models described in Section 3.1 in order to establish more precise values for SCF_p . The stress concentration factor for primary bending is in this case calculated as SHSS at an S-point divided by the primary bending stress. As can be seen in Table 4.2a girders 1 and 3 and girders 2 and 4 correlate well, which conforms with earlier trends. Note that if extrapolating the lines in Figure 4.20 to $\sigma_t/\sigma_p = 0$ approximately the same values for SCF_p found for the pure bending model in Table 4.2a would be obtained. With this in mind, the values for SCF_p obtained from the pure bending model are used for further analysis. This result also proves that the uniform tension model is not able to capture this effect as precisely as the pure bending model. The mean value for SCF_p between girders 1 and 3 and girders 2 and 4 can be seen in Table 4.2b.

Table 4.2: Stress concentration factor for primary bending stress from pure bending and uniform tension models.

(a) SCF_p for the girders

Girder	SCF_p pure bending model	SCF_p uniform tension model
Girder 1	1.394	1.304
Girder 2	1.445	1.343
Girder 3	1.402	1.314
Girder 4	1.457	1.352

(b) Mean SCF_p for the girders

Girders	Mean SCF_p pure bending model	Mean SCF_p uniform tension model
Girders 1 and 3	1.40	1.31
Girders 2 and 4	1.45	1.35

Figure 4.21 shows the variation of stress concentration factor for transverse bending stresses, calculated by rearranging equation 4.2. For design purposes, the stress concentration for transverse bending stresses is assumed to be equal to 1 in the constant moment region since theoretically there is no transverse bending moment from shear flow in this region. As can be seen in this figure, SCF_t is not exactly constant in the combined shear and moment region which is not supported by Equation 4.2 and Figure 4.20. This could be explained by that the values close to discontinuity

4. Results

regions (support location and load application points) get distorted. In this case, if the number of wavelengths would have been greater in the combined shear and moment region, a more constant trend could have been seen for S-points far from the discontinuity regions. Thus, the trend seen for the combined region in Figure 4.21 would show a more "S-shaped" trend. With this as background, the values for SCF_t at S-points 2 and 5 are excluded from further analysis. SCF_t is then calculated as the mean value between SCF_t at S-points 3 and 4 for girders 1 and 3 and for girders 2 and 4, respectively. The values for SCF_p and SCF_t for the girders are summarized in Table 4.3.

Table 4.3: SCF_p and SCF_t for the 4 studied girders.

	SCF_p	SCF_t
Girders 1 and 3	1.40	1.68
Girders 2 and 4	1.45	1.50

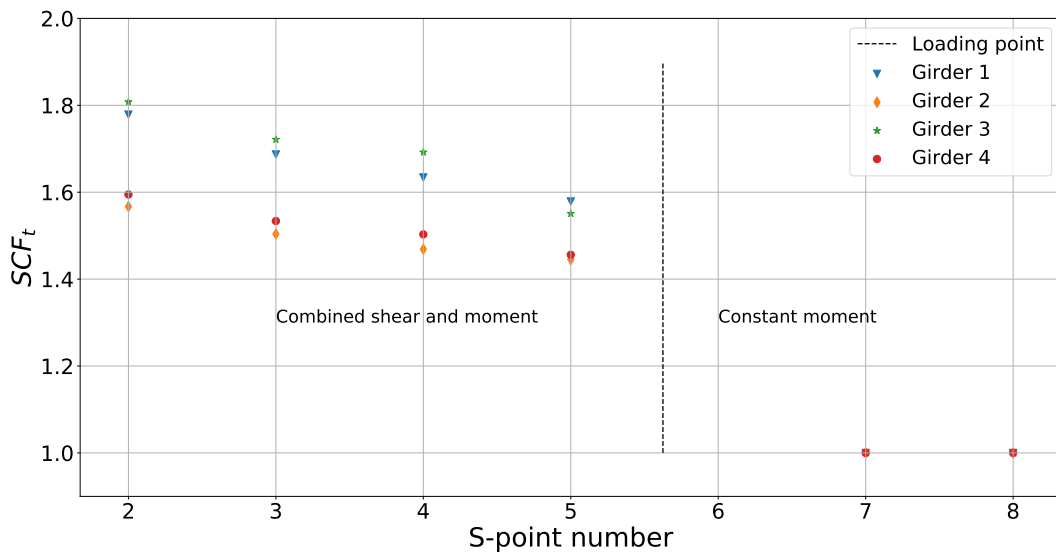


Figure 4.21: Variation of SCF_t at S-points.

Figure 4.22 shows a comparison between the structural hot spot stress obtained from the FE-models (solid lines), calculated with the 1mm stress method, and the structural hot spot stress calculated with the proposed Equation 4.2 (dotted lines). As can be seen, the proposed equation correlates well with the FE-analyses, especially in the combined shear and moment region.

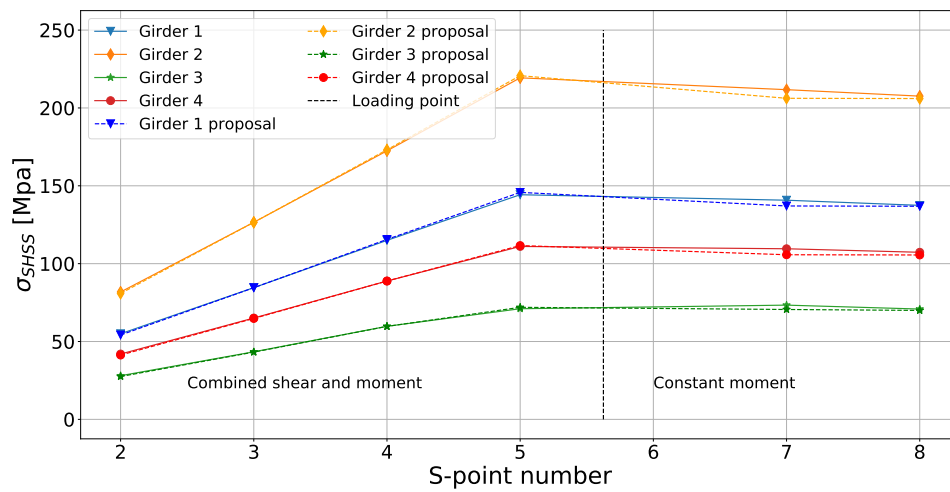


Figure 4.22: Comparison between SHSS obtained from FE-analyses and SHSS calculated with the proposed equation.

5

Discussion

The fatigue aspect in corrugated web girders is a complex question after having analysed previous work of different authors and the results coming from this report. There have been uncertainties regarding the analytical methods, the FE-modeling and the previously executed experiments.

5.1 Analytical methods

As have been stated previously, several geometrical parameters, load cases and boundary conditions affect the fatigue performance of a corrugated web girder. For instance, the support condition in the transverse direction and the load application plays a vital role regarding the transverse deflection mode for the flanges as mentioned by Abbas (2003). This means that the location of the critical S-points changes depending on these parameters. It is possible to predict this analytically with formulas developed by Abbas (2003), although they become quite cumbersome to do so depending on the number of wavelengths, loading schemes and support locations and it might, therefore, be more economical to predict this through numerical investigations. On the other hand, the very simplified Equation 2.4 developed by Kövesdi et al. (2012) to calculate the maximum bending stress subjected to the flanges is useful since it reduces the calculation time tremendously. Although it should be noted once again that the support conditions and loading scheme affect the transverse bending to a great extent, which is not captured in this formula. An example of this can be seen in Figure 4.17, where the difference in transverse support condition between the analysis conducted in this thesis compared to the ones used by Kövesdi et al. (2012) when suggesting Equation 2.4 leads to an overestimation of stresses. This is not mentioned in the new draft of part 1-5 of Eurocode EN:1993:DRAFT (2019) which could be something to consider for upcoming studies and drafts.

The proposed equation (Eq.4.2) for calculating the structural hot spot stress at S-points along the girder is in good agreement with the structural hot spot stresses obtained from FE-analyses, especially in the combined shear and moment region. In the constant moment region, small errors are introduced due to the assumption that transverse bending stresses coming from shear flow in the web in this region are zero. In reality, this is not true since there is a gradual decrease of shear forces into the constant moment zone, owing to that the load is distributed through the

depth of the girder. However, in beam theory, this effect is neglected and the assumption regarding zero shear in the constant moment region is therefore considered reasonable. It should also be noted that in a real bridge case there is seldom any sections along the bridge that experiences solely shear or moment, meaning that the transverse bending of the flanges will be theoretically determinable and thus, the proposed equation will be valid in most practical situations.

As can be seen in Table 4.2b the stress concentration factor for primary bending varies between the girders with long parallel fold (girders 2 and 4) and the girders with short parallel fold (girders 1 and 3). A conclusion can, therefore, be drawn that the length of the parallel fold has an effect on the stress concentration at the S-point, although it is small and most probably negligible compared to the influence of e.g the corrugation angle or the bend radius. With this in mind, it is important to note that the stress concentration factors presented in Table 4.2b and used in Equation 4.2 are only applicable to the corrugation geometries of the tested girders. The corrugation geometry will very likely have a considerable effect on the stress concentration factor for both transverse and primary bending stresses and it is therefore suggested for further research to investigate these effects.

As mentioned before by several authors and seen in Figure 4.20, the magnitude of transverse bending compared to primary bending in a section along a girder can be substantial. In sections with high primary bending stresses, the transverse bending stresses for the test girders are between 15-20% of the primary bending stress. This means that even for a girder (girder 3) that is designed to give a small contribution of transverse bending stresses it still amounts to around 15% of the primary bending stress, which is substantial from a fatigue design point of view. The relevance of these finding from a designer's point of view is therefore substantial.

5.2 FE-modelling

Regarding the modeling of the experimental FE-beams, they are modelled to be accurate when comparing to conventional three and four-point bending tests which have been performed in previous experimental studies. However, as has been stated previously, the boundary conditions and type of loading considerably affect the structural response. In a real bridge case, these factors can initially be hard to predict and are also prone to change during the service life of the structure, which will lead to change in the fatigue response of the CWGs. Therefore, it should be noted that while FE modeling is a useful tool for predicting stress concentrations and deflection modes for CWGs, it could at the same time lead to a degree of false comfort for the designing engineer.

5.3 Experimental tests

After having studied the transverse bending of the flanges thoroughly it became clear that the deflection mode of the bottom flange might play an important role in determining whether girders tested in four-point bending will fail in the combined shear and moment region or the constant moment region. Comparing the deflection mode of the test girders in Section 3.1 to the deflection mode of girders tested in four-point bending from Chapter 2, it can be seen that girders that have half and full corrugation wavelengths in both the combined shear and moment region and the constant moment region deflect differently compared to girders with half wavelengths in one region and whole wavelengths in the other. Girders with half wavelengths in one region and whole wavelengths in the other deflect with a single curvature with the maximum deflection appearing in the constant moment region. Girders with whole wavelengths in both regions on the other hand deflect with a double curvature with the maximum deflection in the combined region. This observation could indicate that girders with half wavelengths in one region and whole wavelengths in the other fail in the constant moment region, and girders with whole wavelengths in both regions fail in the combined shear and moment region. An illustration of the two types of deflection modes observed for the girders mentioned in Section 3.1 and the experimentally tested girders mentioned in Chapter 2 can be seen in Figure 5.1.

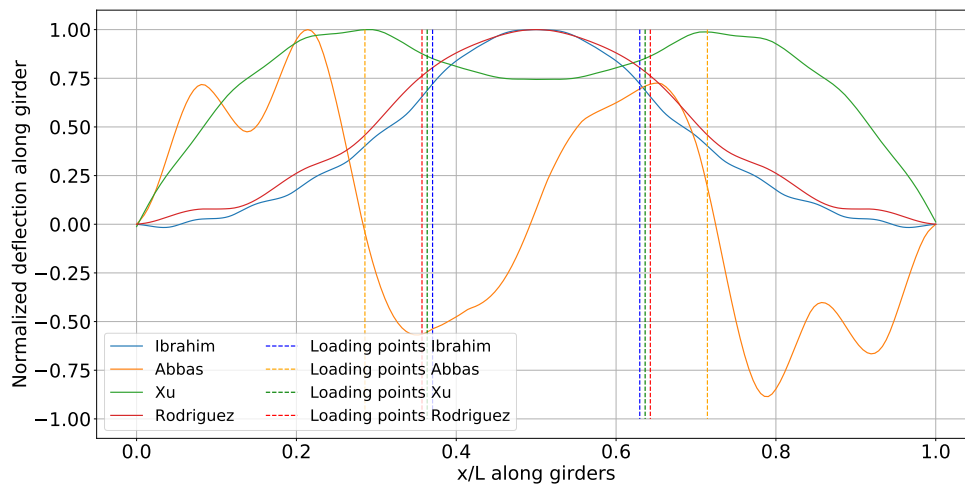


Figure 5.1: Transverse deflection modes for girders from experimental tests mentioned in 2.

The girder from Rodriguez' experiments (2000) is an exception in this case since this girder fails in the combined shear and moment region even though the largest transverse deflection appears in the constant moment region. Explanation for this could be that the weld was poorly executed at the point of failure or another weld defect-related issue existed. It should also be noted that the results obtained by Rodriguez (2000) differ substantially from results obtained from other experiments mentioned in Chapter 2.

6

Conclusions

This report aimed to investigate whether a unified way of calculating corrugated web girders with regard to fatigue can be suggested. As have been discussed in the report, fatigue performance of CWGs can be highly complex to evaluate which previous authors also have experienced. Two issues were noticed to be less commented on within this subject from earlier work, namely the importance of transverse bending and overall experiments on structural hot spot stresses using FE-modeling. Therefore, analyses were performed to investigate both of these topics.

6.1 Concluding remarks

The following conclusions are drawn from this study:

- After conducting statistical analysis on previous fatigue tests on corrugated web girders no statistically significant difference could be seen between corrugation geometry parameters for the test specimens. Moreover, when plotting the test results in an S-N curve a sufficiently narrow scatter band was observed, leading to a suggested fatigue class for corrugated web girders equal to FAT 120.
- Modeling of CWGs with submodels is an efficient way when thorough analyses of the structural hot spot stresses are sought for. However, as the most detailed model yet requires a large amount of computational power, its applicability in general design practice is questionable. However, a global shell model is able to predict transverse and vertical deflection as well for longitudinal stresses. This is valuable both for design and maintenance purposes since the prediction of the locations of the critical fatigue points become substantially more accessible.
- The 1mm stress method proves to provide accurate results when calculating structural hot spot stresses for corrugated web girders. It reduces the processing of FE-modelling results significantly and is recommended by the authors to use for future researchers when conducting e.g parametric studies on the effect of corrugation geometry on fatigue performance.

- The upcoming draft of part 1-5 of Eurocode 3 states that the transverse bending of a corrugated web girder should be considered in the design. The associated formula described in the previous section has been discussed with the conclusion that it is in most cases a conservative expression. However, as it is important to acknowledge its weaknesses, it is also important to stress the fact that this expression will capture the most extreme load situation. This upper bound way of calculating transverse bending stresses will probably provide more confidence for future engineers to design CWGs.
- Investigation on the effect of transverse bending of the bottom flange on the structural hot spot stress at the S-point revealed that the structural hot spot stress can be divided into primary and transverse bending stresses with corresponding stress concentration factors SCF_p and SCF_t , respectively.

6.2 Suggestions for further studies

As mentioned earlier, the stress concentration factors for primary and transverse bending stresses are highly dependent on the corrugation geometry and the SCFs suggested in this thesis are *only* valid for the corrugation geometry of the tested girders. It is therefore suggested to carry out more extensive parametric studies to investigate the effect of corrugation geometry on the stress concentration factors for primary and transverse bending stresses.

References

- AASHTO (2013). *AASHTO LRFD Bridge Design Specifications, customary U.S. units with 2012 and 2013 interim revisions ; and 2012 Errata*. American Association of State Highway and Transportation Officials.
- Abbas, H. H. (2003). *Analysis and design of corrugated web I -girders for bridges using high performance steel*. Ph.D., Lehigh University, United States – Pennsylvania.
- Abbas, H. H., Sause, R., and Driver, R. G. (2006). Behavior of Corrugated Web I-Girders under In-Plane Loads. *Journal of Engineering Mechanics*, 132(8):806–814.
- Abbas, H. H., Sause, R., and Driver, R. G. (2007). Simplified analysis of flange transverse bending of corrugated web I-girders under in-plane moment and shear. *Engineering Structures*, 29(11):2816–2824.
- Al-Emrani, M. and Aygül, M. (2013). Fatigue design of steel and composite bridges. Technical Report 2014:10, Chalmers University of Technology, Göteborg, Sweden.
- Anami, K. and Sause, R. (2005). Fatigue of web-flange weld of corrugated web girders: 2. Analytical evaluation of fatigue strength of corrugated web-flange weld. *International Journal of Fatigue*, 27(4):383–393.
- Baddoo, N. (2017). *Design manual for structural stainless steel - Commentary*. The Steel Construction Institute (SCI), 4th edition.
- Doerk, O., Fricke, W., and Weissenborn, C. (2003). Comparison of different calculation methods for structural stresses at welded joints. *International Journal of Fatigue*, 25(5):359–369.
- EN:1993 (2005). *Eurocode 3: Design of steel structures - Part 1-9: Fatigue*. European Committee for Standardization (CEN), Brussels.
- EN:1993:DRAFT (2019). Eurocode 3: Design of steel structures - Part 1-5: Plated structural elements, upcoming draft.
- Fisher, J. W., Albrecht, P. A., and Yen, B. T. (1974). *Fatigue strength of steel beams with welded stiffeners and attachments*. Number 147 in National cooperative highway research program report. Highway Research Board, Washington, D.C.

- Fisher, J. W., Frank, K. H., Hirt, M. A., and McNamee, B. M. (1970). Effect of Weldments on the Fatigue Strength of Steel Beams. Technical Report 334-2, Lehigh University.
- Harrison, J. (1965). Exploratory Fatigue Tests on Two Girders with Corrugated Webs. *British Welding Journal*, 12(2):121–125.
- Hobbacher, A. (2016). *Recommendations for Fatigue Design of Welded Joints and Components*. IIW Collection. Springer International Publishing, Cham.
- Ibrahim, S. A., El-Dakhakhni, W. W., and Elgaaly, M. (2006). Fatigue of corrugated-web plate girders: Experimental study. *Journal of Structural Engineering*, 132(9):1371–1380.
- Ibrahim, S. A.-B. (2001). *Fatigue analysis and instability problems of plate girders with corrugated webs*. Ph.D., Drexel University, United States – Pennsylvania.
- Karlsson, E. (2018). Stainless Steel Bridge Girders with Corrugated Webs. Master's thesis, Chalmers University of Technology, Gothenburg.
- Korashy, M. and Varga, J. (1979). Comparative Evaluation of Fatigue Strength of Beams with Web Plate Stiffened in the Traditional Way and by Corrugation. *ACTA Technica Academiae Scientiarum Hungaricae*, 89(3-4):309–346.
- Kotaki, N., Ichikawa, A., Sasaki, E., and Hosaka, T. (2003). A of steel girder bridges with ripple web and their fatigue performance. *Tokyo Institute of Technology*.
- Kövesdi, B. and Dunai, L. (2014). Fatigue life of girders with trapezoidally corrugated webs: An experimental study. *International Journal of Fatigue*, 64:22–32.
- Kövesdi, B., Jáger, B., and Dunai, L. (2012). Stress distribution in the flanges of girders with corrugated webs. *Journal of Constructional Steel Research*, 79:204–215.
- Machacek, J. and Tuma, M. (2006). Fatigue life of girders with undulating webs. *Journal of Constructional Steel Research*, 62(1-2):168–177.
- Rodriguez, R. (2000). *Stress distribution and bearing stiffeners details related to fatigue and fracture of steel girders with corrugated webs*. Ph.D., Drexel University, United States – Pennsylvania.
- Rong, L., Yuqing, L., Bohai, J., Manman, W., and Yuan, T. (2014). Hot spot stress analysis on rib–deck welded joint in orthotropic steel decks | Elsevier Enhanced Reader. *Journal of Constructional Steel Research*.
- Sause, R., Abbas, H. H., Wassef, W. G., Driver, R. G., and Elgaaly, M. (2003). Corrugated web girder shape and strength criteria.
- Schneider, C. R. A. and Maddox, S. J. (2003). *Best Practice Guide on Statistical Analysis of Fatigue Data*. International Institute of Welding, United Kingdom.

-
- Sedlacek, G., Hobbacher, A., Schleich, J. B., Nussbaumer, A., Maddox, S. J., Brozzetti, J., Chabrolin, B., Helmerich, R., Piraprez, E., and Kleineidam, P. (2003). 1st draft of the background document prEN 1993-1-9. *RWTH Institute of Steel Construction, Germany*.
- Smith, M. (2009). *ABAQUS/Standard User's Manual, Version 6.9*. Dassault Systèmes Simulia Corp, Providence, RI, United States.
- Wang, Z. (2020). Clarification of Stresses in CWGs subjected to three-point bending.
- Wang, Z., Tan, L., and Wang, Q. (2013a). Fatigue strength evaluation of welded structural details in corrugated steel web girders. *International Journal of Steel Structures*, 13(4):707–721.
- Wang, Z., Wang, Q., and Jiang, R. (2015). Finite element based fatigue assessment of corrugated steel web beams in highway bridges. *International Journal of Civil Engineering*, 13(4).
- Wang, Z. Y., Wang, Q. Y., and Zhang, Y. Q. (2013b). Fatigue Strength of Longitudinal Welded Joints with Steel Corrugated Plates. In *Proceedings of the Thirteenth East Asia-Pacific Conference on Structural Engineering and Construction (EASEC-13)*, pages C–4. The Thirteenth East Asia-Pacific Conference on Structural Engineering and Construction (EASEC-13).
- Xiao, Z. G. and Yamada, K. (2004). A method of determining geometric stress for fatigue strength evaluation of steel welded joints. *International Journal of Fatigue*, 26(12):1277–1293.
- Xu, J., Sun, H., Cai, S., Sun, W., and Zhang, B. (2019). Fatigue testing and analysis of I-girders with trapezoidal corrugated webs. *Engineering Structures*, 196:109344.

A

Python script used to model
corrugated web girders

```

# -*- coding: mbc3 -*-
1  from part import *
2  from material import *
3  from section import *
4  from assembly import *
5  from step import *
6  from interaction import *
7  from load import *
8  from mesh import *
9  from optimization import *
10 from job import *
11 from sketch import *
12 from visualization import *
13 from connectorBehavior import *
14
15 import math
16 import regionToolset
17
18 #-----INPUT DATA-----
19
20 # Material parameters
21 elastic_modulus =          # Elastic modulus [Pa]
22 poissons_ratio =         # Poissons ratio
23
24 # I-section
25 web_height =              # Web height [m]
26 t_w =                    # Web thickness [m]
27 b_f =                    # Flange width [m]
28 t_f =                    # Flange thickness [m]
29
30 # Corrugation geometry
31 corr_depth =              # Corrugation depth [m]
32 l_par =                   # Parallel fold length [m]
33 corr_ang =                # Corrugation angle in degrees
34
35 # Model settings global model
36 num_tot_wavelengths =     # Number of total wavelengths on the girder
37 point_load =              # Point load magnitude [N]
38 load_position =           # Load application, ex 5 = end of 5th wavelength from left support
39 sym = 'false'             # Symmetry condition or not. 'false' = no symmetry.
40 global_element_size =    # Global element size
41
42 # Model settings intermediate model
43 bend_radius =             # Bend radius [m]
44 weld_throat_thickness =   # Weld throat thickness [m]
45 intermediate_element_type = # Type of elements in intermediate model. 'free' for free mesh, 'quad' for structured mesh
46 intermediate_element_size = # Element size for intermediate model
47 intermediate_model_position = # Wavelength of interest, 1 = first wavelength and so on
48
49 # Model settings S-point model
50 s_point_element_size =    # Element size for S-point model
51 web_height_s_point =     # Height of web in S-point model
52
53 #-----START OF SCRIPT-----
54
55 ## DEBUG MODE, when debug mode is on the analyses are not submitted
56 debug = 1                 # 1 = debug mode on, 0 = debug mode off
57 ## DEBUG MODE
58
59 # Determining number of wavelengths for the model, if symmetry
60 if sym == 'false':
61     num_wavelengths = (num_tot_wavelengths)          # Number of wavelengths in case of no symmetry
62     num_full_wavelengths = int(num_wavelengths)      # Number of whole wavelengths, no symmetry
63     rest_wavelength = num_wavelengths-num_full_wavelengths # Number of partial wavelengths remaining, 0.25=quarter wavelength
64 else:
65     num_wavelengths = (num_tot_wavelengths/2.0)     # Number of wavelengths on the symmetry girder
66     num_full_wavelengths = int(num_wavelengths)     # Number of whole wavelengths on symmetry girder
67     rest_wavelength = num_wavelengths-num_full_wavelengths # Number of partial wavelengths remaining ,# 0.25=quarter wavelength
68
69 # Coordinates and parameters used in script
70 l_par = l_par/2
71 # Angles
72 corr_ang=corr_ang*(2*pi/360)          # Corrugation angle in radians for script
73 weld_ang=45*(2*pi/360)                # Weld angle in radians for script
74

```

```

78 # Y - coordinates
79 corr_amp=corr_depth/2 # Corrugation amplitude [m]
80 web_height_global=web_height+t_f # Web height used in shell model [m]
81 half_web_thickness=t_w/2 # Half of web thickness [m]
82
83 # X - coordinates
84 proj_l_inc = corr_amp/math.tan(corr_ang) # Projected length of inclined fold
85 l_wavelength=4*(proj_l_inc+l_par) # Length of wavelength [m]
86 quarter_wavelength = proj_l_inc+l_par # Length of a quarter wavelength
87 load_position = 5*l_wavelength # Load application, distance from support [m]
88 s_point_model_position = intermediate_model_position-0.5 # Position of S-point within intermediate model
89
90
91 #-----GLOBAL MODEL-----
92
93
94 # Change name of model
95 mdb.models.changeKey(fromName='Model-1', toName='global_model')
96 global_model = mdb.models['global_model']
97
98 ## Create quarter wavelength
99
100 # Create web part
101 global_model.ConstrainedSketch(name='web_sketch_global', sheetSize=10.0)
102 web_sketch_global = global_model.sketches['web_sketch_global']
103 web_sketch_global.Line(point1=(0.0, 0.0), point2=(proj_l_inc, -corr_amp))
104 web_sketch_global.Line(point1=(proj_l_inc, -corr_amp), point2=(quarter_wavelength, -corr_amp))
105 global_model.Part(dimensionality=THREE_D, name='Part1', type=DEFORMABLE_BODY)
106 global_part_1 = global_model.parts['Part1']
107 global_part_1.BaseShellExtrude(depth=web_height_global, sketch=web_sketch_global)
108
109 del web_sketch_global
110
111 # Create datum planes for flanges
112 global_datumpl1 = global_part_1.DatumPlaneByPrincipalPlane(offset=0.0, principalPlane=XYPLANE)
113 global_datumpl1 = global_part_1.datums[global_datumpl1.id]
114
115 global_datumpl2 = global_part_1.DatumPlaneByPrincipalPlane(offset=web_height_global, principalPlane=XYPLANE)
116 global_datumpl2 = global_part_1.datums[global_datumpl2.id]
117
118 # Create bottom flange
119 global_model.ConstrainedSketch(gridSpacing=0.02, name='bot_flange_sketch_global',
120 sheetSize=1.05, transform=global_part_1.MakeSketchTransform(
121 sketchPlane=global_datumpl1,
122 sketchPlaneSide=SIDE1,
123 sketchUpEdge=global_part_1.edges.findAt((proj_l_inc+l_par/2,-corr_amp,web_height_global),),
124 sketchOrientation=BOTTOM, origin=(0.0, 0.0, 0.0)))
125 bot_flange_sketch_global = global_model.sketches['bot_flange_sketch_global']
126 bot_flange_sketch_global.rectangle(point1=(0, b_f/2), point2=(quarter_wavelength, -b_f/2))
127 global_part_1.Shell(sketch=bot_flange_sketch_global)
128
129 del bot_flange_sketch_global
130
131 # Create top flange
132 global_model.ConstrainedSketch(gridSpacing=0.02, name='top_flange_sketch_global',
133 sheetSize=1.09, transform=
134 global_part_1.MakeSketchTransform(
135 sketchPlane=global_datumpl2,
136 sketchPlaneSide=SIDE1,
137 sketchUpEdge=global_part_1.edges.findAt((proj_l_inc+l_par/2,-corr_amp,web_height_global),),
138 sketchOrientation=BOTTOM, origin=(0.0, 0.0, web_height_global)))
139 top_flange_sketch_global = global_model.sketches['top_flange_sketch_global']
140 top_flange_sketch_global.rectangle(point1=(0, b_f/2), point2=(quarter_wavelength, -b_f/2))
141
142 global_part_1.Shell(sketch=top_flange_sketch_global,
143 sketchOrientation=BOTTOM,
144 sketchPlane=global_datumpl2,
145 sketchPlaneSide=SIDE1, sketchUpEdge=
146 global_part_1.edges.findAt((proj_l_inc+l_par/2,-corr_amp,web_height_global),))
147
148 del top_flange_sketch_global
149
150
151 # Create material
152 global_model.Material(name='Steel')
153 global_model.materials['Steel'].Elastic(table=((elastic_modulus, poissons_ratio),))
154
155 # Create Flange and web sections

```

```

156 global_model.HomogeneousShellSection(idealization=NO_IDEALIZATION,
157     integrationRule=SIMPSON, material='Steel', name='Flange',
158     nodalThicknessField="", numIntPts=5, poissonDefinition=DEFAULT,
159     preIntegrate=OFF, temperature=GRADIENT, thickness=t_f, thicknessField="",
160     thicknessModulus=None, thicknessType=UNIFORM, useDensity=OFF)
161 global_model.HomogeneousShellSection(idealization=NO_IDEALIZATION,
162     integrationRule=SIMPSON, material='Steel', name='Web', nodalThicknessField="",
163     numIntPts=5, poissonDefinition=DEFAULT, preIntegrate=OFF, temperature=
164     GRADIENT, thickness=t_w, thicknessField="", thicknessModulus=None,
165     thicknessType=UNIFORM, useDensity=OFF)
166
167 # Partition quarter wavelength
168 p1 = (proj_l_inc, 0, 0)
169 p2 = (proj_l_inc, -b_f/2, 0)
170 p3 = (proj_l_inc, 0, web_height_global)
171 p4 = (proj_l_inc, -b_f/2, web_height_global)
172
173 global_model.ConstrainedSketch(gridSpacing=0.02, name='partition_sketch_global',
174     sheetSize=1.1, transform=global_part_1.MakeSketchTransform(
175     sketchPlane=global_datump12,
176     sketchPlaneSide=SIDE1,
177     sketchUpEdge=global_part_1.edges.findAt((proj_l_inc,-b_f/2,web_height_global),),
178     sketchOrientation=BOTTOM, origin=(0.0, 0.0, web_height_global)))
179 partition_sketch_global = global_model.sketches['partition_sketch_global']
180 partition_sketch_global.Line(point1=(proj_l_inc, -corr_amp), point2=(proj_l_inc, b_f/2))
181 partition_sketch_global.Line(point1=(proj_l_inc, -corr_amp), point2=(proj_l_inc, -b_f/2))
182 global_part_1.PartitionFaceBySketchThruAll(
183     faces=global_part_1.faces.findAt(((p1),), ((p2),), ((p3),), ((p4),)),
184     sketch=partition_sketch_global, sketchOrientation=BOTTOM,
185     sketchPlane=global_datump12, sketchPlaneSide=SIDE1,
186     sketchUpEdge=global_part_1.edges.findAt((proj_l_inc,-b_f/2,web_height_global),))
187
188 del partition_sketch_global
189
190
191 # Copy and mirroring quarter wavelength for creation of symmetry girder
192 global_model.Part(compressFeatureList=ON, mirrorPlane=YZPLANE, name=
193     'global_part_2', objectToCopy=global_part_1)
194 global_part_2 = global_model.parts['global_part_2']
195
196 global_model.Part(compressFeatureList=ON, mirrorPlane=XZPLANE, name=
197     'global_part_3', objectToCopy=global_part_1)
198 global_part_3 = global_model.parts['global_part_3']
199
200 global_model.Part(compressFeatureList=ON, mirrorPlane=XZPLANE, name=
201     'global_part_4', objectToCopy=global_part_2)
202 global_part_4 = global_model.parts['global_part_4']
203
204 ## Assigning flange and web sections to parts
205
206 # Assign sections to first quarter
207 pf11 = (0, b_f/2, 0)
208 pf21 = (0, -b_f/2, 0)
209 pf31 = (quarter_wavelength, b_f/2, 0)
210 pf41 = (quarter_wavelength, -b_f/2, 0)
211 pf51 = (0, b_f/2, web_height_global)
212 pf61 = (0, -b_f/2, web_height_global)
213 pf71 = (quarter_wavelength, b_f/2, web_height_global)
214 pf81 = (quarter_wavelength, -b_f/2, web_height_global)
215 pw11 = (0, 0, web_height_global/2)
216 pw21 = (quarter_wavelength, -corr_amp, web_height_global/2)
217
218 global_part_1.SectionAssignment(offset=0.0, offsetField="",
219     offsetType=MIDDLE_SURFACE, region=Region(
220     faces=global_part_1.faces.findAt(((pf11),), ((pf21),),
221     ((pf31),), ((pf41),), ((pf51),), ((pf61),), ((pf71),), ((pf81),))),
222     sectionName='Flange', thicknessAssignment=FROM_SECTION)
223 global_part_1.SectionAssignment(offset=0.0, offsetField="",
224     offsetType=MIDDLE_SURFACE, region=Region(
225     faces=global_part_1.faces.findAt(((pw11),), ((pw21),))),
226     sectionName='Web', thicknessAssignment=FROM_SECTION)
227
228 # Assign sections to second quarter
229 pf12 = (0, b_f/2, 0)
230 pf22 = (0, -b_f/2, 0)
231 pf32 = (-proj_l_inc-l_par, b_f/2, 0)
232 pf42 = (-proj_l_inc-l_par, -b_f/2, 0)
233 pf52 = (0, b_f/2, web_height_global)

```

```

234 pf62 = (0, -b_f/2, web_height_global)
235 pf72 = (-proj_l_inc-l_par, b_f/2, web_height_global)
236 pf82 = (-proj_l_inc-l_par, -b_f/2, web_height_global)
237 pw12 = (0, 0, web_height_global/2)
238 pw22 = (-proj_l_inc-l_par, -corr_amp, web_height_global/2)
239
240 global_part_2.SectionAssignment(offset=0.0, offsetField="",
241   offsetType=MIDDLE_SURFACE, region=Region(
242     faces=global_part_2.faces.findAt(((pf12),), ((pf22),), ((pf32),),
243     ((pf42),), ((pf52),), ((pf62),), ((pf72),), ((pf82),))),
244     sectionName='Flange', thicknessAssignment=FROM_SECTION)
245 global_part_2.SectionAssignment(offset=0.0, offsetField="",
246   offsetType=MIDDLE_SURFACE, region=Region(
247     faces=global_part_2.faces.findAt(((pw12),), ((pw22),))),
248     sectionName='Web', thicknessAssignment=FROM_SECTION)
249
250 # Assign sections to third quarter
251 pf13 = (0, -b_f/2, 0)
252 pf23 = (0, b_f/2, 0)
253 pf33= (quarter_wavelength, -b_f/2, 0)
254 pf43 = (quarter_wavelength, b_f/2, 0)
255 pf53 = (0, -b_f/2, web_height_global)
256 pf63 = (0, +b_f/2, web_height_global)
257 pf73 = (quarter_wavelength, -b_f/2, web_height_global)
258 pf83 = (quarter_wavelength, b_f/2, web_height_global)
259 pw13 = (0, 0, web_height_global/2)
260 pw23 = (quarter_wavelength, corr_amp, web_height_global/2)
261
262 global_part_3.SectionAssignment(offset=0.0, offsetField="",
263   offsetType=MIDDLE_SURFACE, region=Region(
264     faces=global_part_3.faces.findAt(((pf13),), ((pf23),), ((pf33),),
265     ((pf43),), ((pf53),), ((pf63),), ((pf73),), ((pf83),))),
266     sectionName='Flange', thicknessAssignment=FROM_SECTION)
267 global_part_3.SectionAssignment(offset=0.0, offsetField="",
268   offsetType=MIDDLE_SURFACE, region=Region(
269     faces=global_part_3.faces.findAt(((pw13),), ((pw23),))),
270     sectionName='Web', thicknessAssignment=FROM_SECTION)
271
272 # Assign sections to fourth quarter
273 pf14 = (0, -b_f/2, 0)
274 pf24 = (0, b_f/2, 0)
275 pf34= (-proj_l_inc-l_par, -b_f/2, 0)
276 pf44 = (-proj_l_inc-l_par, b_f/2, 0)
277 pf54 = (0, -b_f/2, web_height_global)
278 pf64 = (0, +b_f/2, web_height_global)
279 pf74 = (-proj_l_inc-l_par, -b_f/2, web_height_global)
280 pf84 = (-proj_l_inc-l_par, b_f/2, web_height_global)
281 pw14 = (0, 0, web_height_global/2)
282 pw24 = (-proj_l_inc-l_par, corr_amp, web_height_global/2)
283
284 global_part_4.SectionAssignment(offset=0.0, offsetField="",
285   offsetType=MIDDLE_SURFACE, region=Region(
286     faces=global_part_4.faces.findAt(((pf14),), ((pf24),),
287     ((pf34),), ((pf44),), ((pf54),), ((pf64),), ((pf74),), ((pf84),))),
288     sectionName='Flange', thicknessAssignment=FROM_SECTION)
289 global_part_4.SectionAssignment(offset=0.0, offsetField="",
290   offsetType=MIDDLE_SURFACE, region=Region(
291     faces=global_part_4.faces.findAt(((pw14),), ((pw24),))),
292     sectionName='Web', thicknessAssignment=FROM_SECTION)
293
294 # Insert quarter wavelength instances
295 global_model.rootAssembly.DatumCsysByDefault(CARTESIAN)
296 global_model.rootAssembly.Instance(dependent=OFF, name='Part1-1',
297   part=global_part_1)
298 global_model.rootAssembly.Instance(dependent=OFF, name='Part2-1',
299   part=global_part_2)
300 global_model.rootAssembly.Instance(dependent=OFF, name='Part3-1',
301   part=global_part_3)
302 global_model.rootAssembly.Instance(dependent=OFF, name='Part4-1',
303   part=global_part_4)
304 global_model.rootAssembly.translate(instanceList=('Part2-1', ),
305   vector=(l_wavelength/2, 0.0, 0.0))
306 global_model.rootAssembly.translate(instanceList=('Part3-1', ),
307   vector=(l_wavelength/2, 0.0, 0.0))
308 global_model.rootAssembly.translate(instanceList=('Part4-1', ),
309   vector=(l_wavelength, 0.0, 0.0))
310
311 # Considering partial wavelengths
312 if root_wavelength == 0.25:

```

```

312     rest_wavelength == 0.25:
313         w1 = int(num_full_wavelengths)+1
314         w2 = int(num_full_wavelengths)
315         w3 = int(num_full_wavelengths)
316         w4 = int(num_full_wavelengths)
317     elif rest_wavelength == 0.5:
318         w1 = int(num_full_wavelengths)+1
319         w2 = int(num_full_wavelengths)+1
320         w3 = int(num_full_wavelengths)
321         w4 = int(num_full_wavelengths)
322     elif rest_wavelength == 0.75:
323         w1 = int(num_full_wavelengths)+1
324         w2 = int(num_full_wavelengths)+1
325         w3 = int(num_full_wavelengths)+1
326         w4 = int(num_full_wavelengths)
327     else:
328         w1 = int(num_full_wavelengths)
329         w2 = int(num_full_wavelengths)
330         w3 = int(num_full_wavelengths)
331         w4 = int(num_full_wavelengths)
332
333     # Linear pattern of quarter wavelengths
334     global_model.rootAssembly.LinearInstancePattern(direction1=(1.0, 0.0,
335         0.0), direction2=(0.0, 1.0, 0.0), instanceList=('Part1-1', ), number1=w1,
336         number2=1, spacing1=l_wavelength, spacing2=0.15)
337     global_model.rootAssembly.LinearInstancePattern(direction1=(1.0, 0.0,
338         0.0), direction2=(0.0, 1.0, 0.0), instanceList=('Part2-1', ), number1=(w2),
339         number2=1, spacing1=l_wavelength, spacing2=0.15)
340     global_model.rootAssembly.LinearInstancePattern(direction1=(1.0, 0.0,
341         0.0), direction2=(0.0, 1.0, 0.0), instanceList=('Part3-1', ), number1=(w3),
342         number2=1, spacing1=l_wavelength, spacing2=0.15)
343     global_model.rootAssembly.LinearInstancePattern(direction1=(1.0, 0.0,
344         0.0), direction2=(0.0, 1.0, 0.0), instanceList=('Part4-1', ), number1=(w4),
345         number2=1, spacing1=l_wavelength, spacing2=0.15)
346
347     # Rotate instances for correct coordinate system
348     all_instances=global_model.rootAssembly.instances
349     global_model.rootAssembly.rotate(angle=-90.0, axisDirection=(1.0, 0.0, 0.0),
350         axisPoint=(0.0, 0.0, 0.0), instanceList=(all_instances.keys()))
351
352     # Merge instances into CWG and delete quarter instances
353     global_model.rootAssembly.InstanceFromBooleanMerge(domain=GEOMETRY,
354         instances=all_instances.values(),
355         keepIntersections=ON, name='global_model_cwg', originalInstances=DELETE)
356
357     # Name CWG instance and part
358     global_model_instance = global_model.rootAssembly.instances['global_model_cwg-1']
359     global_model_cwg = global_model.parts['global_model_cwg']
360
361     # Create load step
362     global_model.StaticStep(name='load_step', previous='Initial')
363
364     # Create support constraint
365     origo = (0,0,0)
366     L = (num_wavelengths*l_wavelength)
367     end = (L,0,-corr_amp)
368     sf1 = (0,0,-b_f/2+(b_f/2-corr_amp)/2)
369     sf2 = (0,0,b_f/2-(b_f/2-corr_amp)/2)
370     sf3 = (0,web_height_global,-b_f/2+(b_f/2-corr_amp)/2)
371     sf4 = (0,web_height_global,b_f/2-(b_f/2-corr_amp)/2)
372     sw = (0,web_height_global/2,0)
373
374     global_model.MultipointConstraint(controlPoint=Region(
375         vertices=global_model_instance.vertices.findAt(((origo),)),
376         csys=None, mpcType=BEAM_MPC, name='Support constraint', surface=Region(
377         edges=global_model_instance.edges.findAt(((sf1),),
378         ((sf2),), ((sf3),), ((sf4),), ((sw),))),
379         userMode=DOF_MODE_MPC, userType=0)
380
381     # Create constraint at symmetry line/end of girder
382     if rest_wavelength == 0:
383         pw_endpoint = 0
384     elif rest_wavelength == 0.25:
385         pw_endpoint = corr_amp
386     elif rest_wavelength == 0.5:
387         pw_endpoint = 0
388     elif rest_wavelength == 0.75:
389         pw_endpoint = -corr_amp
390
391

```

```

391 web_endpoint = (L,web_height_global/2,pw_endpoint)
392 end_point = (L,0,pw_endpoint)
393
394 syf1 = (L,0,-b_f/2+(b_f/2-corr_amp)/2)
395 syf2 = (L,0,b_f/2-(b_f/2-corr_amp)/2)
396 syf3 = (L,web_height_global,-b_f/2+(b_f/2-corr_amp)/2)
397 syf4 = (L,web_height_global,b_f/2-(b_f/2-corr_amp)/2)
398 syw = (L,web_height_global/2,-corr_amp)
399
400 global_model.MultipointConstraint(controlPoint=Region(
401     vertices=global_model_instance.vertices.findAt(((end_point))),
402     csys=None, mpcType=BEAM_MPC, name='Symmetry Constraint', surface=Region(
403     edges=global_model_instance.edges.findAt(((syf1),),
404     ((syf2),), ((syf3),), ((syf4),), ((web_endpoint))),),
405     userMode=DOF_MODE_MPC, userType=0)
406
407 # Create support BC
408 global_model.DisplacementBC(amplitude=UNSET, createStepName='Initial',
409     distributionType=UNIFORM, fieldName="", localCsys=None, name='Support BC',
410     region=Region(
411     vertices=global_model_instance.vertices.findAt(((origo))),),
412     u1=UNSET, u2=SET, u3=SET, ur1=SET, ur2=UNSET, ur3=UNSET)
413
414 if sym == 'false':
415     # Create second BC in case of full girder
416     global_model.DisplacementBC(amplitude=UNSET, createStepName='Initial',
417     distributionType=UNIFORM, fieldName="", localCsys=None, name='End Support BC',
418     region=Region(
419     vertices=global_model_instance.vertices.findAt(((end_point))),),
420     u1=SET, u2=SET, u3=SET, ur1=SET, ur2=UNSET, ur3=UNSET)
421 else:
422     # Create BC at symmetry line
423     global_model.XsymmBC(createStepName='Initial', localCsys=None, name=
424     'Symmetry BC', region=Region(
425     vertices=global_model_instance.vertices.findAt(((end_point))))))
426
427 # Create point load
428 global_model.ConcentratedForce(cf2=-point_load, createStepName='load_step',
429     distributionType=UNIFORM, field="", localCsys=None, name='Point load',
430     region=Region(
431     vertices=global_model_instance.vertices.findAt(((load_position,web_height_global,0))))))
432
433 # Create second point load in case of full girder
434 if sym == 'false':
435     global_model.ConcentratedForce(cf2=-point_load, createStepName='load_step',
436     distributionType=UNIFORM, field="", localCsys=None, name='Point load 2',
437     region=Region(
438     vertices=global_model_instance.vertices.findAt(((L-load_position,web_height_global,0))))))
439
440 # Create mesh for the global model
441 global_model_cwg.seedPart(deviationFactor=0.1,
442     minSizeFactor=0.1, size=global_element_size)
443 global_model_cwg.setMeshControls(elemShape=QUAD,
444     regions=global_model_cwg.faces,
445     technique=STRUCTURED)
446 global_model_cwg.setElementType(elemTypes=(ElemType(
447     elemCode=S8R, elemLibrary=STANDARD), ElemType(elemCode=STRI65,
448     elemLibrary=STANDARD)), regions=(
449     global_model_cwg.faces,))
450 global_model_cwg.generateMesh()
451
452 # Flip positive - negative normal of shell elements so that faces that share common plane have the same normal
453 p_normal1 = [0] * num_full_wavelengths
454 p_normal2 = [0] * num_full_wavelengths
455 p_normal3 = [0] * num_full_wavelengths
456 p_normal4 = [0] * num_full_wavelengths
457 for i in range(0,num_full_wavelengths,1):
458     p_normal1[i] = (i*_wavelength+3*_l_wavelength/4-l_par/2,web_height_global/2,-corr_amp)
459     p_normal2[i] = (i*_wavelength+_l_wavelength/2+proj_l_inc/2,web_height_global/2,-corr_amp/2)
460     p_normal3[i] = (i*_wavelength+_l_wavelength-proj_l_inc/2,web_height_global/2,-corr_amp/2)
461     p_normal4[i] = (i*_wavelength+3*_l_wavelength/4+_l_par/2,web_height_global/2,-corr_amp)
462
463 p_normal1=tuple(p_normal1)
464 p_normal2=tuple(p_normal2)
465 p_normal3=tuple(p_normal3)
466 p_normal4=tuple(p_normal4)
467 p_normal_tot=p_normal1+p_normal2+p_normal3+p_normal4
468

```

```

469 # Flip normal for ev. additional partial wavelength
470 if rest_wavelength == 0.75:
471     p_normal_end=[0]*2
472     p_normal_end[0]= (num_full_wavelengths*l_wavelength+l_wavelength/2+proj_l_inc/2,web_height_global/2,-corr_amp/2)
473     p_normal_end[1]= (num_full_wavelengths*l_wavelength+3*l_wavelength/4-l_par/2,web_height_global/2,-corr_amp)
474     p_normal_tot=p_normal_tot+tuple(p_normal_end)
475
476 global_model_cwg.flipNormal(regions=Region(
477     faces=global_model_cwg.faces.findAt(coordinates=p_normal_tot,))
478 global_model.rootAssembly.regenerate()
479
480 # Create global job
481 global_analysis = mdb.Job(atTime=None, contactPrint=OFF, description="", echoPrint=OFF,
482     explicitPrecision=SINGLE, getMemoryFromAnalysis=True, historyPrint=OFF,
483     memory=90, memoryUnits=PERCENTAGE, model='global_model', modelPrint=OFF,
484     multiprocessingMode=DEFAULT, name='global_analysis', nodalOutputPrecision=
485     SINGLE, numCpus=1, numGPUs=0, queue=None, resultsFormat=ODB, scratch="",
486     type=ANALYSIS, userSubroutine="", waitHours=0, waitMinutes=0)
487
488 # Submit global job
489 if debug == 0:
490     global_analysis.submit(consistencyChecking=OFF)
491
492
493 #-----INTERMEDIATE MODEL-----
494
495
496 # Create intermediate model
497 mdb.Model(globalJob='global_analysis', modelType=STANDARD_EXPLICIT, name='intermediate_model',
498 shellToSolid=ON)
499 intermediate_model = mdb.models['intermediate_model']
500
501 ## Create quarter wavelength for intermediate model
502
503 # Create web part
504 intermediate_model.ConstrainedSketch(name='intermediate_web_sketch', sheetSize=20.0)
505 intermediate_web_sketch = intermediate_model.sketches['intermediate_web_sketch']
506
507 inc_line = intermediate_web_sketch.Line(
508     point1=(0.0, half_web_thickness/math.cos(corr_ang)),
509     point2=(proj_l_inc+math.tan(corr_ang/2)*half_web_thickness, -corr_amp+half_web_thickness))
510
511 par_line = intermediate_web_sketch.Line(
512     point1=(proj_l_inc+math.tan(corr_ang/2)*half_web_thickness, -corr_amp+half_web_thickness),
513     point2=(quarter_wavelength, -corr_amp+half_web_thickness))
514
515 bend = intermediate_web_sketch.FilletByRadius(curve1=inc_line, curve2=par_line,
516     nearPoint1=(0.0, half_web_thickness/math.cos(corr_ang)),
517     nearPoint2=(quarter_wavelength, -corr_amp+half_web_thickness), radius=bend_radius)
518
519 offset_line = intermediate_web_sketch.offset(distance=t_w, objectList=(inc_line, par_line, bend), side=RIGHT)
520
521 left_line = intermediate_web_sketch.Line(
522     point1=(0.0, half_web_thickness/math.cos(corr_ang)),
523     point2=(0.0, -half_web_thickness/math.cos(corr_ang)))
524
525 right_line = intermediate_web_sketch.Line(
526     point1=(quarter_wavelength, -corr_amp+half_web_thickness),
527     point2=(quarter_wavelength, -corr_amp-half_web_thickness))
528
529 p1 = (-0.001, -half_web_thickness/math.cos(corr_ang)+0.001*math.tan(corr_ang))
530
531 intermediate_web_sketch.autoTrimCurve(curve1= intermediate_web_sketch.geometry.findAt(p1) , point1=(p1))
532
533 intermediate_model.Part(dimensionality=THREE_D, name='intermediate_part_1', type=
534     DEFORMABLE_BODY)
535
536 intermediate_part_1 = intermediate_model.parts['intermediate_part_1']
537 intermediate_part_1.BaseSolidExtrude(depth=web_height/6, sketch=intermediate_web_sketch)
538
539 del intermediate_model.sketches['intermediate_web_sketch']
540
541 # Create datum planes for flange
542 intermediate_datump1 = intermediate_part_1.DatumPlaneByPrincipalPlane(offset=0.0, principalPlane=XYPLANE)
543 intermediate_datump1 = intermediate_part_1.datums[intermediate_datump1.id]
544
545 # Create flange
546 intermediate_model.ConstrainedSketch(gridSpacing=0.02, name='flange_sketch_intermediate',
547     sheetSize=1.05, transform=

```

```

547 intermediate_part_1.MakeSketchTransform(
548 sketchPlane=intermediate_datumpl1,
549 sketchPlaneSide=SIDE1,
550 sketchUpEdge=intermediate_part_1.edges.findAt((proj_l_inc+9*l_par/10, -corr_amp+half_web_thickness, 0.0)),
551 sketchOrientation=BOTTOM, origin=(0.0, 0.0, 0.0))
552 flange_sketch_intermediate = intermediate_model.sketches['flange_sketch_intermediate']
553 flange_sketch_intermediate.rectangle(point1=(0, b_f/2), point2=(quarter_wavelength, -b_f/2))
554
555 intermediate_part_1.SolidExtrude(depth=t_f,
556 flipExtrudeDirection=ON, sketch=flange_sketch_intermediate,
557 sketchOrientation=BOTTOM, sketchPlane=intermediate_datumpl1,
558 sketchPlaneSide=SIDE1, sketchUpEdge=
559 intermediate_part_1.edges.findAt((proj_l_inc+9*l_par/10, -corr_amp+half_web_thickness, 0.0),))
560
561 del intermediate_model.sketches['flange_sketch_intermediate']
562
563 # Create fillet welds
564 p1_top = (0.01, half_web_thickness/math.cos(corr_ang)-math.tan(corr_ang)*0.01, 0.0)
565 p1_bot = (0.01, -half_web_thickness/math.cos(corr_ang)-math.tan(corr_ang)*0.01, 0.0)
566 p2_bot = (proj_l_inc+9*l_par/10, -corr_amp-half_web_thickness, 0.0)
567
568 chamf_edge_top = intermediate_part_1.edges.findAt((p1_top),)
569 chamf_edge_bot1 = intermediate_part_1.edges.findAt((p1_bot),)
570 chamf_edge_bot2 = intermediate_part_1.edges.findAt((p2_bot),)
571
572 chamf_edges_top = chamf_edge_top.getAdjacentEdges()
573 chamf_edges_bot1 = chamf_edge_bot1.getAdjacentEdges()
574
575 intermediate_part_1.Chamfer(edgeList=(
576 chamf_edges_top[2], chamf_edges_top[3], chamf_edges_bot1[1], chamf_edge_bot1, chamf_edge_bot2),
577 length=weld_throat_thickness/math.cos(weld_ang))
578
579 # Partition cells of quarter wavelength
580 if intermediate_element_type != 'free':
581 # Flange cell
582 cell_1 = ((quarter_wavelength)/2, b_f/2, 0.0)
583 flange_cell = intermediate_part_1.PartitionCellByDatumPlane(datumPlane=intermediate_datumpl1,
584 cells=intermediate_part_1.cells.findAt((cell_1),))
585
586 # Weld cell
587 cell_2 = ((proj_l_inc)/2, -corr_amp/2, 0.0)
588 weld_cell = intermediate_part_1.PartitionCellByPlanePointNormal(
589 cells=intermediate_part_1.cells.findAt((cell_2),), normal=intermediate_part_1.edges[26],
590 point=intermediate_part_1.vertices[18])
591
592 # Weld cell 1
593 cell_3 = ((proj_l_inc)/2, -corr_amp/2, 0.002)
594 weld_cell_1 = intermediate_part_1.PartitionCellByPlanePointNormal(
595 cells=intermediate_part_1.cells.findAt((cell_3),), normal=intermediate_part_1.edges[17],
596 point=intermediate_part_1.vertices[15])
597
598 # Weld cell 2
599 cell_4 = (proj_l_inc+l_par/2, -corr_amp, 0.002)
600 weld_cell_2 = intermediate_part_1.PartitionCellByPlanePointNormal(
601 cells=intermediate_part_1.cells.findAt((cell_4),), normal=intermediate_part_1.edges[21],
602 point=intermediate_part_1.vertices[14])
603
604 # Web cell 1
605 cell_5 = ((proj_l_inc)/2, -corr_amp/2, web_height/8)
606 web_cell_1 = intermediate_part_1.PartitionCellByPlanePointNormal(
607 cells=intermediate_part_1.cells.findAt((cell_5),), normal=intermediate_part_1.edges[37],
608 point=intermediate_part_1.vertices[22])
609
610 # Web cell 2
611 cell_6 = (proj_l_inc+l_par/2, -corr_amp, web_height/8)
612 web_cell_2 = intermediate_part_1.PartitionCellByPlanePointNormal(
613 cells=intermediate_part_1.cells.findAt((cell_6),), normal=intermediate_part_1.edges[5],
614 point=intermediate_part_1.vertices[4])
615
616 ## Create remaining quarter wavelengths
617
618 # Mirror first quarter to create remaining quarters
619 intermediate_model.Part(compressFeatureList=ON, mirrorPlane=YZPLANE,
620 name='intermediate_part_2', objectToCopy=intermediate_part_1)
621 intermediate_part_2 = intermediate_model.parts['intermediate_part_2']
622
623 intermediate_model.Part(compressFeatureList=ON, mirrorPlane=XZPLANE,
624 name='intermediate_part_3', objectToCopy=intermediate_part_1)
625 intermediate_part_3 = intermediate_model.parts['intermediate_part_3']

```

```

625 intermediate_part_3 = intermediate_model.parts[intermediate_part_3]
626
627 intermediate_model.Part(compressFeatureList=ON, mirrorPlane=XZPLANE,
628     name='intermediate_part_4', objectToCopy=intermediate_part_2)
629 intermediate_part_4 = intermediate_model.parts['intermediate_part_4']
630
631 ## Define material and sections
632
633 # Define material
634 intermediate_model.Material(name='Steel')
635 intermediate_model.materials['Steel'].Elastic(table=((elastic_modulus, poissons_ratio,))
636
637 # Define sections
638 intermediate_model.HomogeneousSolidSection(material='Steel', name='Solid_section', thickness=None)
639
640 # Assign sections
641 section_part1 = intermediate_part_1.SectionAssignment(offset=0.0,
642     offsetField="", offsetType=MIDDLE_SURFACE, region=Region(
643     cells=intermediate_part_1.cells), sectionName='Solid_section',
644     thicknessAssignment=FROM_SECTION)
645
646 section_part2 = intermediate_part_2.SectionAssignment(offset=0.0,
647     offsetField="", offsetType=MIDDLE_SURFACE, region=Region(
648     cells=intermediate_part_1.cells), sectionName='Solid_section',
649     thicknessAssignment=FROM_SECTION)
650
651 section_part3 = intermediate_part_3.SectionAssignment(offset=0.0,
652     offsetField="", offsetType=MIDDLE_SURFACE, region=Region(
653     cells=intermediate_part_1.cells), sectionName='Solid_section',
654     thicknessAssignment=FROM_SECTION)
655
656 section_part4 = intermediate_part_4.SectionAssignment(offset=0.0,
657     offsetField="", offsetType=MIDDLE_SURFACE, region=Region(
658     cells=intermediate_part_1.cells), sectionName='Solid_section',
659     thicknessAssignment=FROM_SECTION)
660
661
662 ## Assembly quarter wavelengths and create full wavelength
663
664 # Create coordinate system for assembly
665 intermediate_model.rootAssembly.DatumCsysByDefault(CARTESIAN)
666
667 # Insert quarters
668 intermediate_model.rootAssembly.Instance(dependent=OFF, name='Part1-1',
669     part=intermediate_part_1)
670 intermediate_model.rootAssembly.Instance(dependent=OFF, name='Part2-1',
671     part=intermediate_part_2)
672 intermediate_model.rootAssembly.Instance(dependent=OFF, name='Part3-1',
673     part=intermediate_part_3)
674 intermediate_model.rootAssembly.Instance(dependent=OFF, name='Part4-1',
675     part=intermediate_part_4)
676
677 # Translate quarters to correct position
678 intermediate_model.rootAssembly.translate(instanceList=('Part2-1', ),
679     vector=(l_wavelength/2, 0.0, 0.0))
680 intermediate_model.rootAssembly.translate(instanceList=('Part3-1', ),
681     vector=(l_wavelength/2, 0.0, 0.0))
682 intermediate_model.rootAssembly.translate(instanceList=('Part4-1', ),
683     vector=(l_wavelength, 0.0, 0.0))
684 intermediate_instances = intermediate_model.rootAssembly.instances
685
686 # Rotate quarters to correct coordinate system
687 intermediate_model.rootAssembly.rotate(angle=-90.0, axisDirection=(1.0, 0.0, 0.0),
688     axisPoint=(0.0, 0.0, 0.0), instanceList=intermediate_instances.keys())
689
690 # Translate quarters so that origo is in the middle of flange, to conform with global model
691 intermediate_model.rootAssembly.translate(instanceList=intermediate_instances.keys(),
692     vector=(0.0, t_f/2, 0.0))
693
694 # Merge quarters to full wavelength
695 intermediate_model.rootAssembly.InstanceFromBooleanMerge(domain=
696     GEOMETRY, instances=intermediate_instances.values(),
697     keepIntersections=ON, name='solid_wavelength', originalInstances=DELETE)
698 intermediate_model_instance = intermediate_model.rootAssembly.instances['solid_wavelength-1']
699 intermediate_model_wavelength = intermediate_model.parts['solid_wavelength']
700
701 ## Create step and boundary conditions
702
703 # Create step

```

```

704 intermediate_model.StaticStep(name='intermediate_step', previous='Initial')
705
706 # Create submodel BC
707 left_flange_p = (0.0, 0.0 , 0.0)
708 left_flange_face = intermediate_model_instance.faces.findAt((left_flange_p,))
709 left_faces = left_flange_face.getFacesByFaceAngle(corr_ang)
710
711 top_face_p = (proj_l_inc+9*l_par/10, t_f/2+web_height/6, corr_amp)
712 top_face = intermediate_model_instance.faces.findAt((top_face_p,))
713 top_faces = top_face.getFacesByFaceAngle(corr_ang)
714
715 right_flange_p = (l_wavelength, 0.0 , 0.0)
716 right_flange_face = intermediate_model_instance.faces.findAt((right_flange_p,))
717 right_faces = right_flange_face.getFacesByFaceAngle(corr_ang)
718
719 all_faces = left_faces+top_faces+right_faces
720
721 if intermediate_model_position == 1:
722     exterior_tolerance = 0.15
723 else:
724     exterior_tolerance = 0.05
725
726 intermediate_model.SubmodelIBC(absoluteExteriorTolerance=None,
727     centerZoneSize=0.1*t_f, createStepName='intermediate_step',
728     exteriorTolerance=exterior_tolerance, globalDrivingRegion="", globalIncrement=0,
729     globalStep='1', name='driven_nodes', region=Region(
730     faces=all_faces), shellThickness=t_f,
731     timeScale=OFF)
732
733 ## Translate wavelength to desired position and create mesh
734
735 # Translate wave length to desired position along girder
736 intermediate_model_position = intermediate_model_position-1
737 intermediate_model.rootAssembly.translate(instanceList=intermediate_instances.keys(),
738     vector=(intermediate_model_position*l_wavelength, 0.0, 0.0))
739
740 # Seed wavelength
741 intermediate_model_wavelength.seedPart(deviationFactor=
742     0.1, minSizeFactor=0.1, size=intermediate_element_size)
743
744 # Set element type
745 if intermediate_element_type == 'free':
746
747     all_cells = intermediate_model_wavelength.cells
748     intermediate_model_wavelength.setMeshControls(regions=all_cells,
749     elemShape=TET, technique=FREE)
750
751 intermediate_model_wavelength.setElementType(elemTypes=(
752     ElemType(elemCode=C3D20R, elemLibrary=STANDARD), ElemType(elemCode=C3D15,
753     elemLibrary=STANDARD), ElemType(elemCode=C3D10, elemLibrary=STANDARD)),
754     regions=(intermediate_model_wavelength.cells,))
755
756 # Generate mesh
757 intermediate_model_wavelength.generateMesh()
758
759 # Create intermediate job
760 intermediate_analysis = mdb.Job(atTime=None, contactPrint=OFF, description="", echoPrint=OFF,
761     explicitPrecision=SINGLE, getMemoryFromAnalysis=True, historyPrint=OFF,
762     memory=90, memoryUnits=PERCENTAGE, model='intermediate_model', modelPrint=OFF,
763     multiprocessingMode=DEFAULT, name='intermediate_analysis', nodalOutputPrecision=
764     SINGLE, numCpus=1, numGPUs=0, queue=None, resultsFormat=ODB, scratch="",
765     type=ANALYSIS, userSubroutine="", waitHours=0, waitMinutes=0)
766
767
768
769 #Submit intermediate job
770 if debug == 0:
771     global_analysis.waitForCompletion()
772     intermediate_analysis.submit(consistencyChecking=OFF)
773
774
775 #-----S - POINT MODEL-----
776
777
778 ## Create S-point model by cutting a part of the intermediate model
779 mdb.Model(name='s_point_model', objectToCopy=intermediate_model)
780 s_point_model = mdb.models['s_point_model']
781 s_point_model.setValues(globalJob='intermediate_analysis', shellToSolid=OFF)

```

```

782
783 # Rename the second quarter from the intermediate model
784 s_point_model.parts.changeKey(fromName='intermediate_part_2', toName='s_point_part')
785 s_point_part = s_point_model.parts['s_point_part']
786
787 # Delete stuff that we don't need
788 del s_point_model.parts['intermediate_part_1']
789 del s_point_model.parts['intermediate_part_3']
790 del s_point_model.parts['intermediate_part_4']
791 del s_point_model.parts['solid_wavelength']
792
793 del s_point_model.rootAssembly.instances['solid_wavelength-1']
794
795 del s_point_model.boundaryConditions['driven_nodes']
796
797 del s_point_model.steps['intermediate_step']
798
799 ## Create S-point part
800
801 # Cut web to make model smaller
802
803 s_point_model.ConstrainedSketch(gridSpacing=0.005, name='web_cut_sketch',
804     sheetSize=0.219, transform=s_point_part.MakeSketchTransform(
805     sketchPlane=s_point_part.faces[14],
806     sketchPlaneSide=SIDE1,
807     sketchUpEdge=s_point_part.edges[42],
808     sketchOrientation=RIGHT, origin=(0.0, b_f/2, 0.0)))
809 web_cut_sketch = s_point_model.sketches['web_cut_sketch']
810 web_cut_sketch.sketchOptions.setValues(decimalPlaces=3)
811 # s_point_part.projectReferencesOntoSketch(filter=COPLANAR_EDGES,
812 web_cut_sketch.rectangle(point1=(-l_wavelength, web_height),
813     point2=(l_wavelength, web_height_s_point))
814 s_point_part.CutExtrude(flipExtrudeDirection=OFF, sketch=web_cut_sketch,
815     sketchOrientation=RIGHT, sketchPlane=s_point_part.faces[14],
816     sketchPlaneSide=SIDE1, sketchUpEdge=s_point_part.edges[42])
817
818 del s_point_model.sketches['web_cut_sketch']
819
820 # Cut corrugation quarter into S-point
821 vertices = s_point_part.vertices
822
823 if (vertices.pointsOn[19][0][0])+math.cos((pi/2)-corr_ang)*2*t_f < 0:
824     x_coord_right = (vertices.pointsOn[19][0][0])+math.cos((pi/2)-corr_ang)*2*t_f
825 else:
826     x_coord_right = -0.001
827 if (vertices.pointsOn[20][0][0])-t_f > -l_wavelength/4:
828     x_coord_left = (vertices.pointsOn[20][0][0])-t_f
829 else:
830     x_coord_left = (-l_wavelength/4)+0.001
831
832 y_coord_top = vertices.pointsOn[17][0][1]
833
834 if (vertices.pointsOn[19][0][1])-math.sin((pi/2)-corr_ang)*2*t_f > -b_f/2:
835     y_coord_bot = (vertices.pointsOn[19][0][1])-math.sin((pi/2)-corr_ang)*2*t_f
836 else:
837     y_coord_bot = (-b_f/2)+0.001
838
839 s_point_model.ConstrainedSketch(gridSpacing=0.007, name='vertical_boundaries',
840     sheetSize=0.316, transform=s_point_part.MakeSketchTransform(
841     sketchPlane=s_point_part.faces[0],
842     sketchPlaneSide=SIDE1,
843     sketchUpEdge=s_point_part.edges[41],
844     sketchOrientation=BOTTOM, origin=(0.0, 0.0, web_height_s_point)))
845 vertical_boundaries = s_point_model.sketches['vertical_boundaries']
846 vertical_boundaries.sketchOptions.setValues(decimalPlaces=3)
847 # s_point_part.projectReferencesOntoSketch(filter=COPLANAR_EDGES,
848 vertical_boundaries.rectangle(point1=(x_coord_right, b_f),
849     point2=(0.01, -b_f))
850 vertical_boundaries.rectangle(point1=(x_coord_left, b_f),
851     point2=(-l_wavelength/3, -b_f))
852 bagg=2
853 s_point_part.CutExtrude(flipExtrudeDirection=OFF, sketch=vertical_boundaries,
854     sketchOrientation=BOTTOM, sketchPlane=s_point_part.faces[0],
855     sketchPlaneSide=SIDE1, sketchUpEdge=s_point_part.edges[41])
856
857 del s_point_model.sketches['vertical_boundaries']
858
859 s_point_model.ConstrainedSketch(gridSpacing=0.007, name='horizontal_boundaries',
860

```

```

861 sheetSize=0.316, transform=s_point_part.MakeSketchTransform(
862 sketchPlane=s_point_part.faces[10],
863 sketchPlaneSide=SIDE1,
864 sketchUpEdge=s_point_part.edges[21],
865 sketchOrientation=BOTTOM, origin=(0.0, 0.0, web_height_s_point))
866 horizontal_boundaries = s_point_model.sketches['horizontal_boundaries']
867 horizontal_boundaries.sketchOptions.setValues(decimalPlaces=3)
868 # s_point_part.projectReferencesOntoSketch(filter=COPLANAR_EDGES,
869 horizontal_boundaries.rectangle(point1=(0.01, vertices.pointsOn[17][0][1]),
point2=(-l_wavelength/3, +b_f))
870 horizontal_boundaries.rectangle(point1=(0.01, y_coord_bot),
871 point2=(-l_wavelength/3, -b_f))
872 bagg=2
873 s_point_part.CutExtrude(flipExtrudeDirection=OFF, sketch=horizontal_boundaries,
874 sketchOrientation=BOTTOM, sketchPlane=s_point_part.faces[10],
875 sketchPlaneSide=SIDE1, sketchUpEdge=s_point_part.edges[21])
876
877 del s_point_model.sketches['horizontal_boundaries']
878
879 # Partition S-point part
880 edges = s_point_part.edges
881 vertices = s_point_part.vertices
882
883 cell_p = (-proj_l_inc, -corr_amp, 0.0)
884 cell_1 = s_point_part.cells.findAt((cell_p),)
885 picked_edges_1 = (edges[9], edges[10], edges[11])
886 s_point_part.PartitionCellByExtrudeEdge(line=edges[14], cells=cell_1, edges=picked_edges_1,
887 sense=FORWARD)
888
889 cell_p1 = (x_coord_left, -corr_amp, 0.0)
890 cell_2 = s_point_part.cells.findAt((cell_p1),)
891 picked_edges_2 = (edges[39], edges[40], edges[41])
892 s_point_part.PartitionCellByExtrudeEdge(line=edges[31], cells=cell_2, edges=picked_edges_2,
893 sense=REVERSE)
894
895 cell_p2 = (x_coord_left, -corr_amp, 0.0)
896 cell_3 = s_point_part.cells.findAt((cell_p2),)
897 s_point_part.PartitionCellByPlanePointNormal(point=vertices[10], normal=edges[13], cells=cell_3)
898
899 cell_p3 = (x_coord_left, -corr_amp, 0.0)
900 cell_4 = s_point_part.cells.findAt((cell_p3),)
901 s_point_part.PartitionCellByPlanePointNormal(point=vertices[0], normal=edges[7], cells=cell_4)
902 bagg=2
903 cell_p4 = (x_coord_left, -corr_amp, web_height_s_point/2)
904 cell_5 = s_point_part.cells.findAt((cell_p4),)
905 s_point_part.PartitionCellByPlanePointNormal(point=vertices[1], normal=edges[8], cells=cell_5)
906
907 cell_p5 = (x_coord_right, math.tan(corr_ang)*x_coord_right, 0.0)
908 cell_6 = s_point_part.cells.findAt((cell_p5),)
909 s_point_part.PartitionCellByPlanePointNormal(point=vertices[16], normal=edges[21], cells=cell_6)
910 bagg=2
911 cell_p6 = (x_coord_right, math.tan(corr_ang)*x_coord_right, web_height_s_point/2)
912 cell_7 = s_point_part.cells.findAt((cell_p6),)
913 s_point_part.PartitionCellByPlanePointNormal(point=vertices[5], normal=edges[28], cells=cell_7)
914
915 cell_p7 = (x_coord_right, y_coord_bot, -t_f/2)
916 cell_8 = s_point_part.cells.findAt((cell_p7),)
917 s_point_part.PartitionCellByPlanePointNormal(point=vertices[6], normal=edges[53], cells=cell_8)
918 bagg=2
919
920 ## Assemble parts
921
922 # Create coordinate system for assembly
923 s_point_model.rootAssembly.DatumCsysByDefault(CARTESIAN)
924
925 # Insert s_point part
926 s_point_model.rootAssembly.Instance(dependent=ON, name='s_point_part-1', part=s_point_part)
927 s_point_instance = s_point_model.rootAssembly.instances['s_point_part-1']
928
929 # Rotate S_point to correct position
930 s_point_model.rootAssembly.rotate(angle=-90.0, axisDirection=(1.0, 0.0, 0.0),
931 axisPoint=(0.0, 0.0, 0.0), instanceList=s_point_model.rootAssembly.instances.keys())
932
933 # Translate S-point so that origo is in the middle of flange
934 s_point_model.rootAssembly.translate(instanceList=s_point_model.rootAssembly.instances.keys(),
935 vector=(0.0, t_f/2, 0.0))
936 bagg=2
937
938 # Create step and boundary conditions

```

```

939 # Create S-point step
940 s_point_model.StaticStep(name='s_point_step', previous='Initial')
941
942 # Create submodel BC
943 left_flange_p = (x_coord_left, 0.0, corr_amp)
944 left_flange_face = s_point_instance.faces.findAt((left_flange_p,))
945 left_faces = left_flange_face.getFacesByFaceAngle(corr_ang)
946
947 top_face_p = (x_coord_right, t_f/2+web_height_s_point, -math.tan(corr_ang)*x_coord_right)
948 top_face = s_point_instance.faces.findAt((top_face_p,))
949 top_faces = top_face.getFacesByFaceAngle(corr_ang)
950
951 right_flange_p = (x_coord_right, 0.0, -math.tan(corr_ang)*x_coord_right)
952 right_flange_face = s_point_instance.faces.findAt((right_flange_p,))
953 right_faces = right_flange_face.getFacesByFaceAngle(corr_ang)
954
955 inner_flange_face = s_point_instance.faces[28]
956 inner_flange_faces = inner_flange_face.getFacesByFaceAngle(corr_ang)
957
958 outer_flange_p = (x_coord_left/2, 0.0, -y_coord_bot)
959 outer_flange_face = s_point_instance.faces.findAt((outer_flange_p,))
960 outer_flange_faces = outer_flange_face.getFacesByFaceAngle(corr_ang)
961
962 all_faces = left_faces+top_faces+right_faces+outer_flange_faces+inner_flange_faces
963
964 s_point_model.SubmodelBC(name='driven_nodes', createStepName='s_point_step',
965     region=Region(faces=all_faces), globalStep='1', globalIncrement=0, timeScale=OFF, dof=(1, 2,
966     3, 4, 5, 6), globalDrivingRegion="", absoluteExteriorTolerance=0.0, exteriorTolerance=0.05)
967
968 ## Translate S-point to correct location on intermediate model and create mesh
969 bagg=2
970 # Translate S-point to correct location on intermediate model
971 s_point_model.rootAssembly.translate(instanceList=s_point_model.rootAssembly.instances.keys(),
972     vector=(s_point_model_position*I_wavelength, 0.0, 0.0))
973
974 # Regenerate assembly
975 s_point_model.rootAssembly.regenerate()
976 bagg=2
977 # Seed S-point part
978 s_point_part.seedPart(deviationFactor=0.1, minSizeFactor=0.1, size=s_point_element_size)
979
980 # Reassign seed for horizontal flange edges
981 edges = s_point_part.edges
982 vertices = s_point_part.vertices
983
984 top_right_edge_p = (x_coord_right, 9*y_coord_bot/10, 0.0)
985 top_right_edge = edges.findAt((top_right_edge_p,))
986 top_right_edges = top_right_edge.getEdgesByEdgeAngle(corr_ang)
987
988 top_left_edge_1_p = (x_coord_left, 9*y_coord_bot/10, 0.0)
989 top_left_edge_1 = edges.findAt((top_left_edge_1_p,))
990 top_left_edges_1 = top_left_edge_1.getEdgesByEdgeAngle(corr_ang)
991
992 top_left_edge_2_p = (x_coord_left, 11*(vertices.pointsOn[29][0][1])/10, 0.0)
993 top_left_edge_2 = edges.findAt((top_left_edge_2_p,))
994 top_left_edges_2 = top_left_edge_2.getEdgesByEdgeAngle(corr_ang)
995
996 top_top_edge_p = (x_coord_left/2, vertices.pointsOn[29][0][1], 0.0)
997 top_top_edge = edges.findAt((top_top_edge_p,))
998 top_top_edges = top_top_edge.getEdgesByEdgeAngle(corr_ang)
999
1000 top_bottom_edge_p = (x_coord_left/2, y_coord_bot, 0.0)
1001 top_bottom_edge = edges.findAt((top_bottom_edge_p,))
1002 top_bottom_edges = top_bottom_edge.getEdgesByEdgeAngle(corr_ang)
1003
1004 bottom_right_edge_p = (x_coord_right, 9*y_coord_bot/10, -t_f)
1005 bottom_right_edge = edges.findAt((bottom_right_edge_p,))
1006 bottom_right_edges = bottom_right_edge.getEdgesByEdgeAngle(corr_ang)
1007
1008 bottom_left_edge_p = (x_coord_left, 9*y_coord_bot/10, -t_f)
1009 bottom_left_edge = edges.findAt((bottom_left_edge_p,))
1010 bottom_left_edges = bottom_left_edge.getEdgesByEdgeAngle(corr_ang)
1011
1012 bottom_top_edge_p = (x_coord_left/2, vertices.pointsOn[29][0][1], -t_f)
1013 bottom_top_edge = edges.findAt((bottom_top_edge_p,))
1014 bottom_top_edges = bottom_top_edge.getEdgesByEdgeAngle(corr_ang)
1015
1016 bottom_bottom_edge_p = (x_coord_left/2, y_coord_bot, -t_f)

```

```

1017 bottom_bottom_edge = edges.findAt((bottom_bottom_edge_p,))
1018 bottom_bottom_edges = bottom_bottom_edge.getEdgesByEdgeAngle(corr_ang)
1019
1020 flange_seed_edges = (top_right_edges+top_left_edges_2+top_top_edges+bottom_right_edges+
1021 bottom_top_edges+top_bottom_edges+bottom_bottom_edges+bottom_left_edges+top_left_edges_1)
1022
1023 s_point_part.seedEdgeBySize(edges=flange_seed_edges, size=0.005,
1024 deviationFactor=0.1, minSizeFactor=0.1, constraint=FINER)
1025
1026 # Set flange triangle to sweep mesh
1027 flange_triangle_p = (x_coord_right, y_coord_bot/2, -t_f/2)
1028 flange_triangle = s_point_part.cells.findAt((flange_triangle_p,))
1029 s_point_part.setMeshControls(regions=(flange_triangle, flange_triangle),
1030 technique=SWEEP, algorithm=ADVANCING_FRONT)
1031
1032 # Set element type for S-point model
1033 s_point_part.setElementType(elemTypes=(
1034 ElemType(elemCode=C3D20R, elemLibrary=STANDARD), ElemType(elemCode=C3D15,
1035 elemLibrary=STANDARD), ElemType(elemCode=C3D10, elemLibrary=STANDARD)),
1036 regions=(s_point_part.cells,))
1037
1038 # Generate S-point mesh
1039 cells = s_point_part.cells
1040
1041 structured_cells = (cells[1], cells[2], cells[3], cells[4], cells[5], cells[8])
1042 s_point_part.generateMesh(regions=structured_cells)
1043
1044 sweep_cells = (cells[0], cells[6], cells[7])
1045 s_point_part.generateMesh(regions=sweep_cells)
1046
1047 override_seeds = s_point_part.cells.getSequenceFromMask(mask=('[#1ff ]', ), )
1048 s_point_part.generateMesh(regions=override_seeds, seedConstraintOverride=ON)
1049
1050 # Create S-point job
1051 s_point_analysis = mdb.Job(atTime=None, contactPrint=OFF, description="", echoPrint=OFF,
1052 explicitPrecision=SINGLE, getMemoryFromAnalysis=True, historyPrint=OFF,
1053 memory=90, memoryUnits=PERCENTAGE, model='s_point_model', modelPrint=OFF,
1054 multiprocessingMode=DEFAULT, name='s_point_analysis', nodalOutputPrecision=
1055 SINGLE, numCpus=1, numGPUs=0, queue=None, resultsFormat=ODB, scratch="",
1056 type=ANALYSIS, userSubroutine="", waitHours=0, waitMinutes=0)
1057
1058 # Submit S-point job
1059 if debug == 0:
1060 intermediate_analysis.waitForCompletion()
1061 s_point_analysis.submit(consistencyChecking=OFF)
1062
1063 ## End of file

```